Super-Resolution Imaging via Spectral Separation of Quantum Dots

Kemal Oguz Keseroglu

Submitted in partial fulfilment
of the requirements of the Degree of
Doctor of Philosophy

29 November 2017

School of Physics and Astronomy
Queen Mary, University of London

Queen Mary
University of London

Statement of originality

I, Kemal Oguz Keseroglu, confirm that the research included within this thesis is my own work or that where it has been carried out in collaboration with, or supported by others, that this is duly acknowledged below and my contribution indicated. Previously published material is also acknowledged below.

I attest that I have exercised reasonable care to ensure that the work is original, and does not to the best of my knowledge break any UK law, infringe any third party's copyright or other Intellectual Property Right, or contain any confidential material.

I accept that the College has the right to use plagiarism detection software to check the electronic version of the thesis.

I confirm that this thesis has not been previously submitted for the award of a degree by this or any other university.

The copyright of this thesis rests with the author and no quotation from it or information derived from it may be published without the prior written consent of the author.

.....

Kemal Oguz Keseroglu

29 November 2017

The data presented in section 3.4.5 and in Figure 3.30 were collected by Nikolaos Papaioannou from Queen Mary, University of London.

Abstract

There has been significant progress in the optical resolution of microscopes over the last two decades. However, the majority of currently used methods (e.g. STED, PALM, STORM) have a number of drawbacks, including high intensities of light that result in damage to living specimens in STED, and long data acquisition time leading to limitations on live-cell imaging. Therefore, there is a niche for faster image acquisition at lower intensities while maintaining resolution beyond the diffraction limit.

Here, we have developed a new methodology – Quantum Dot-based Optical Spectral Separation (QDOSS) – which relies on using Quantum Dots (QDs) as fluorophores, and on their separation and localisation based on their spectral signatures. We utilise the key advantages of QDs over the usual organic fluorophores: broad excitation, narrow emission spectra and high resistance to photobleaching. Besides, since QDOSS is based on spectral differences for separation, QDs can be deterministically localised in a relatively short time – milliseconds and, potentially, microseconds. Last but not least, QDOSS is suitable for obtaining super-resolution images using a standard confocal fluorescence microscope equipped with a single laser excitation wavelength and capable of spectral signal separation (e.g. Leica TCS SP series or Zeiss LSM series).

First, we demonstrated resolution down to 60 nm using triangular DNA origami as a reference. Furthermore, we labelled and imaged the alpha-tubulin structure in HEK293T cells. We showed that using a mixture of standard off-the-shelf QDs of different sizes, resolution down to 40 nm could be achieved via spectroscopic separation of QDs. Finally, we demonstrated that QDOSS could also be used for multicolour imaging of synaptic proteins distributed around synapsis in neurons within diffraction limit.

All in all, we believe that these features of QDOSS make it a potential method for long-term live super-resolution imaging, which is going to have a high impact in biological sciences.

Publications

[4] **K. Keseroglu**, D. Huang, M. Palma, A.V. Sapelkin, "Super-Resolution Imaging via Spectral Separation of Quantum Dots", (To be submitted to Small), 2017.

[3] M. Altunbek, M.E. Yalvac, **K. Keseroglu**, A. Palotas, M. Culha, A.A. Rizvanov, "Gold-and Silver-based Nano-Particles Influence Pseudo-Typed Lenti-viral Infection", Current Nanoscience, Vol. 9, No. 6, pp. 693-697, 2013.

[2] A.Y. Sonay, **K. Keseroglu**, M. Culha, "2D Gold Nanoparticle Structures Engineered Through DNA Tiles for Delivery and Therapy", Nano Biomedicine and Engineering, Vol. 4, No. 1, pp. 17-22, 2012.

[1] **K. Keseroglu**, M. Culha, "Assembly of nanoparticles at the contact line of a drying droplet under the influence of a dipped tip", Journal of Colloid and Interface Science, Vol. 360, No. 1, pp. 8-14, 2011.

Conferences

[4] **K. Keseroglu**, D. Huang, J. Heller, M. Palma, D.A. Rusakov and A.V. Sapelkin, "Co-localisation imaging of scaffolding proteins located around the synaptic cleft below the diffraction limit", Quantitative BioImaging (QBI) Conference, College Station, Texas, USA, 5-7 January, 2017 (poster).

[3] **K. Keseroglu** and A.V. Sapelkin, "Super-resolution imaging of biological samples via spectral separation of quantum dots", London Super-Resolution Society Meeting, London, UK, 26 February, 2016 (oral).

[2] **K. Keseroglu** and A.V. Sapelkin, "Super-resolution imaging via spectral separation of quantum dots", Super-Resolution Microscopy in Infection and Immunity Symposium, Oeiras, Portugal, 21-22 October, 2015 (poster).

[1] **K. Keseroglu**, M.Song and A.V. Sapelkin, "Super-resolution imaging via spectral separation of quantum dots", Faraday Discussion: Single-Molecule Microscopy and Spectroscopy, Royal Society of Chemistry, London, UK, 14-16 September, 2015 (poster).

Dedicated to the peace in the world.

Acknowledgements

I sincerely acknowledge Queen Mary University of London (QMUL) in the UK for the financial support during my study and providing crucial facility for the completion of my thesis. I am extremely grateful to be a member of Centre for Condensed Matter and Materials Physics in the School of Physics and Astronomy.

I would like to express my gratitude to my PhD supervisor Dr Andrei V. Sapelkin for his constant guidance and encouraging support for the duration of experimental and writing stages of the thesis, which would never have been completed without him. I would like to extend my thanks to Prof Gleb Sukhorukov, my second supervisor, who has provided his laboratory to carry out biological experiments in the School of Engineering and Materials Science. I am also grateful to have met with Dr Dongsheng Wu, whose assistance and knowledge in using the confocal microscope was essential in the data collection.

Besides, I would like to thank my PhD examination committee, Dr Theo Kreouzis and Dr Marc Vendrell, for their encouragement and insightful comments.

In addition, I wish to thank our collaborators, Da Huang and Dr Matteo Palma in the School of Biological and Chemical Sciences for their kind help in providing DNA origami, and Dr Janosch Heller and Prof Dmitri A. Rusakov in the Institute of Neurology at University College London, for providing neurons used in multicolour imaging studies, and my colleagues, Dr Mingying Song and Osman Ersoy, for their help in the thesis.

Finally, a special gratitude also goes to my parents, my sister, my mother-in-law and my sisters-in-law for their continued support during my life, and to my wife, Elif, for always standing beside me since we met.

Contents

List of Figures

List of Tables

Abbreviations

Ab	Antibody
ADUs	Analogue-to-Digital Units
AFM	Atomic force microscopy
AMPARs	alpha-amino-3-hydroxy-5-methylisoxazole-4-propionate receptors
bp	base pair
CB	Conduction band
CCD	Charge-coupled device
CQDs	Carbon quantum dots
DIC	Differential interference contrast
DNA	Deoxyribonucleic acid
e-h pair	electron-hole pair
EM	Electron microscope
FIONA	Fluorescence imaging with one-nanometer accuracy
FPALM	Fluorescence photoactivation localisation microscopy
FWHM	Full width at half maximum
γ-TuRC	gamma-tubulin ring complex
GDP	Guanosine diphosphate
GDSC	Genome Damage and Stability Centre
GFP	Green fluorescent protein
GSD	Ground state depletion
GTP	Guanosine triphosphate
HEK	Human embryonic kidney
LSCM	Laser scanning confocal microscope

MTOC	Microtubule Organising Centres
NA	Numerical aperture
NMDARs	N-methyl-D-aspartate receptors
NSOM	Near Field Scanning Optical Microscopy
PALM	Photoactivation localisation microscopy
PMT	Photomultiplier tube
PSF	Point-spread function
QCE	Quantum confinement effect
QDOSS	Quantum Dot-based Optical Spectral Separation
QDs	Quantum dots
QY	Quantum yields
ROI	Region of interest
SIM	Structured illumination microscopy
SMLM	Single-molecule localisation microscopy
SPDM	Spectral precision distance microscopy
SR	Super-resolution
ss	single stranded
STED	Stimulated emission depletion
STORM	Stochastic optical reconstruction microscopy
TIRF	Total internal reflection fluorescence microscope
VB	Valence band

Symbols

η	Density function ($number/cm^2$)
ε	Dielectric constant (F/m)
d	Diffraction limit (nm)
D	Dimension
e	Electron charge (C)
$\Delta\ E$	Energy gap (eV)
b^2	Expected number of photons per pixel (background noise)
I	Intensity (Wcm^{-2})
σ	Localisation precision (nm)
m	Number of distinctive QDs
k	Number of positions
ν	Photon frequency (s^{-1})
N_p	Photon number
a	Pixel size (nm)
h	Planck's constant ($6.626068 \times 10^{-34} \cdot m^2kg/s$)
P	Probability
r	Radius of the quantum dot (nm)
n	Refractive index
R	Resolution
R_{QD}	Size of QD (nm)
s	Standard deviation (nm)
λ	Wavelength (nm)

Chapter 1

INTRODUCTION

1.1 Thesis content and structure

The aim of this thesis was to develop labelling strategies to test spectroscopic super-resolution imaging of biological samples via "Quantum Dot-based Optical Spectral Separation" (QDOSS) using a standard confocal microscope. The proposed approach allows to shift super-resolution from the temporal to the spectral domain, thus promising in some cases much faster image acquisition than currently possible. The approach is first tested using reference deoxyribonucleic acid (DNA) ruler and DNA origami structures. It was then applied to imaging alpha-tubulin in human embryonic kidney (HEK) 293T cells and to observe synaptic proteins localised around the synaptic cleft in neurons. Finally, we tested our labelling methods using a novel fluorophore system - carbon nanoparticles. We demonstrated that resolution down to at least 40 nm could be achieved at sub-second acquisition time using a mixture of quantum dots with distinct emission wavelength. The proposed method does not require complicated custom instrumentation and can be implemented using any standard confocal microscope capable of spectral signal separation and a single excitation laser wavelength.

1.2 History of microscopy

Human beings have been trying to understand and influence their environment throughout history. The special characteristic of human desire and curiosity has

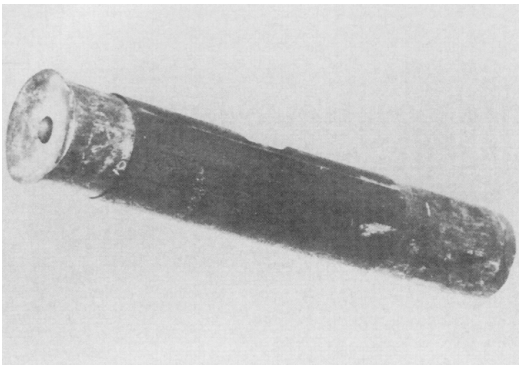

Figure 1.1: The first microscope, designed by Hans and Zacharias Janssen in 1590. Figure sourced from [2].

enabled us to develop science, philosophy, culture, technology and numerous other fields of knowledge. Yet although we could explain macroscopic activities and processes in the world with the naked eye, our understanding of astronomic and microscopic fields came after the invention of artificial lenses, and using them in telescopes and microscopes, which produce magnified visual images of objects that are far away or too small to be seen by the naked eye. From the late 16^{th} century, several microscopic techniques have been developed, and microscopes have played an important role in understanding what is going on in the micro world.

The first compound microscope, which was composed of three sliding tubes measuring 18 inches when fully extended and provided 9 times magnification, was conceived by two Dutch spectacle makers, Hans Jansen and his son Zacharias Jansen, in the 1590s (Figure 1.1) [1, 2]. After the invention of the optical (light) microscope, the first primitive observations of a plant cell was published by the English physicist Robert Hooke, who first defined a "cell" in his book, *Micrographia*, in 1665 (Figure 1.2) [3]. At around the same time, Dutch scientist Anton van Leeuwenhoek developed a microscope that could achieve magnification by a factor of over 270 and used his single lens microscope with its short focal length to achieve a resolution down to micro scale. With this ability, he made an number of biological discoveries. He was the first to see and describe bacteria and yeast plants.

In the subsequent 200 years of work in optical microscopy, there were some slight improvements in microscope technology, such as the manufacturing of improved lenses

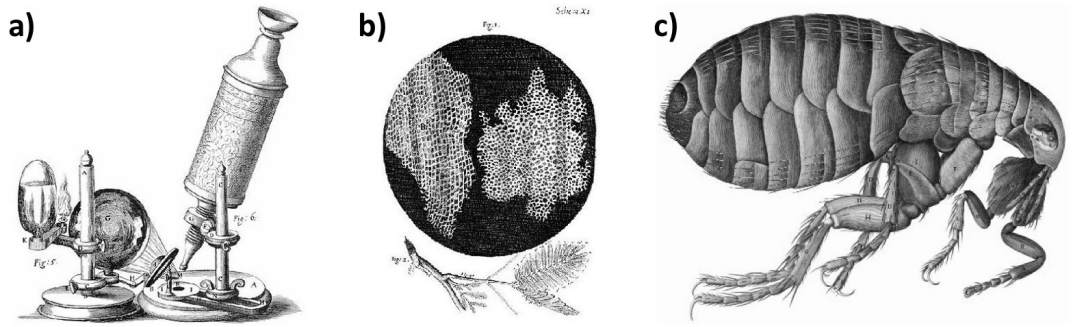

Figure 1.2: (a) The Hooke microscope and (b, c) Hooke's own sketches of his observations: the structures of (b) cork and (c) flea. Figure sourced from *Micrographia*.

in terms of correcting of chromatic[1] and spherical[2] aberrations by Joseph Jackson Lister in the 1830s. Despite these improvements, the microscopic resolution was still about 1 μm at that time. Following the development of homogeneous oil immersion objective, Ernst Abbe and Carl Zeiss produced the world's leading microscopes in the 1880s [4]. In the early 20^{th} century, the Austrian manufacturer Reichert Zetopan introduced Infinity Corrected Optics (Figure 1.3 [5]), which makes it possible to adjust the distance between the objective and relay lenses without affecting the magnification, and to add additional optical elements to the tube, such as filters and mirrors, without distorting the image. This technology is now well developed and commonly used as an industrial standard by the microscope manufacturers, Zeiss and Leica.

Another fundamental development on microscopic imaging was the invention of photodetectors, and so digital image processing. After the discovery of photoelectric effect, which means the emission of electrons from a surface by an incident of light, in 1887 by Heinrich Hertz [6], Albert Einstein drew a model that hypothesises the photoelectric effect stems from the discrete energy packets of light in 1905 [7]. Since then, the principle of the photoelectric effect has started being used in the detectors of microscopes, such as photomultiplier tubes (PMT) and charge-coupled devices (CCD). A typical PMT detector consists of a photocathode, where photons hit and are

[1]Chromatic Aberration: different refraction of light at different wavelengths by a lens.

[2]Spherical Aberration: imperfect refraction of an incident of light between edges and near the axis after passing through a spherical lens.

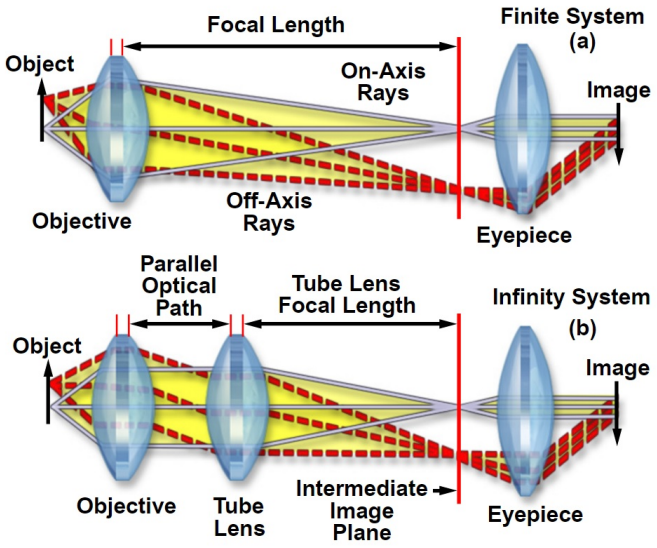

Figure 1.3: The principle diagram of (a) finite-correction optical system and (b) infinity-corrected optical system. Figure sourced from [5].

converted into electrons; a multiplier chain, which is a string of electron enhancers, called dynodes; and an anode, where the amplified electrical signal is collected and measured (Figure 1.4a). PMTs can detect even a single photon of light, and now they are widely used in microscopes. As for the charge-coupled device (CCD), it was first introduced by Willard Boyle and George E. Smith in 1969 [8, 9]. A CCD consists of sensors that convert photons to electrons, and transport the charge across the chip to one corner of the array, where the charge is converted into a voltage by a charge amplifier. So that photons hitting an array of pixels can be read and stored in the memory of a digital device as a binary value (greyscale) related to the amount of charge. The resolution of the digital output image is determined by the number of these pixels per unit area (Figure 1.4b). Today, the physical size of the pixels on a typical CCD camera ranges from 6.45 μm to 24 μm, which provides down to 60 nm per pixel image resolution using a high magnification lens (100X 1.4 NA) [10]. Thanks to the use of digital cameras in imaging, obstacles to the mathematical analysis of the images were removed. While it was limiting to do image analysis via observation with the naked eye or on photographic film, it has become possible to learn more about the image by using PMT and CCD, such as quantification of intensity over a certain parts

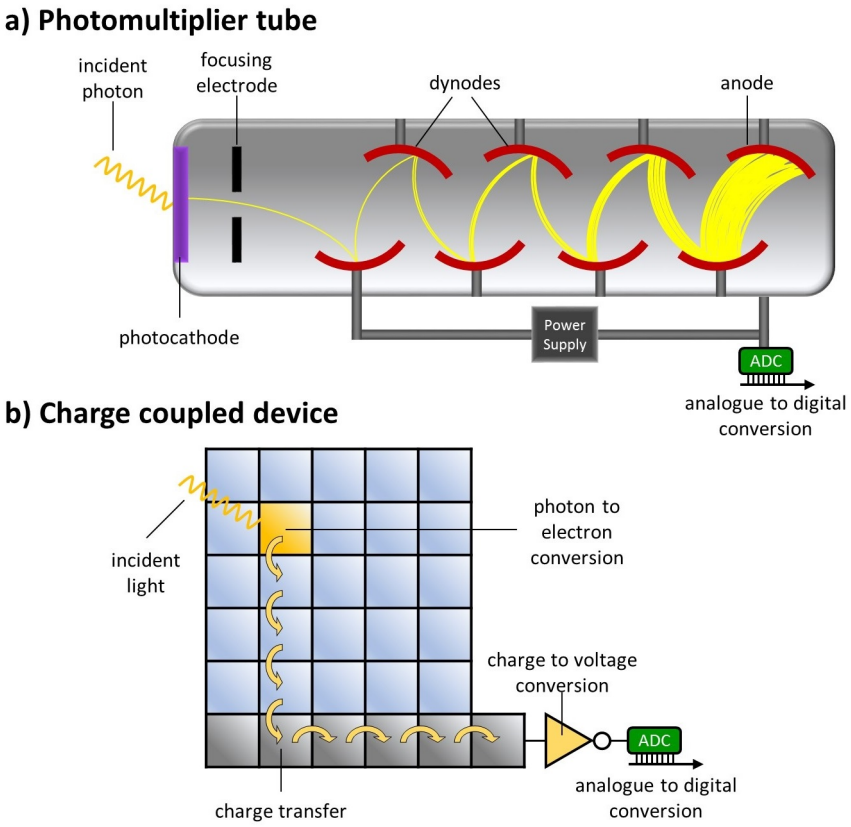

Figure 1.4: Schematic representation of the working principles of (a) photomultiplier tube (PMT) and (b) charge-coupled device (CCD).

of an image [11].

Another fundamental development in microscopic imaging was the invention of "electron microscopy" [12]. Since the optical limit is related to the wavelength of light according to Abbe and Rayleigh (see below), electromagnetic radiation with a shorter wavelength than visible light has been used since the 1930s. As in the optical microscope that has a light source, which allows the sample to be seen, the condenser, which focuses light onto the specimen, and magnifier (lenses), which enables the sample to be seen larger; in an electron microscope (EM), however, the electron beam is used as a source instead of light to generate the image, and a magnetic lens is used as a condenser rather than an optical lens. On the one hand, EM has advantages over the traditional microscope, such as having a higher resolution, large depth of field and capacity for continuously controlling the degree of magnification. On the other

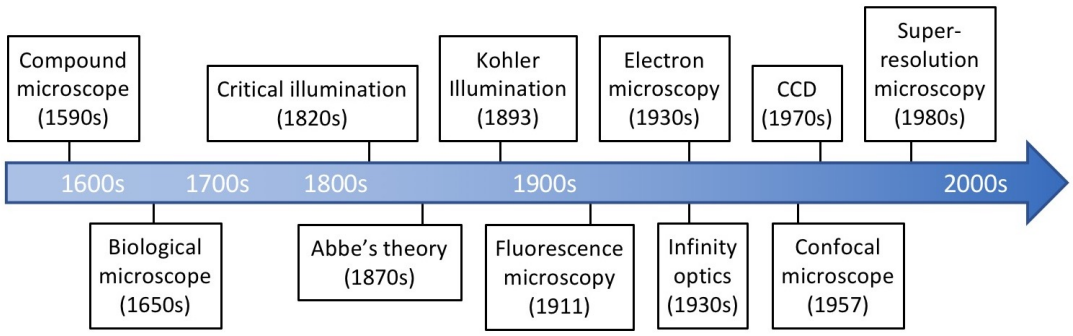

Figure 1.5: A timeline and key developments in the microscope history.

hand, there are also some disadvantages, for instance, biological specimens cannot be viewed *in vivo* due to the fact that high vacuum condition and coating of the dried sample are required. These requirements make it impossible to study live samples in EM [13].

Illumination and contrast play key roles in microscopy. There are several methods of illumination with the most common being bright and dark field microscopy. In bright-field illumination (one of the simplest methods) a sample illuminated by transmitted white light and contrast is achieved by attenuation of the transmitted light according to density variation in the sample. In the late 19^{th} century, Edward Nelson introduced the Critical Illumination technique, where a substage condenser was used for focusing the light of the illumination source on the sample bright illumination [14]. However, it didn't solve the problem of even illumination as the image of the light source was also visible. Later, in 1893, August Köhler designed a new method of illumination, the Köhler Illumination, which produced extremely even illumination of the specimen via placing the image of the filament in the back focal plane of the objective lens, so that the light source is no longer able to be seen by the observer's eye [15] (for a comparison between Critical Illumination and Köhler Illumination, please see Figure 1.6). In the dark-field microscopy the scattered light from the sample is used. A phase ring is placed between the light source and the condenser. It blocks part of the light and allows only an outer ring of illumination, which reaches the objective only when there is a sample on the focus plane, and the light is scattered by the sample. In other methods, such as phase contrast microscopy, which was

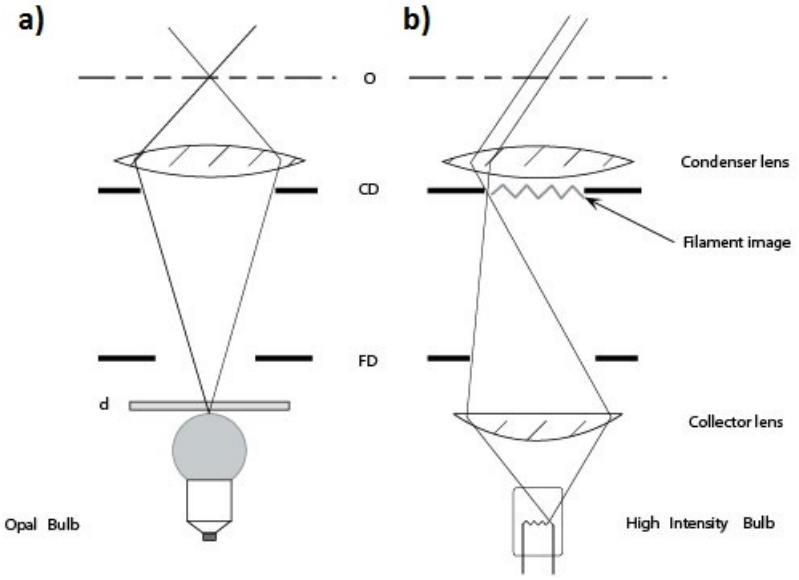

Figure 1.6: A comparison of optical paths for (a) Critical and (b) Köhler Illumination. (FD: Field diaphragm, CD: Condenser diaphragm). Figure sourced from [17].

invented by the Dutch physicist Frits Zernike in 1934, another condenser is used to refocus the annular light to the objective, and a phase plate is inserted to increase the contrast after the light is scattered from the specimen. Thicker part of a sample shifts the phase of the scattered light compared to the direct light. This leads to interference of the scattered light and the direct light so that a phase contrast can be achieved. In cross-polarised illumination, instead of a phase ring and a phase plate, two polarising plates orientated at 90 degrees to the illumination are used. Thus, no light can be detected unless there is a sample. Another polarised light microscope used for the contrast enhancement is differential interference contrast (DIC) microscopy, which was first devised by Polish physicist Georges Nomarski in 1952 [16]. It uses Nomarski-modified Wollaston prism to separate the polarised light into two rays with 90° polarisation before the sample and to recombine them after passing through the sample, which causes optical differentiation that generates the image.

All of these methods have their advantages and disadvantages which become quite significant for cellular work where contrast can be very low (see Figure 1.7a-d). A solution to the problem of contrast was found with the development of fluores-

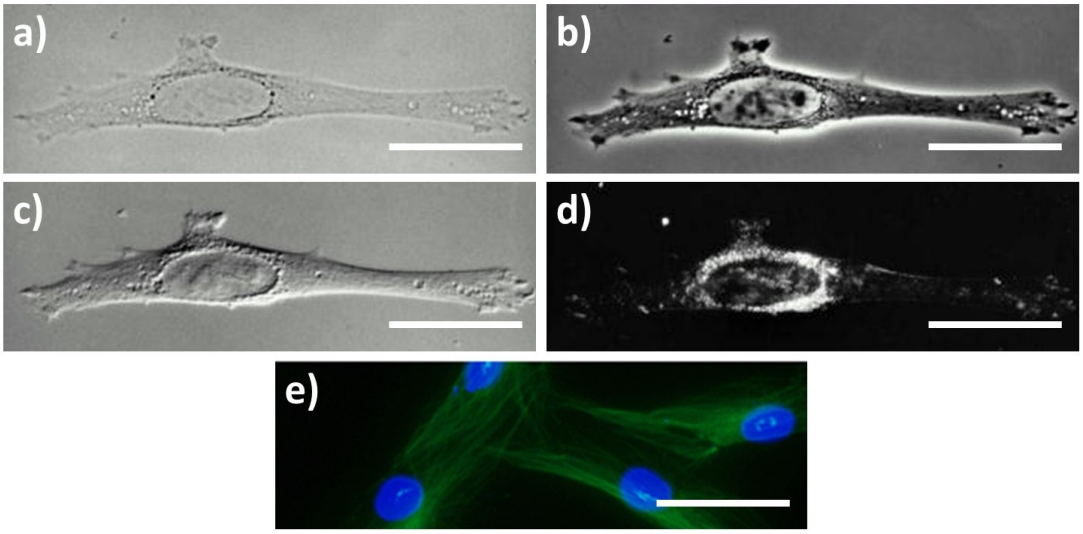

Figure 1.7: Example images of several advanced optical microscopies. A fibroblast cell seen in (a) bright-field microscopy, (b) phase-contrast microscopy, (c) differential interference contrast microscopy, (d) dark field microscopy [18], and (e) multicolour fluorescence microscopy image of fixed fibroblast cells stained with anti-alpha-tubulin antibody (red) and DAPI (blue) [19]. (Scale bar is 50 μm.)

cence microscopy in the second part of 20^{th} century. In fluorescence microscopy in place of absorption or reflection of white light, fluorescence and phosphorescence properties that stem from the interaction of light and probe (i.e. fluorophore) in the sample are used to enhance the contrast. Figure 1.7 shows example images of each optical microscopy [18, 19]. Today, in the field of molecular bioimaging, fluorescent microscopy is the most widely used microscopy technique. Fluorescence microscopes offer contrast enhancement in images because of the self-illumination of the probes against an otherwise dark background. Fluorescent microscopy offers not only the contrast enhancement, but also provides multicolour imaging by using probes with different emission wavelength (Figure 1.7e). Furthermore, fluorescence microscopes offer a highly tuneable emission and illumination spectrum with the help of filters and monochromatic light sources.

In the following section, the mechanism of fluorescence, the properties of fluorescent probes and different fluorescence microscopy techniques will be discussed in details.

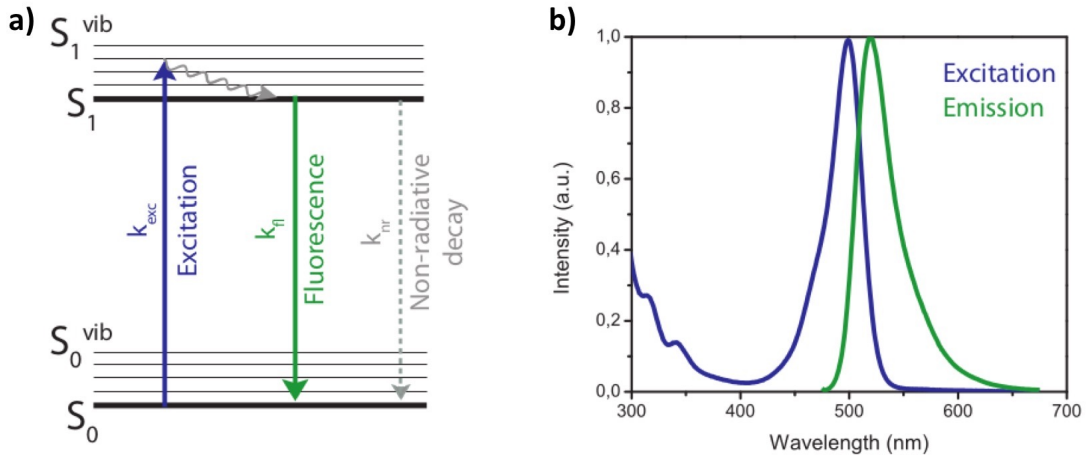

Figure 1.8: (a) The energy state transitions, Jablonski diagram, that lead to fluorescence and non-radiative decay to the ground state. (b) Excitation and emission profile of Alexa Fluor 488. Figure sourced from [20].

1.3 Fluorescence microscopy

In 1852, the Irish physicist George Stokes first described the term 'fluorescence' as a process whereby absorbing the light of a shorter wavelength of certain materials leads to a shifting of emission to a longer wavelength [21]. When an electron is excited by a photon with an equal or greater energy than the energy gap between an excited state (S_1) and ground state (S_0), it transits to the excited state (Figure 1.8a). Then, it quickly relaxes its energy to the lowest sublevel of the excited state through vibration (in a few picoseconds). Here, it can either release the energy via reverting back to the ground state (in the ns range), which is called fluorescence emission, or through intersystem crossing where its excited singlet state passes to an excited triplet state, from where the radiative decay to the ground state is known as phosphorescence ($\sim \mu s$) [22]. In the fluorescence emission, the frequency of the emitted photon is related to the energy difference between the excited state and the ground state:

$$h\nu = \Delta E \tag{1.1}$$

where h is Planck's constant, ν is the frequency of the photon, and ΔE is the energy difference between two states. However, dispersing the energy in vibration results in

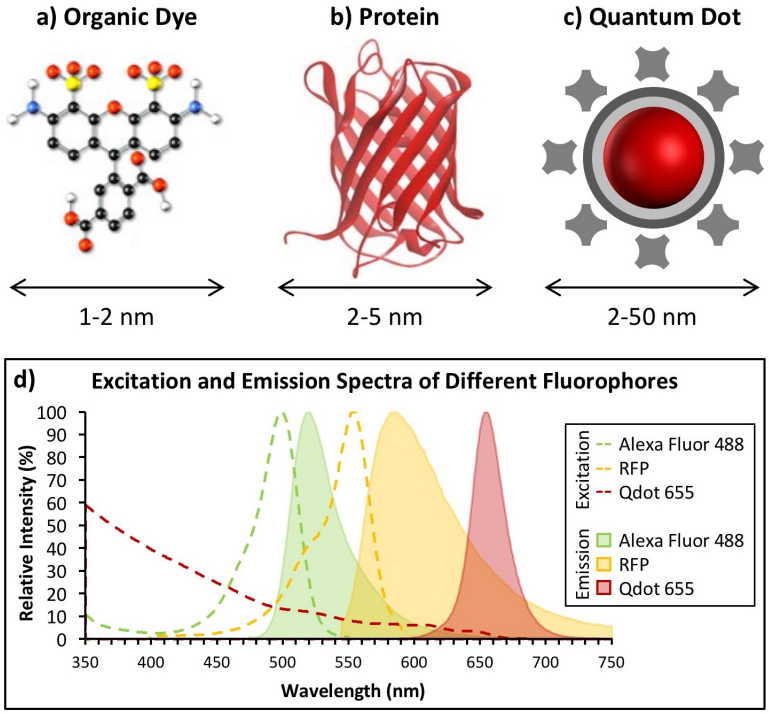

Figure 1.9: Structural and size variances of different fluorescent probes: (a) organic dye (Alexa Fluor 488), (b) protein (red fluorescent protein, RFP) and (c) quantum dot (Qdot-655 streptavidin conjugates), and (d) their excitation (dash lines) and emission (filled area) spectra.

an emission with a lower energy than the excitation, i.e. shifting of wavelength, which is called the Stokes shift (Figure 1.8b).

This is the principle of how fluorescent probes, so-called fluorophores, are involved in fluorescence microscopy. In the following section, different types of fluorophores and their properties will be discussed.

1.3.1 Fluorescent probes

Fluorophores are used to stain a specimen to be observed under a fluorescence microscope. There is a wide range of fluorescent probes in use: organic dyes [23], fluorescent proteins [24] and quantum dots (QDs) [25] (Figure 1.9).

Fluorescent dyes are small organic molecules, usually 1-2 nm in diameter, such as Rhodamine 6G, Cy5 and Alexa Fluor 488 [23, 26]. The fluorescence emission stems from the conformational changes in the structure of organic dyes (Figure 1.10). They

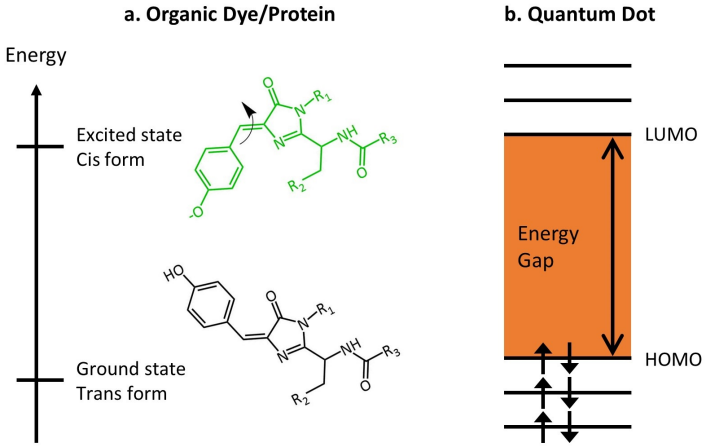

Figure 1.10: Fluorescence mechanism difference between (a) structure changes in dyes/proteins (e.g. Dronpa [23]) and (b) electron transition between energy gap in QDs.

are reported to have excellent quantum yields (QY), which means that the ratio of the number of photons absorbed to emitted ones, approaching 100%. They provide a wide selection of emission colours, for instance, while DAPI gives a blue emission (461 nm), the maximum emissions are green (547 nm) for Rhodamine 6G, red (664 nm) for Cy5, and even near IR (805 nm) for Alexa Fluor 790. Fluorescent dyes are widely used in cellular imaging because of their high QY and developed sophisticated and comprehensive binding protocols suitable for biological samples [27].

Other alternatives to fluorescent dyes are fluorescent proteins. They are large biological macromolecules (normally ∼2-5 nm) that can emit fluorescence. They have become widely used since the discovery of the Green Fluorescent Protein (GFP) in 1962 [28], due to its high stability, decreased toxicity and ability to label the target without the addition of external cofactors [29]. They are genetically fused to the target of interest inside the cell; therefore they are highly stable inside the cell, and are the preferred choice to be used for protein localisation and dynamics in living cells.

Similar to fluorescent dyes, fluorescence emission occurs as a result of structural changes in fluorescent proteins with QYs of 79-85% [30]. However, some fluorescent dyes and proteins are far from able to keep their structure in the long term [26]. During the absorption-emission process, changes in the geometrical shape of the

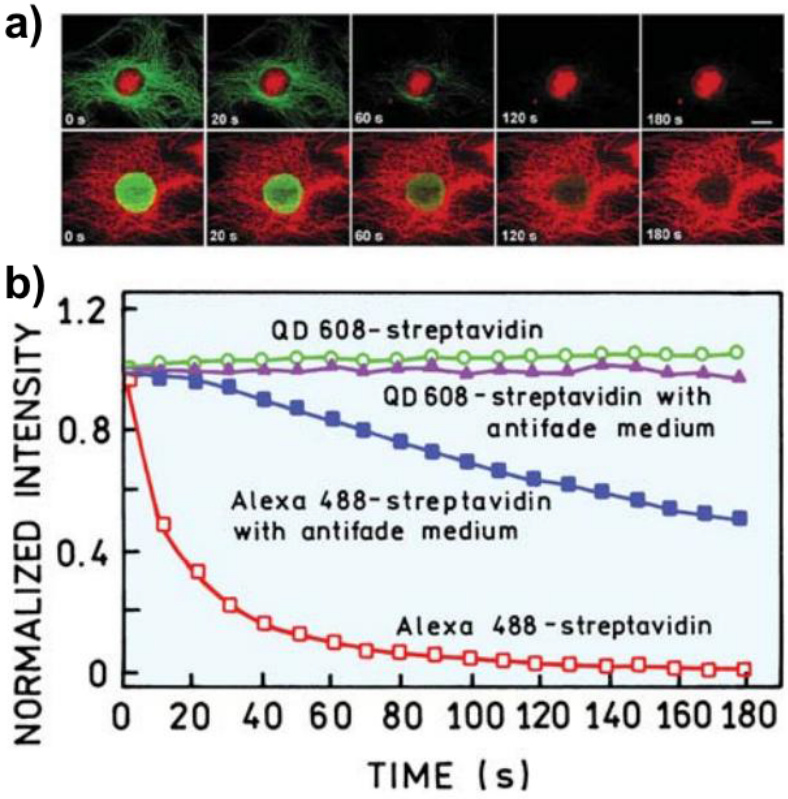

Figure 1.11: Photostability comparison between organic dyes and quantum dots. (a) Change of fluorescence signal in the cells labelled with Alexa Fluor 488 dye (green) and QD 630 (red) under continuous illumination for 3 minutes. (b) Normalised intensities of Alexa 488-streptavidin and QD 608-streptavidin labelled specimens that were mounted with glycerol or antifade mounting medium. Figure sourced from [31].

molecule cause the bond structure to be weakened more quickly, and broken within an average of 1 minute (see Figure 1.11). This irreversible photochemical destruction is called photobleaching and leads to the termination of observation of organic dyes under sufficient light exposure.

One alternative to organic fluorophores that has recently emerged are quantum dots, which will be discussed in detail in the next section.

1.3.2 Quantum Dots

Quantum dots are inorganic nanocrystals that remain more stable under illumination, thus allowing for longer fluorescence observation periods, despite its lower quantum yield (typically below 50-60%). This resistance to bleaching is the major

advantage of QDs over organic dyes, in addition to ease of controlling of its emission wavelength simply by changing particle size. Therefore, QDs occupy an important niche in fluorescence imaging in biolabelling [32, 33]. Additionally, QDs have a broad excitation wavelength range compared to organic dyes (see Figure 1.9d), which allows to efficiently filter out excitation and emission light to avoid their overlap during imaging.

In QDs, contrary to organic dyes, the excitation-relaxation mechanism is purely electronic (i.e. transitions between conduction and valence bands). Therefore, QDs can be observed for long periods of time without any problem of photobleaching, because they do not undergo structural changes. Moreover, the crystal size at nanoscale results in discrete energy levels, and the band gap of the semiconductor increases as the size of the crystal decreases (Figure 1.12). This effect of size is called quantum confinement and is used to control the emission wavelength. For instance, while 4 nm CdSe QDs emit at red wavelengths (maximum 630 nm), 2 nm CdSe QDs emit at green wavelengths (maximum 550 nm) [34]. Unlike dyes, there is no need to use multiple sources for excitation: QDs of all sizes can be excited by the same source.

Furthermore, a single QD has a sharper emission spectrum than the organic dyes because the fluorescence wavelength of a QD depends mostly on the band gap energy, while a number of interband transitions may be allowed in organic dyes. It is shown that ZnS-capped CdSe QDs have much narrower emission spectra compared to an organic molecule (Rhodamine 6G) and the full width at half maximum (FWHM) can be as narrow as 13 nm at room temperature [36]. This allows to fit a larger variety of colours in a single image.

As far as the QY of QDs is concerned, it is much lower than the QYs of the dyes. One of the reasons for low efficiency is surface trapping. However, the longer lifetimes of QDs leads to signal generation over longer periods of time, which partially compensates for the lower QY. Additionally, surface modifications, i.e. encapsulating with a shell material with a higher conduction band, are used to increase the efficiency. This shell material partially prevents the charge from escaping or being trapped at the surface. In addition, it also enables the reduction of cytotoxicity of the core material,

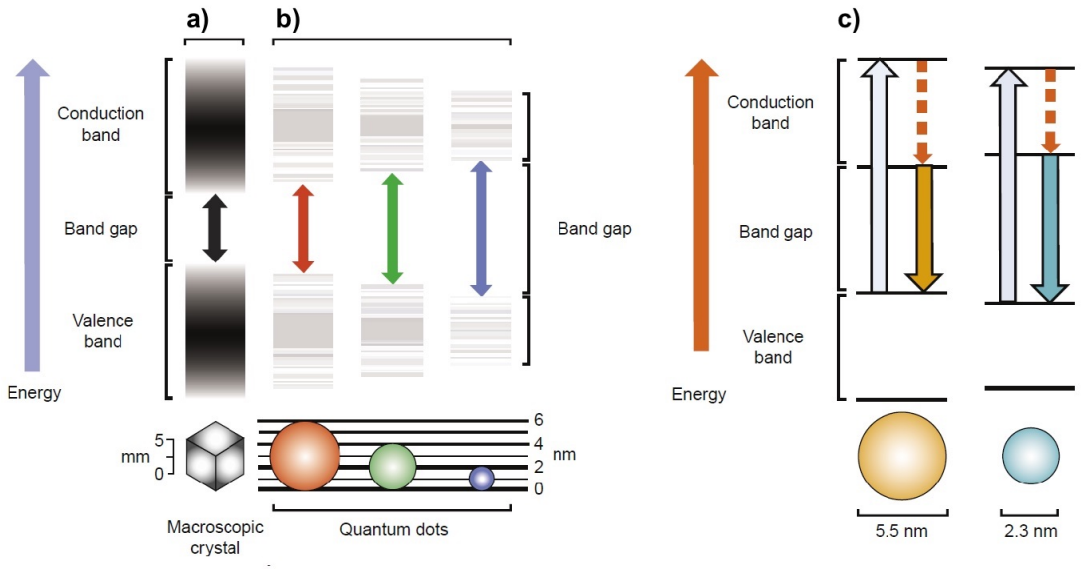

Figure 1.12: Graphical representation of size dependent energy levels and band gaps. (a) Continuous energy spectrum of a bulk semiconductor. (b) Increasing band gaps and discrete energy levels with decreasing sizes of the QDs. Larger QDs have narrow band gaps than small QDs. (c) Comparison of emission wavelengths of different sized QDs (≈590 nm for 5.5 nm and ≈500 nm for 2.3 nm QD) excited at the same wavelength. Figure sourced from [35].

and allows bioconjugation with organic molecules in the cell [37].

1.3.2.1 Light emission in quantum dots

The threshold energy for the absorption spectra is defined by the energy band gap of the semiconductor. When an electron is excited by an energy of photon that is higher than the band gap energy, it jumps from valence to conduction band and leaves a positively charged hole behind. This follows by de-excitation of the electron and recombination of it with the hole at the conduction band via emission of a photon, i.e. fluorescence (Figure 1.13).

The origin of light emission stems from electron-hole recombination. Initially, no electron exists in the conduction band (CB) and no hole can be present in the valence band (VB). After excitation of an electron by a photon to the first excited state of the crystal, an electron-hole pair (e-h pair), called exciton, is created. This corresponds to the hydrogen-like bound state and can be described by the Bohr hydrogen model [38]. In 1913, Niels Bohr developed the model, which is based on the quantisation of

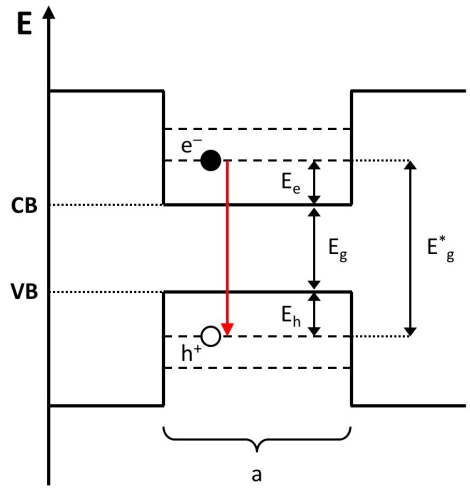

Figure 1.13: Schematic representation of an energy level diagram that shows an increase of the effective band gap because of the confinement of an electron and a hole in a potential well with a size of "a".

energy of an orbiting electron, to explain the hydrogen atom spectrum:

$$\mathrm{R_n} = n a_B, \quad a_B = \frac{4\pi\varepsilon_0\hbar^2}{m_\mathrm{e} e^2} = 0.53\text{Å} \tag{1.2}$$

where a_B is the Bohr radius, which is the orbital radius of the electron at minimum energy state, ε_0 is the the permittivity of vacuum, e is the electron charge, $\hbar$ is the reduced Planck's constant and m_e is the electron rest mass.

The exciton is characterised by the exciton Bohr radius similar to the hydrogen atom, but multiplied by the dielectric constant of the crystal $\varepsilon \neq 1$, and the electron mass is replaced by electron-hole reduced mass μ ($\mu^{-1} = m_e^{*-1} + m_h^{*-1}$, defined by effective masses of electrons and holes in a material):

$$\mathrm{a_B^*} = \frac{\varepsilon\hbar^2}{\mu e^2} = \varepsilon\frac{m_e}{\mu} \times 0.53\text{Å} \tag{1.3}$$

where ε is the dielectric constant of the bulk material, μ is the reduced mass of exciton. The quantum confinement effect (QCE) is expected to be observed when the size of the nanocrystals is comparable to the exciton Bohr radius. Under quantum confinement,

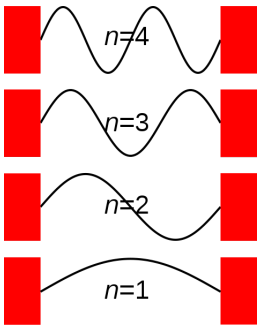

Figure 1.14: 1-D particle in a box model, where the quantum particle is within a potential well with infinite potential at the walls and zero potential within the well.

carriers are trapped within a finite space, which can be approximated as enclosed by infinite potential barriers. This can be illustrated in one dimension as seen in Figure 1.14 by the "particle in a box" model.

The allowed energies for a particle in a box model are discrete. The energy levels are dependent on the effective mass m^*, the size of the confinement space a and the quantum states n, where (n = 1, 2, 3 ...):

$$E_n = \frac{\pi^2 \hbar^2 n^2}{2m^* a^2} \tag{1.4}$$

Brus and Efros used this simple approach to develop a model that could relate the size of the quantum dot to the excited energy states [39]. The quantum dot behaves like the potential well for an exciton in three dimensions:

$$E_g^* = E_g + \frac{\pi^2 \hbar^2}{2\mu r^2} - \frac{1.8e^2}{4\pi\varepsilon} \tag{1.5}$$

where $E_g{}^*$ is the excited energy state, E_g is the bang gap energy of the bulk semiconductor, μ is the reduced mass, r is the radius of the quantum dot, $\hbar$ is the reduced Planck's constant, e is the charge of an electron, ε is the dielectric constant [40]. This shows the dependence of the emission energies on the radius of the quantum dot. Larger QDs would have lower emission energies, and hence larger emission wavelengths.

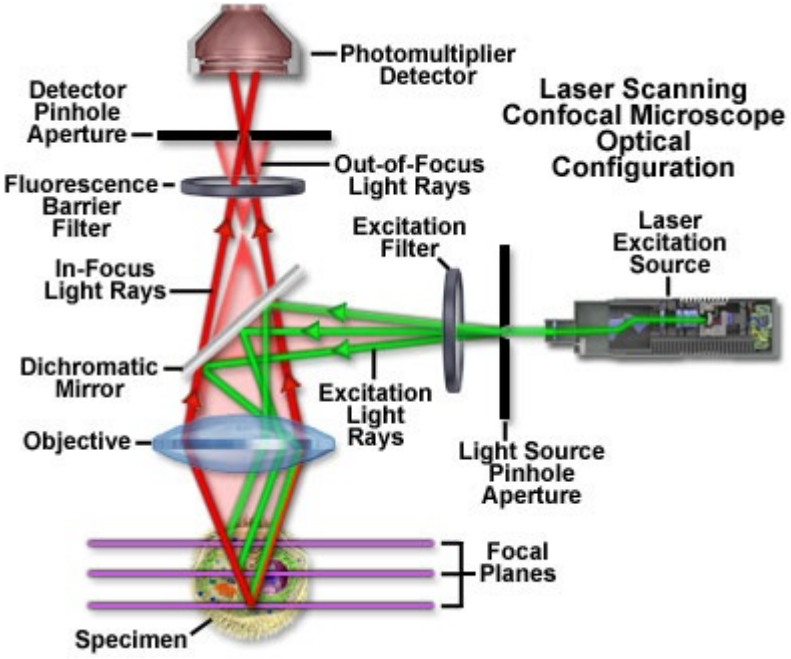

Figure 1.15: Diagram of the confocal principle. Figure sourced from [41].

In the following section, we turn our attention to the practical use of fluorophores in fluorescence microscopy. In particular, a more sophisticated type of fluorescence microscope, confocal microscope will be discussed. Besides the confocal microscope, another type of fluorescence microscope, which is commonly used - "total internal reflection fluorescence microscope" - will also be discussed.

1.3.3 Confocal Microscopy

Confocal Microscopes were first introduced by Marvin Minsky in 1957 [42]. The technique is based on selecting light coming from the focus point, and rejecting light from all other points via putting a pinhole in the back focal plane of the microscope to increase the contrast of the image (Figure 1.15). This approach allows for rejection of out-of-focus background light and thus in further improvement in contrast compared to a regular fluorescence microscope. It is obvious that while eliminating the out-of-focus light, the detector can get fewer photons at any given instant. This leads to the requirement for longer exposure time, in order to collect enough light for a good contrast. Therefore, modern confocal microscopes use high intensity light sources:

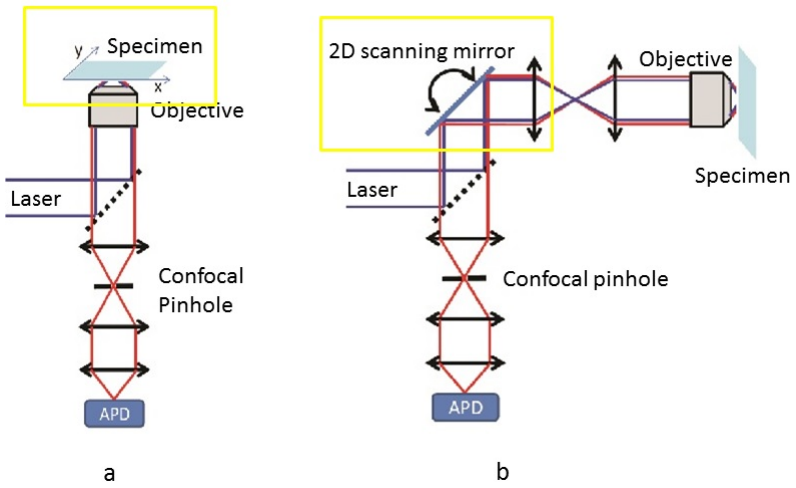

Figure 1.16: Optical path of the light in laser scanning confocal microscopy by either (a) moving of the specimen via stage control, or (b) using 2D scanning mirrors [43]

lasers. Additionally, the size of the pinhole, theoretically, can be reduced to smaller than an Airy disk, but in order to receive enough signals, it is usually adjusted to the same size as an Airy disk. Today, a typical confocal microscope has ∼200 nm lateral and ∼600 nm axial resolution.

In confocal microscopy, since only the light from a focus point is allowed to pass through the pinhole, the image must be built using point-by-point detection. This can be done by means of either scanning the laser methods or using the Nipkow disk system. According to their illumination and detection elements, there are various types of confocal microscopes. For instance, in a laser scanning confocal microscope (LSCM), as its name implies, the sample is scanned and illuminated by one or more very small spots. Either the specimen is moved by a precise stage control, or galvanometer scanners controlled by computers are used to move two internal mirrors for the scanning of lasers (Figure 1.16 [43]). In a typical LSCM, 512x512 pixel images in one dimension take 1.28 seconds at 400 Hz scanning rate. Although this data acquisition time is sufficient for the static systems, it is very slow for dynamic specimens such as blood flow [44].

Another confocal microscopy approach is spinning disk confocal microscopy, which uses a Nipkow disk, which is a spinning disk that has numerous pinholes for allowing

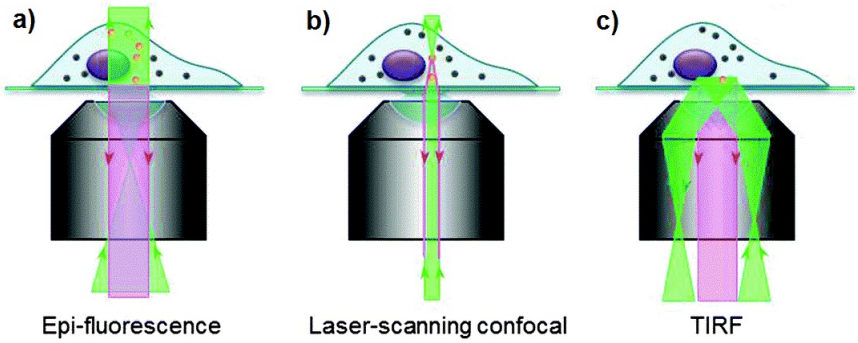

Figure 1.17: Comparison between (a) Epi-fluorescence, (b) Laser Scanning Confocal and (c) TIRF microscopy. Figure sourced from [47].

the laser and light coming from the specimen to pass through [45]. Since the disc has 20,000 pinholes with a diameter of 50 μm and can spin up to 10,000 revolutions per minute, a high-speed measurement of 1 frame/ms can be achieved. Thus, it is possible to observe a cellular process that occurs in milliseconds [46].

Alternative approach to rejecting background fluorescence is the "total internal reflection fluorescence microscope" (TIRF). The idea of TIRF relies on using total internal reflection (Figure 1.17c) to form an evanescent wave, which causes excitation of fluorophores in a very thin optical section (<250 nm) adjacent to the coverslip. Normally, if a light beam comes to a surface with a critical angle, while the majority of the incident light is reflected, a small part of it penetrates through the surface and leads to a thin electromagnetic field, called an evanescent wave, that propagates parallel to the surface in the liquid medium. Therefore, compared to fluorescence and confocal microscopy, only the fluorophores close to the surface are excited and observed in TIRF microscopy with a lack of background noise. Figure 1.17 shows the comparison of the illumination depth between epi-fluorescence microscopy, in which the excitation and the emission light pass through the same light path, LSCM and TIRF microscopy.

Confocal microscopes are now widely used in scientific research and for clinical purposes. Due to its capacity for eliminating out-of-focus light and point-by-point illumination, it provides extremely sensitive biological imaging, 3D and live-cell images. In addition, Leica and Zeiss have commercially utilised spectral separation

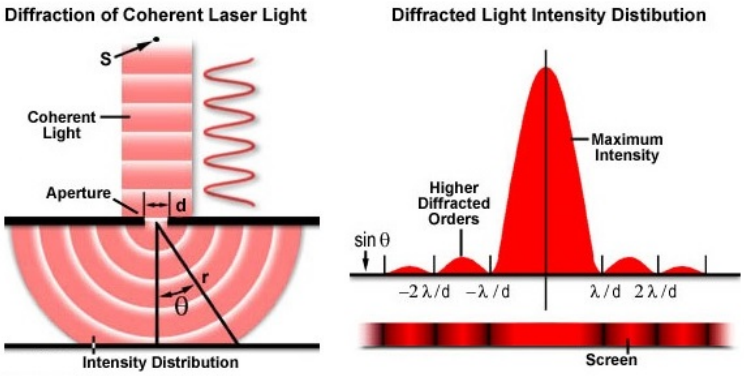

Figure 1.18: Single slit experiment demonstration of diffraction. Spherical waves produce a diffraction pattern. Figure sourced from [48].

capabilities, which allows for multicolour imaging of different biological samples. Despite described advances in techniques and methods, until recently the field of microscopy was significantly held back by the fundamental problem related to the wave nature of light - the diffraction limit. This problem is described in the following section.

1.4 Resolution limit in microscopy

Despite the improvements in optical microscopy, it has spatial and angular limits on resolution. Fundamentally, the resolution limit stems from the wave nature of light, which leads to diffraction pattern when passing through an aperture or an object. According to the principle of the Dutch physicist Christiaan Huygens and the French physicist Augustin-Jean Fresnel, every point on a wave front acts as a secondary spherical wave source, hence interference of spherical waves causes a diffraction pattern centred on a central maximum at the boundary (Figure 1.18). As a result, a point-like light source is seen as a blurred spot, which in optical microscopy is referred to as the point-spread function (PSF).

The resolution limit of an optical microscope was first described and linked to the diffraction on the aperture of an objective by Ernst Abbe in 1873 [49]. Though it is practically possible to magnify the sample more than 1200X, there is an optical limit ($\sim$250 nm) for observing the matter, as expressed in the equation below [49]:

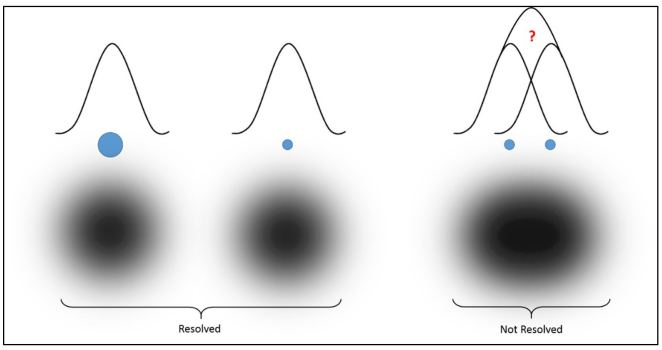

Figure 1.19: Objects that are smaller than the PSF are seen as the same size as the PSF even though they are different in size, and objects that are closer than the FWHM of the PSF cannot be distinguished as separate.

$$d = \frac{\lambda}{2n \sin\theta} \tag{1.6}$$

Where λ is the wavelength of light, n is the refractive index of the medium that light travels in, θ is the angle that light is converging to, and $n \sin\theta$ denominates as numerical aperture (NA). This limit is the minimum size for an object or distance between two objects that can be resolved by a microscope. That is to say, smaller objects than the width of the PSF are observed as the same size as the PSF, even though they are different in size, and two objects that are closer than the FWHM of the PSF cannot be differentiated as separate (Figure 1.19).

Shortly afterwards, in 1879, Lord Rayleigh introduced his famous resolution criterion (Equation 1.7). He linked the optical resolution with the wavelength of light and the numerical aperture of a microscope. The Rayleigh resolution criterion gives the minimum distance between two objects that can be resolved by an optical microscope [50]. The point-spread function can also be measured by the Rayleigh criterion, which is close to Abbe Law [50]:

$$R = \frac{0.61\lambda}{\mathrm{NA}} \approx \frac{\lambda}{2\mathrm{NA}} \tag{1.7}$$

where R is the lateral resolution limit, λ is the wavelength of light, NA is the numerical aperture of the objective. As far as NA and λ are considered as 0.95 in the air and 400 nm for the shortest wavelength of visible light, violet, respectively, the resolution limit can be found $\sim$250 nm. Compared to air (NA= 1), using oil (NA= 1.45) as an immersion medium, the limit can be calculated down to $\sim$200 nm.

This resolution limit has been a significant challenge until recently, which is why super-resolution (SR) microscopy has emerged to overcome the limit and yield higher resolution images, i.e. down to several nm. In the following section, the historical developments in SR imaging and several SR techniques that are commonly used will be described in detail.

1.5 Super-Resolution Microscopy

Most of the SR microscopy techniques were started on the basis of imaging of single particles. Historically, after Ernst Abbe first made a correlation between image resolution of a microscope, the numerical aperture of objective and wavelength of light in 1873, the imaging of single particles below the diffraction limit started in the late 20^{th} century. In 1986, Ashkin et al. invented optical tweezers to characterise biomolecules at a single-molecule level; and Moerner and Kador first observed the optical absorption spectrum of a single molecule at cryo-temperatures in 1989 [51, 52]. In the meantime, single-molecule detection techniques were improving, and Betzig and Lewis et al. published a paper about Near Field Scanning Optical Microscopy (NSOM) for high resolution imaging in 1986 [53]. Just a few years later, a theoretical paper about how to surmount the diffraction limit was published in 1994 by Hell and Wichmann [54]. They described a method based on the transition of fluorescent molecules from “on” to “off” state, which gives rise to obtaining a smaller PSF than that of the conventional one. This concept was first experimentally demonstrated by Klar and Hell in 1999, and followed by an explosive development in the field of super-resolution optical imaging [55, 56]. In 2003, Yildiz and his colleagues published a wonderful paper showing that Myosin V, a dimeric molecular motor, has a hand-

over-hand model of motility by tracking and localising a single fluorophore with one nanometer accuracy in 1-500 milliseconds. They called their method "fluorescence imaging with one-nanometer accuracy" (FIONA) [57].

There have been many techniques developed and commercially used in super-resolution optical imaging up to now. Basically, they can be assembled into three groups: (i) structured illumination techniques, (ii) deterministic-based ensemble techniques and (iii) stochastic-based single-molecule localisation techniques. Whereas the diffraction limit is broken via using a striped pattern of light in the structured illumination microscopy [58], in ensemble-based ones, the aim is to carve out the diameter of PSF using a high intensity of light that suppresses emissions of a large number of photons' fluorescence to the ground state (stimulated emission depletion, STED) [55] or the metastable dark state (ground state depletion, GSD) [59]. On the other hand, single-molecule localisation techniques, e.g. photoactivation localisation microscopy (PALM) [60], fluorescence photoactivation localisation microscopy (FPALM) [61] and stochastic optical reconstruction microscopy (STORM) [62], are based on the localisation of centroids of a single molecule with nanometer level localisation precision (i.e. uncertainty of the position estimation) by turning "on" a small sub-group of fluorescent probes. These methods typically use temporal separation of fluorophores and visualise the structure by localising the centres of the probes' PSF after more than 1000 repeated measurements on a single area of interest. According to all tremendous discoveries in single-molecule and sub-diffraction optical imaging, as mentioned above, William Moerner, Eric Betzig and Stefan Hell were deemed to deserve the Nobel Prize in Chemistry in 2014.

Some of the widely used super-resolution techniques will be considered in detail in the following sections.

1.5.1 Structured Illumination Microscopy

The structured illumination microscopy (SIM) uses a known spatially structured illumination light with a movable diffraction grating. After the excitation light is split into two beams following the diffraction grating, they emerge when they reach the

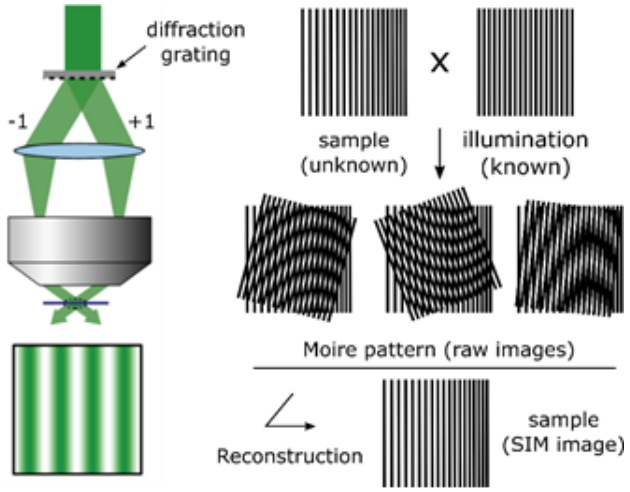

Figure 1.20: Diagram explaining the Moiré effect and the principle of structured illumination microscopy (SIM) [66].

sample and form a sinusoidal illumination pattern. This is called the Moiré effect, which produces a low spatial frequency when two structures of high spatial frequency overlap. After acquiring multiple images that were illuminated by these different patterns, a high-resolution image can be reconstructed (Figure 1.20). It has been reported that SIM has a good capability for 3D imaging and multicolour imaging [63, 64]. The lateral resolution of SIM has been improved down to 50 nm [65].

1.5.2 Deterministic-based super-resolution microscopy

Similar to structured illumination microscopy, modified illumination patterns are used in the deterministic-based ensemble techniques. One of the most known deterministic-based super-resolution microscopy techniques is stimulated emission depletion (STED) microscopy. The idea of "stimulated emission" was first theoretically described by Albert Einstein in 1916 [67]. When a fluorophore at ground state (S_0) absorbs a photon, it jumps to the excited state (S_1), where it vibrationally proceeds to the lowest electronically excited state within a few picoseconds. Here, it can either spontaneously jump down to the ground state with a fluorescence emission, or if it is hit by another photon with a wavelength, which has an energy that fits the energy gap between the ground state and the excited state, stimulation emission happens where the fluorophore goes back to the ground state without fluorescence emission (Figure

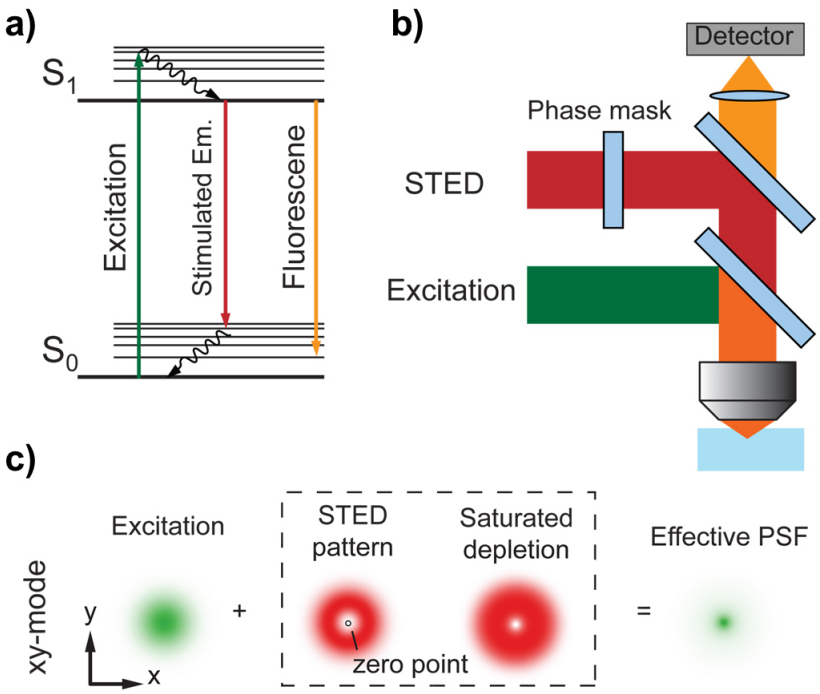

Figure 1.21: The principle of STED microscopy. (a) The stimulated emission process. (b) Schematic representation of a STED microscope. (c) Formation of effective PSF from combination of excitation laser and doughnut-shaped STED laser in the xy mode [68]

1.21a) [68]. Stefan W. Hell and Jan Wichmann were the first to use this property in super-resolution imaging in their theoretical paper in 1994 [54]. They applied a second laser (depletion laser), which was designed as a doughnut shape, to make the fluorophores revert back to the ground state without emitting photons except at the centre of the illumination area at the focal spot (Figure 1.21b,c). Thus, only the tiny centre of the luminous area is left, which makes it possible to decrease the size of the PSF and to achieve lateral resolution down to 35 nm [54]. This new resolution limit in STED is described in the following equation, Eq. 1.8,

$$\mathrm{D} = \frac{\lambda}{2n \sin\theta \sqrt{1 + \frac{I}{I_{\mathrm{sat}}}}} \tag{1.8}$$

where I is the peak intensity of the depletion laser and I_S is the saturation intensity for the fluorophore.

STED microscopy is performed using a combination of pulsed excitation and

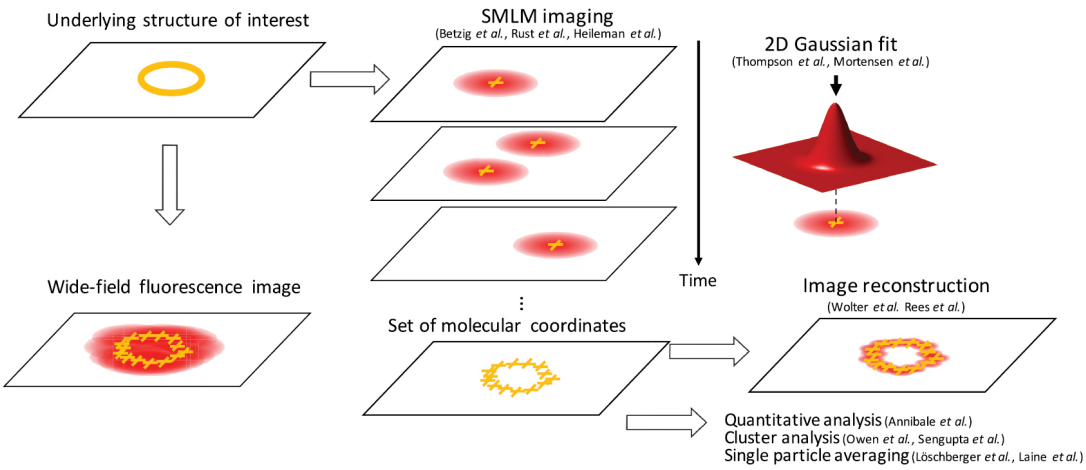

Figure 1.22: The principle of single-molecule localisation microscopy [74].

depletion lasers, which interact with the fluorophores sequentially and emissions are collected in order. Therefore, STED microscopes can be easily derived from laser scanning confocal microscopes. Although there have been several papers published to show that STED microscopy can deliver resolution down to few nm, with image recording times ranging from a few milliseconds to a few seconds [69, 70], it has numerous drawbacks. A high intensity of the laser power that varies between 600 Wcm^{-2} to 10 $MWcm^{-2}$ on the sample is required in order to achieve sufficient stimulated emission [68, 71, 72]. This high level of light intensity leads to damage of living specimens, photobleaching of fluorophores and a build-up of toxic products in the cells [73]. Thus, requiring the use of high intensity of laser power, which significantly affects cell functionality and eventually results in cell death, is still criticised in STED microscopy for live-cell super-resolution imaging.

1.5.3 Stochastic-based super-resolution microscopy

Stochastic-based super-resolution microscopy relies on the detection of single fluorescent probes signals and their precise localisations with subsequent image reconstruction to achieve a super-resolution image. It can be either temporal or spectral basis. In 2006, three different laboratories independently published a new concept for super-resolution based on single-molecule localisation microscopy (SMLM): photoacti-

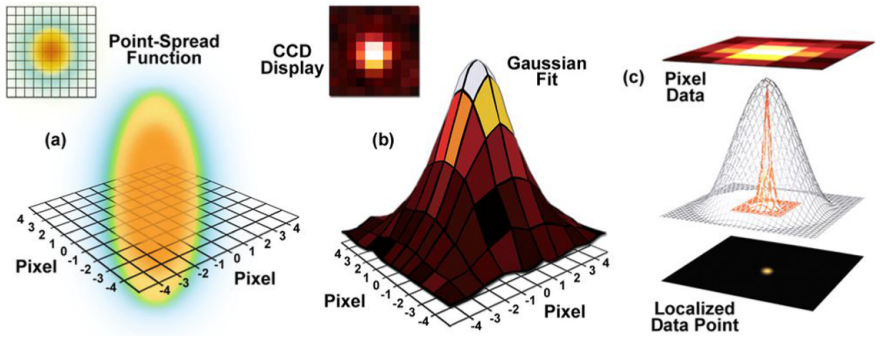

Figure 1.23: Single-molecule localisation procedure via fitting the PSF to a Gaussian function. (a) The PSF of a widefield fluorescence microscope is composed on a wireframe representation of (b) the pixel arrangement from a digital camera in two and three-dimensional diagrams. (c) The pixelated PSF of a single fluorophore and its localisation point modelled by a 3D Gaussian function [75].

vated localisation microscopy, (PALM) [60], fluorescence photoactivation localisation microscopy (FPALM) [61] and stochastic optical reconstruction microscopy (STORM) [62]. While the photoactivatable green fluorescent protein is used as the fluorescent probe in PALM and FPALM, photo-switchable dye pairs are used in STORM.

The fundamental concept anchoring these techniques is that if enough photons can be gathered, the position of a single molecule can be localised with the accuracy of a few nanometres (Figure 1.22). Localisation accuracy does not directly translate into super-resolution images due to overlapping of fluorophores that emit light simultaneously in densely labelled specimens. To prevent this from happening and to break this "ensemble nature" of fluorescent labels, PALM and STORM are designed in such a way that they can precisely localise individual single-molecule emitters by switching the fluorescence "on" in groups of molecules before attempting to locate them. This technique relies on stochastic photoswitching, where most molecules remain dark. When radiated with excitation light at low power, molecules are stochastically switched on, imaged, localised and then photobleached to remove them from this group. This process is repeated in cycles to reproduce thousands of images of localisations and layer them into a single image, allowing the construction of a super-resolved image.

Identifying and localising single molecules were done on the basis of an area consisting of single-molecule emitters. By gathering a number of photons, the central

section of each diffraction-limited spot, recorded on a digital camera image plane, corresponds to the position of a molecule, and which can be localised by a high nanometric position. Using statistical curve-fitting of the measured photon distribution to a Gaussian function, the centre of localisation can be determined (Figure 1.23). In cases where two single-molecule locations overlap with a separation distance shorter than the diffraction limit, the centroid for each fluorophore can be individually localised by subtracting the point-spread function of one fluorophore from the other (after it is photobleached).

There are three main factors that affect the final resolution in this method: (i) the fluorophore size, (ii) labelling density, and (iii) localisation precision. It is obvious that the resolution cannot be improved better than the size of probe used for fluorescence labelling. In addition, the labelling density of the probes and how well each of them can be localised later, i.e. localisation precision, determines the resolution limit.

The effect of labelling density on the resolution has been best described by the Nyquist sampling theory, which states that the minimum sampling rate must be twice the frequency of the highest frequency component of the signal detected in order to faithfully reconstruct the signal [68, 76, 77]. Thus, the minimum required molecular density for a resolvable feature is described by:

$$\Delta_{N_y} = \frac{2}{N^{\frac{1}{D}}} \tag{1.9}$$

where N is the labelling density, D is the dimension of the structure that is to be imaged. This can be clearly illustrated by the fact that 10^4 probes per μm^2 are required to achieve a 20 nm resolution on a two-dimensional image.

As for localisation precision, the most commonly used method for the localisation of the centroid of the PSF is to apply a two-dimensional Gaussian fit. Localisation precision (σ) can be approximated by the following equation:

$$\sigma \approx \frac{F_{PSF}}{\sqrt{N_p}} \tag{1.10}$$

where σ is the single-molecule localisation precision, F_{PSF} is the FWHM of PSF, and N_p is the photon number. Thus, it is clearly expected to achieve a higher resolution when a microscope system has a small PSF and bright fluorophores (i.e. more photons from the probes).

1.5.4 Fluorophores used in super-resolution imaging

Currently, the most common approach for imaging in biological systems is based on fluorescent dyes and proteins. The probes that are used in SR need to have several properties: (1) they have to be photoactivated (i.e. can be switched from light to dark state by changing the wavelength of light); (2) they should a have high contrast ratio between these states; (3) they should be sufficiently bright to be detected. As Thompson and his colleagues mentioned [78], the number of photons detected is important in single-molecule SR techniques that rely on localisation precision. Furthermore, STED dyes should be (a) easily switched to stimulated emission, (b) photostable at high intensities of light, and (c) should not excite at the depletion wavelength.

1.6 Examples of structures of interest in super-resolution microscopy

Since the invention of different super-resolution strategies, they have been used in imaging of plenty of structures and dynamics inside the cell. Among them, microtubules are one of the widely studied structures as test subjects in SR imaging due to their importance in cells and being continuous structures at sub-diffraction level. In this thesis, we aimed to observe microtubules of a kidney cell and proteins localised around the synaptic cleft of a neuron to test our labelling strategies rather than understanding their structure. Thus, the structures of microtubules and neurons will be discussed and examples in SR will be given in the next sections.

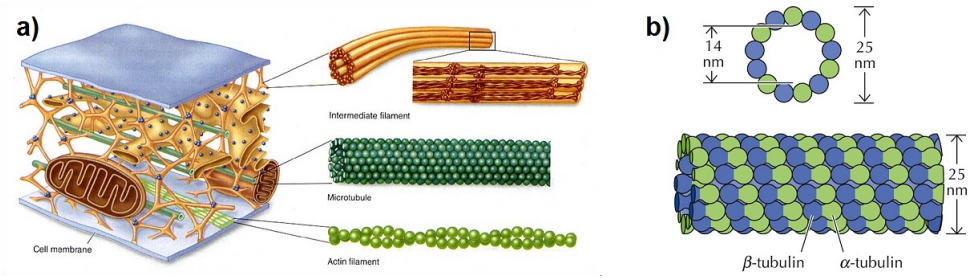

Figure 1.24: (a) The cytoskeleton is a networking system between the two membranes [79] and (b) Cross-section of a microtubule that is composed of alpha- and beta-tubulin dimer [18]

1.6.1 Microtubules

Microtubules are part of a cytoskeleton, which is a structure made up of a complex network of filaments and tubules in the cytoplasm of the cell. The cytoskeleton extends throughout the cell from one side to the other and has a plenty of functions, such as maintaining the shape of the cell, and other internal organisations, to carry out essential functions like endocytosis (uptake of an extracellular material), segregation of chromosomes in cellular division and intracellular transportation (as a scaffold for the movement of vesicles) [18].

In eukaryotic cells, there are three main types of cytoskeleton elements that vary in size and protein composition: (i) actin filaments, (ii) intermediate filaments and (iii) microtubules. Actin filaments are made up of a protein called Actin, and they are the smallest type of filament with a diameter of around 7 nm. Intermediate filaments, on the other hand, are mid-sized filaments with a diameter of about 10 nm and constructed of various protein families. As for microtubules, they are hollow cylinders that are mainly composed of two proteins: alpha- and beta-tubulin. While the outer diameter of the microtubule cross-section is approximately 24 nm, the inner diameter of the lumen is about 12 nm.

Microtubules are highly dynamic structures. They are continuously extended or shortened via constant adding or subtracting of the tubulin dimers at both ends (Figure 1.24). The microtubules tend to grow and branch out from the Microtubule Organising Centres (MTOC), such as centrosome, where one side of the microtubules

is anchored to near the nucleus, towards the plasma membrane, and they provide the basic arrangement of the cytoplasm and location of organelles [80]. For the initiation of the formation of the microtubule, gamma-tubulin, another form of tubulin found in the MOTC, plays a key role in the process of microtubule nucleation. It combines with other proteins to create a structure known as the gamma-tubulin ring complex (γ-TuRC). After γ-TuRC formation, the tubulin dimers (alpha- and beta-tubulin) use it as a platform to polymerise in the formation of microtubules. These protein dimers are added end to end laterally to form a microtubule, and the hollow tube structure of the microtubule results from the polymerisation of these building blocks. One turn of a pseudo-helical structure is generated when thirteen tubulin dimers associate laterally, and these polymers of tubulin can grow up to 50 micrometres.

The assembly of dimers leads to polarity in the structure of microtubules, and the rate of growth or shrinkage at either side of the structure varies; whereas the one end that has beta subunit exposed, known as plus end, grows more rapidly than the other end that has alpha subunit exposed, also known as minus end. Polymerisation of the structure occurs via binding of both subunits to Guanosine triphosphate (GTP) and follows hydrolysis of GTP to Guanosine diphosphate (GDP). In case of a low concentration of tubulin bound to GTP, the GTP bound to the tubulin at the plus end hydrolyses to GDP, resulting in rapid depolymerisation and shrinkage of the microtubule [18].

As mentioned above, microtubules provide structural support for the cell. In addition to their structural supporting function, they serve as a highway system for the secretory vesicles, organelles, and other intracellular macromolecules to be transported along, with the aid of motor proteins. Different motor proteins can attach to vesicles and walk along the microtubules. While dynein proteins walk towards the MTOC, kinesins walk away from the MTOC. What is more, microtubules have a structural role in cilia and flagella, which generate force for cells to swim or move extracellular materials past them. They are composed of two central microtubules (Axoneme) that are surrounded by nine outer doublets microtubules. Their structural bending shape helps cells propel through a fluid or move the fluid across them.

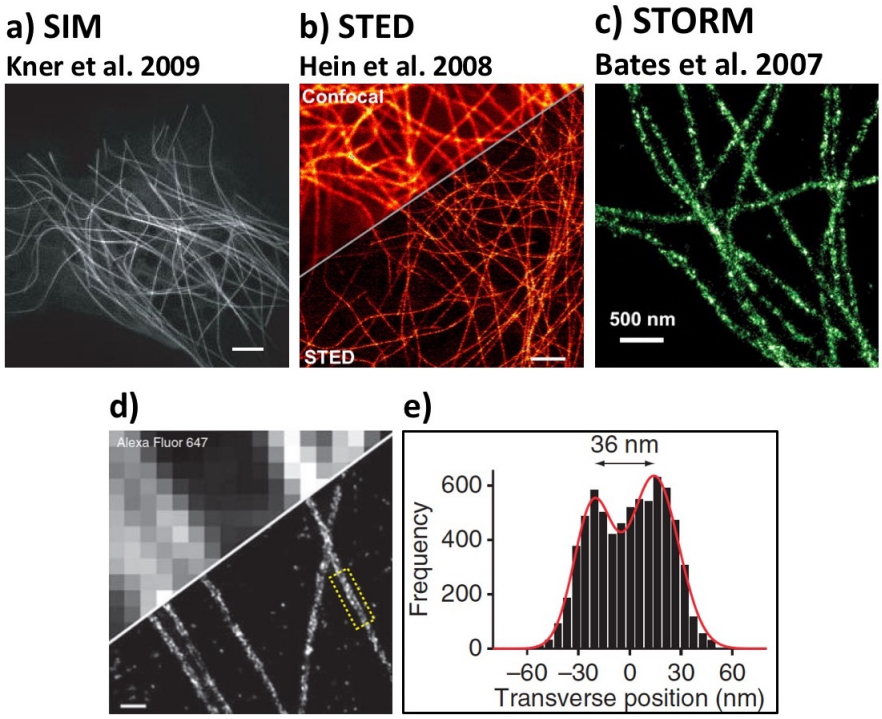

Figure 1.25: Example images of microtubules in the current SR methods: (a) structured illumination microscopy (SIM) [81], (b) stimulated emission depletion (STED) microscopy [82] and (c) stochastic optical reconstruction microscopy (STORM) [83]. (d) Partially overlaid conventional fluorescence image (top left) and STORM image (bottom right) of microtubules immunostained with Alexa Fluor 647 and (e) transverse profile of localisations seen in yellow box in (d) [84]. Scale bars are 500 nm in (a-c) and 250 nm in (d).

Furthermore, microtubules have a key function in mitosis. During the replications and separation of chromosomes, the centrosome is duplicated in the interphase cell, then they move to opposite sides of the nucleus and form the two poles of the mitotic spindle. Meanwhile, condensed chromosomes are lined up in pairs in the centre of the cell and microtubules bind to centromeres, the region at which the two sister chromatids remain attached at metaphase, on either side. As the microtubules begin to disassemble and shrink from the minus end at centrosomes, the chromatids are pulled apart in the direction of the two centrosomes before cytokinesis (the division of cell) takes place.

Since microtubules have an extremely important role in the maintenance of cells as described above, they have been investigated and studied for decades. In addition to their well-known structures and functions, the continuity of their structure, ease of

targeting and labelling of their subunits (such as alpha-tubulin) by fluorophores and having a diameter smaller than the diffraction limit, microtubules have become one of the biological reference structures in super-resolution imaging [81–89].

In the study of Peter Kner and his colleagues in 2009, they imaged EGFP-fused alpha-tubulin in living Drosophila S2 cells (intensity: 5–10 W/cm^2), and they showed that isolated microtubules could be reconstructed with a FWHM of 112$\pm$12 nm and two microtubules separated by 150 nm can be resolved in the SIM construction (Figure 1.25a) [81]. As a second example, STED and confocal images of citrine-fused microtubules of a living PtK2 cell are shown in Figure 1.25b [82]. Here, Hein et al. improved the lateral resolution from 180 nm to 60 nm (at illumination intensity of >62 MW/cm^2). In 2007, Bates et al. have imaged anti-beta-tubulin labelled microtubules with a FWHM of approximately 51 nm and two filaments 80 nm apart appeared in the STORM image, which was acquired in 2-30 minutes (Figure 1.25c) [83]. As for the STORM image captured by Dempsey et al. in 2011, even the hollowness structure of microtubule could be observed as seen in the transverse profile analysis of STORM image in Figure 1.25d and e [84].

In the next section, the structure of neurons will be described, and several examples of their images in SR microscopy will be illustrated.

1.6.2 Neurons

The brain is the most complex biological system in the human body, consisting of about 100 billion nerve cells (neurons). Each neuron is made up of a soma (cell body), dendrites and axon (Figure 1.26) [90]. The soma, main body of the cell, is usually about 10 to 25 micrometres in length and contains the nucleus. The dendrites are the branching parts of the cell, and the axon is the extension part, arising from the cell body, and can be elongated to a metre or more in a human body [91]. The axons can be either myelinated or unmyelinated. Myelin is a layer of insulating substance, which is produced by Schwann cells (in peripheral neurons) or oligodendrocytes (in the central nervous system), and it enables rapid propagation of the electrical impulse along axons [92]. Whereas the axon serves the cell as the single output of the signal

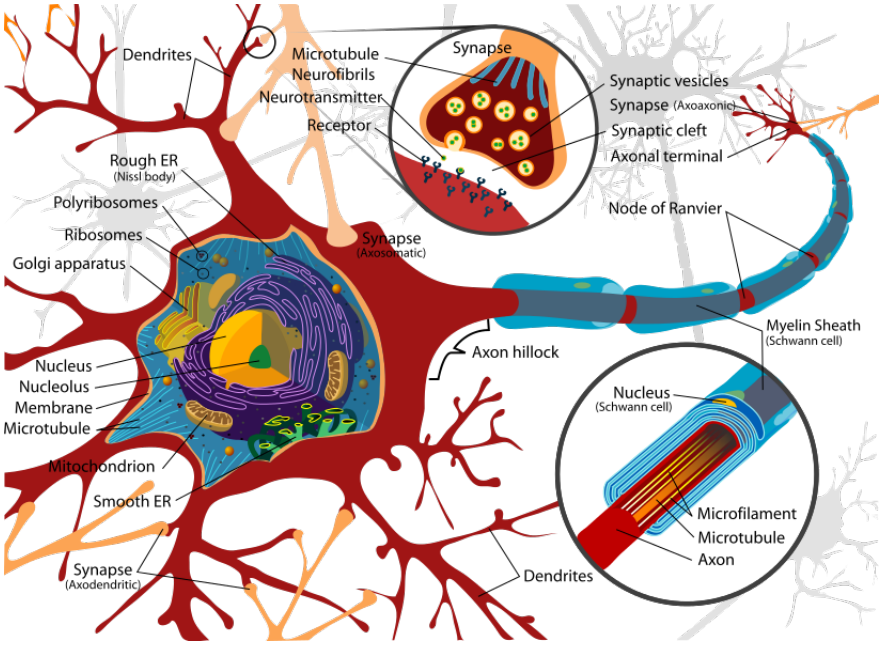

Figure 1.26: Diagram of a neuron, illustrating the soma, dendrites, axon and synapse. Each neuron has many inputs (dendrites) and only a single output (axon). Illustration of the synapse and synaptic cleft also visible [90].

to the other cells, the dendrites serve as inputs of the impulses coming from many other cells to the cell. All neurons can be electrically excited, and the nature of the transmitted information can be electrical and chemical signals. When a neuron is excited by an external stimulus, it transmits electrical pulses down the axon using ion pumps embedded in the membrane, and the impulse is transferred to the next neuron through the synapse. The synapse is a narrow gap structure, where a neuron passes electrochemical signals to another nerve cell. The width of this extracellular space, also known as the synaptic cleft, is about 20 nanometres [93]. The signal is converted into a chemical signal, the neurotransmitters, by the presynaptic neuron. Then the neurotransmitters travel through the synaptic cleft to the receptors of the postsynaptic neuron and are converted back into an electrical signal.

Synapses are very crucial structures in neuron communication, and that is why there are so many neurological disorders, such as autism and Alzheimer's disease, associated with the disfunction of proteins, receptors and other structures around the synapses [94]. Therefore, it becomes very important to study them, and be able to image them in super-resolution using optical microscopy, because the distance

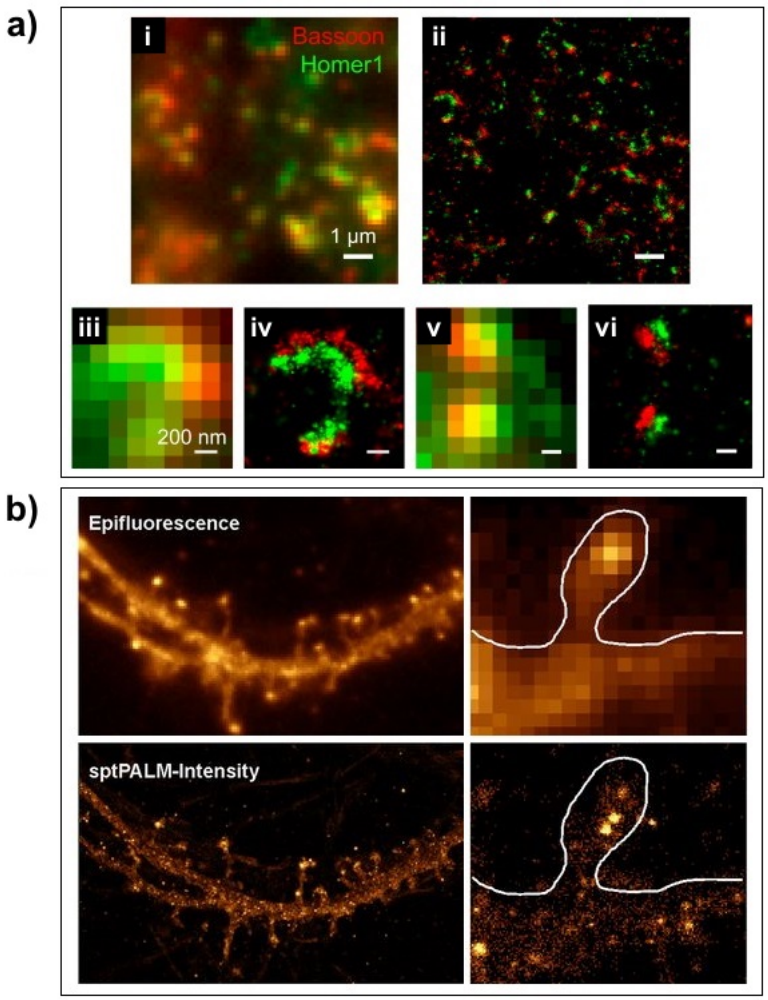

Figure 1.27: (a) The conventional fluorescence image (i) and the STORM image (ii) of the synaptic structures, and zoomed in images (iii,v) of (i) and (iv,vi) of (ii) [95]. (b) Comparison between fluorescence imaging and super-resolution imaging of AMPAR localisation [96].

sizes between the proteins and receptors are below the diffraction limit. Additionally, co-imaging of more than one structure around the synaptic cleft at the same time is essential if the relation between two or more proteins/receptors is to be studied. Here, multicolour super-resolution imaging is taken into consideration, in which more than one structure is labelled with different fluorophores and the images are taken at the same time in different channels, rather than overlaid to produce one image in order to show the structural and localisational relationship between the structures (Figure 1.27) [95–98].

Among these proteins and receptors, here, we will give two SR imaging examples

of neurons. Figure 1.27a shows multicolour STORM images of Bassoon, a presynaptic scaffolding protein, and Homer1, a postsynaptic scaffolding protein, published by Dani et al. in 2010. Bassoon, together with Piccolo, has an important role in the localisation of voltage-gated Ca^{2+} channels around the release sites, and regulates the activity-dependant communication between synapses and nucleus [99, 100]. Similarly, Homer1 has a key function in regulation of receptor trafficking and clustering via interacting with other scaffold proteins such as Shank and PSD-95, and it enhances the distribution and signalling of N-methyl-D-aspartate receptors (NMDARs) and alpha-amino-3-hydroxy-5-methylisoxazole-4-propionate receptors (AMPARs), which are very important for controlling synaptic plasticity and memory function [101, 102]. In the structural position analysis done by Dani and his colleagues, while Bassoon and Homer1 were shown to be localised within a distance between 90 nm and 170 nm in the vicinity of synapses, the distance between Piccolo and PSD95 was found about 50-160 nm, [95]. What is more, in the study of Nair et al. in 2013, they showed AMPARs localisations in nanodomains with an image resolution of 46.6 nm, and their individual trajectories along the neuronal surface using "single particle tracking photoactivation localization microscopy", where imaging took up to 20 minutes (Figure 1.27b) [96].

In the following section, the drawbacks of currently used SR microscopies will be discussed, and a different labelling strategy to solve the current problems will be introduced.

1.7 Limitations of current super-resolution microscopies

Although there has been significant progress in the optical resolution of microscopes over the last two decades, as described above, the majority of currently used methods (e.g. STED, PALM, STORM) have a number of drawbacks. While STED microscopy has been shown to deliver resolution down to a few nm [69], with image recording times ranging from a few milliseconds to a few seconds, this approach generally requires very high levels of light intensities (Table 1.1), which leads to photobleaching

Table 1.1: Comparison of acquisition time and laser intensities currently used in STED/GSD/RESOLFT and PALM/FPALM/STORM/GSDIM [68, 71, 72].

Name	STED/GSD/RESOLFT	PALM/FPALM/ STORM/GSDIM
Total Imaging Time (for 512x512 image)	Millisecond – Seconds	Seconds – Minutes
Intensity of Laser on sample	600 Wcm^{-2} – 10 $MWcm^{-2}$	200 Wcm^{-2} – 30 $kWcm^{-2}$

of fluorophores and damages to the live specimens [73]. On the other hand, whereas SMLM techniques (e.g. PALM, STORM and their variants) require much lower light intensity to stochastically turn on a small sub-group of fluorophores for delivering resolution down to a few nm, relatively slow data acquisition times are required in PALM/STORM (from seconds to several minutes, see Table 1.1) in order to obtain a single super-resolution image [72]. Here, the sample drift problem and insufficient time resolution for the live cell imaging are taken into consideration, in order to overcome this. Therefore, current super-resolution techniques still require considerable improvements for faster acquisition at lower intensities, which we worked to achieve in this thesis, using spectral separation of QDs.

It has been suggested that in general, almost any variation in the photophysical properties of fluorophores [103] (e.g. photo-switching [104], photobleaching [105], blinking [106], fluorescence lifetime [107] and spectral differences [108]) can be used for super-resolution microscopy. In case of spectral signal separation, in particular, the temporal resolution can be vastly improved [109] and is only defined by the signal-to-noise ratio, which in turn depends on the balance between illumination intensity and fluorophore quantum yield. It has been shown previously that high precision (σ <1 nm) localisation of organic fluorophores can be achieved by using spectral precision distance microscopy (SPDM) [110]. However, this required a specialised microscope set-up with the number of excitation wavelength growing proportionally to the number of fluorophores (of different emission wavelength).

On the contrary, with the advantages of QDs over organic fluorophores including broad excitation and narrow, tuneable emission spectra controlled by particle size, QDs have been widely used for different types of labelling studies for decades [111]. In

addition to them, QDs are highly resistant to photobleaching. For the purpose of super-resolution imaging, blinking statistics and blueing of QDs have been demonstrated to be used in a variety of super-resolution methods [106, 112]. Recently, it has been shown that a combination of spectral and blinking properties of QDs can be employed by using Joint Tagging Super-Resolution Optical Fluctuation Imaging (JT-SOFI) [87]. However, so far the majority of SR methods rely on photoluminescence intermittency, which is stochastic in nature, hence requires hundreds to thousands of images to be collected to obtain a single SR image.

To alleviate these constraints, it has been proposed that super-resolution imaging can be achieved using only the spectral properties of the size-dependent light emission of QDs [113, 114]. In this thesis, we suggest and test a new labelling method: quantum dot-based optical spectral separation (QDOSS), which will be described in detail in chapter 2, on several biological reference structures *in vitro*.

Chapter 2

MATERIALS AND METHODS

2.1 Quantum Dot-Based Optical Spectral Separation (QDOSS)

Quantum dot-based optical spectral separation (QDOSS) relies on the "spectral separation", rather than "temporal separation" of QDs with the size-dependence of the peak emission wavelength (Figure 2.1), and localisation and identification of a random mixture of different-sized QDs in different emission channels to achieve super-resolution imaging. In the spectroscopic super-resolution bio-imaging principle, a bio-sample is

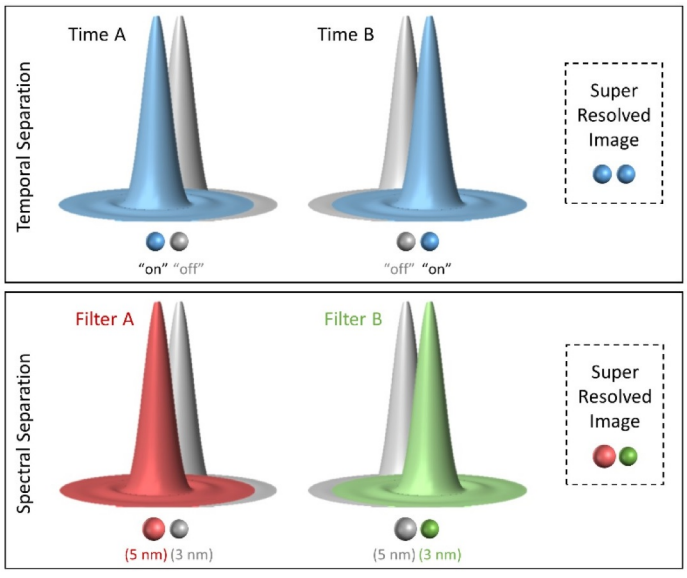

Figure 2.1: Schematic representation of temporal separation and spectral separation.

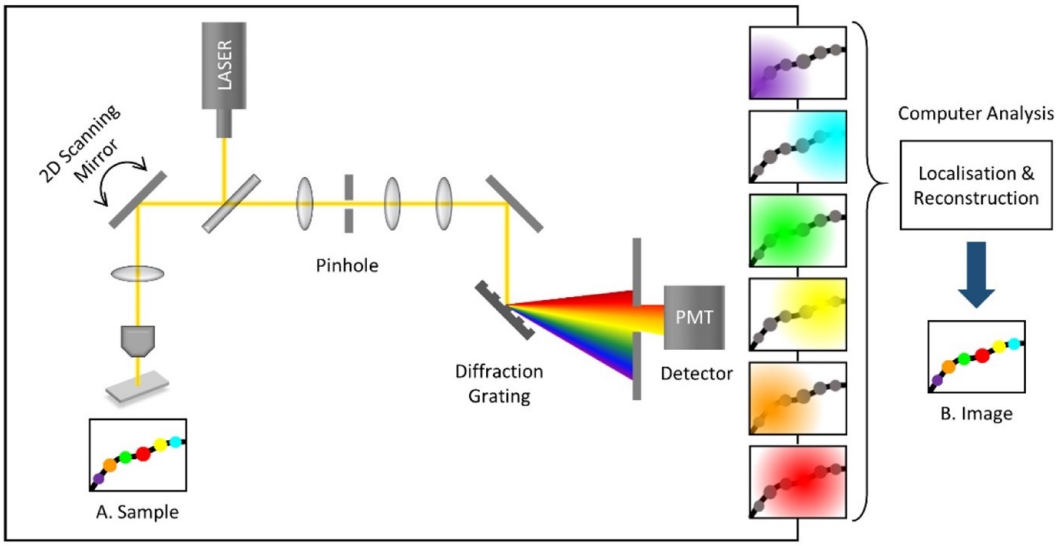

Figure 2.2: Schematic representation of a laser scanning confocal microscope (LSCM) and the strategy of how LSCM is used in QDOSS.

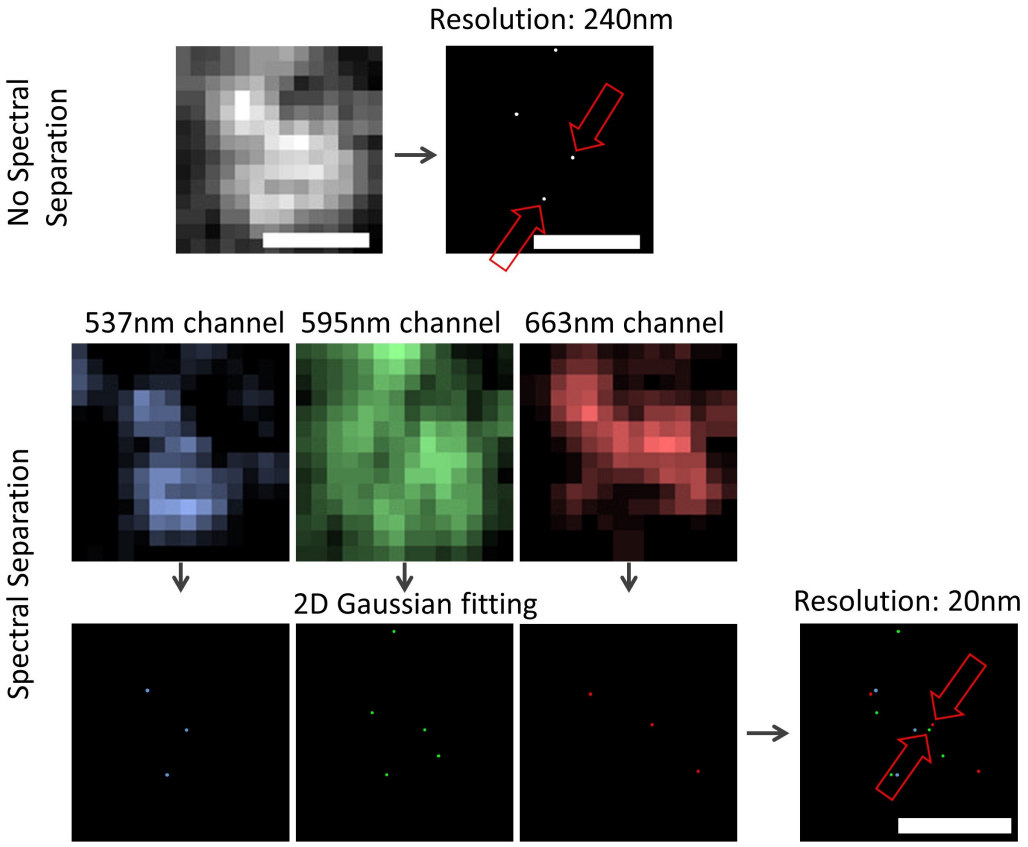

Figure 2.3: 2D Gaussian fitting based on the Levenberg-Marquardt method using GDSC-SMLM. Localisation accuracy: 5±1 nm. Scale bar: 500 nm. Figure sourced from [115].

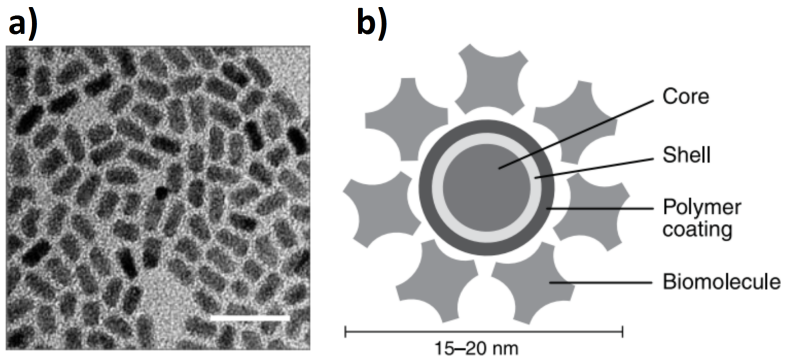

Figure 2.4: (a) Transmission electron microscope image of Qdot® nanoparticles. Scale bar = 20 nm. (b) Schematic structure of a Qdot® streptavidin conjugate. Figure sourced from [116].

labelled with a mixture of a few different-sized QDs that have different peak emission wavelengths. After excitation of QDs on the sample, fluorescence emission light is transferred to a series of filters, where the image is spectrally separated into different channels, and finally arrives to the detectors that collect specific wavelength signals. These spectroscopic separated diffraction spots are later localised in order to reconstruct the sub-diffraction resolution image (Figure 2.2).

In previous studies by our group, Mingying Song has demonstrated that a mixture of different-sized non-modified germanium QDs can be resolved down to 20 nm using the Levenberg-Marquardt method for a 2D Gaussian fitting model [115]. In Figure 2.3, it is seen that the resolution limit is 240 nm if the image is not spectrally separated, whereas the resolution is found down to 20 nm if the 2D Gaussian fitting model is applied to each image from different channels. This model is the basis of the next studies in this thesis.

2.2 Quantum dots

In this study, Qdot® streptavidin conjugates from Invitrogen, USA, are used as labelling fluorophores. The off-the-shelf quantum dots are made from a semiconductor material core, CdSe, and coated with an additional semiconductor shell, ZnS, which helps to improve the optical properties of the material. This core-shell material also has a polymer shell with streptavidin on its surface. This allows the materials to

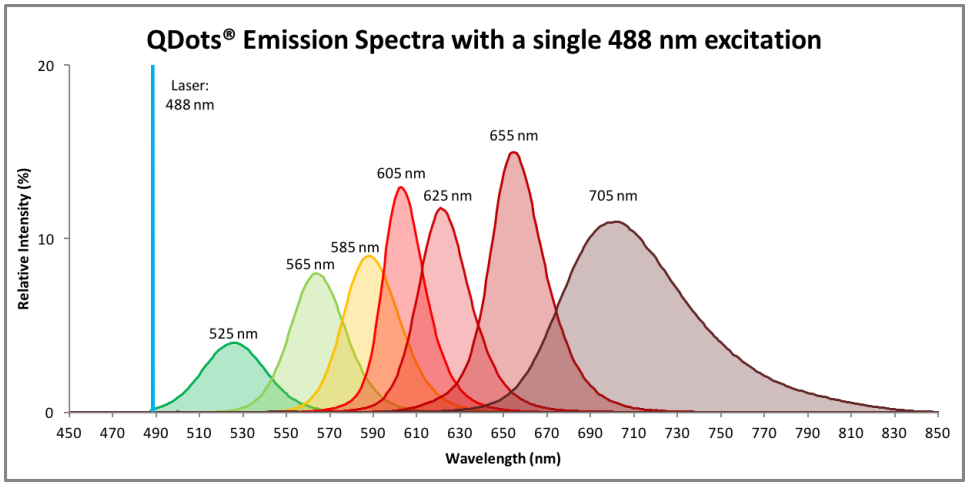

Figure 2.5: Emission spectra of Qdots® with a single 488 nm excitation.

be conjugated directly to biological molecules. The sizes of the Qdot® streptavidin conjugates vary between 15 nm and 20 nm (Figure 2.4). The QDs have an emission spectrum with the emission maximum at 525 nm, 565 nm, 585 nm, 605 nm, 625 nm, 655 nm or 705 nm. In Figure 2.5, the emission spectra of seven types of QDs with relative intensities under 488 nm excitation are seen.

In the final stage of the study, in-house made novel carbon QDs (CQDs) were used. The bench-top colloidal synthesis of CQDs was carried out by my colleague, Nikolaos Papaioannou.

2.3 QDOSS testing on DNA

In order to test the idea of QDOSS, we first used 180 base pairs (bp) long ssDNA as a reference and then triangular DNA origami as a template for attaching different QDs within sub-diffraction distance.

2.3.1 DNA ruler

Because targeting a long single stranded (ss) DNA by streptavidin conjugated QDs modified with small oligonucleotides is easy to perform, we first tested QDOSS on a long ssDNA with a length of 180 bp. The sequences of the nucleotides and their purification methods are seen in Table 2.1. While the long one (TP53-CDNA) was

Table 2.1: List of single stranded DNAs.

Oligo Name	Sequence (5′-3′)	Purification
NPBIOTIN-1	Biotin - A A A A A A A A A A C G C T A G C A G A G C C G A G A T	HPLC
TP53-CDNA	T T C G A C A T A G T G T G G T G G T G C C C T A T G A G C C G C C T G A G G T T G G C T C T G A C T G T A C C A C C A T C C A C T A C A A C T A C A T G T G T A A C A G T T C C T G C A T G G G C G G C A T G A A C C G G A G G C C C A T C C T C A C C A T C A T C A C A C T G G A A G A C T C C A G T G G T A A T C T A C T G G G A C G G A A C A G C T T T G A G G	HPLC
TP53-11	A C C T C A G G C G G C T C A T A G G G C A C C A C C A C A C T A T G T C G A A A T C T C G G C T C T G C T A G C G	Desalted
TP53-12	A C A C A T G T A G T T G T A G T G G A T G G T G G T A C A G T C A G A G C C A A T C T C G G C T C T G C T A G C G	Desalted
TP53-13	G G A T G G G C C T C C G G T T C A T G C C G C C C A T G C A G G A A C T G T T A T C T C G G C T C T G C T A G C G	Desalted
TP53-14	A G T A G A T T A C C A C T G G A G T C T T C C A G T G T G A T G A T G G T G A A T C T C G G C T C T G C T A G C G	Desalted
TP53-6	C C T C A A A G C T G T T C C G T C C C A T C T C G G C T C T G C T A G C G	Desalted

purchased from Sigma, the others were purchased from Life Technology (USA). TP53-CDNA was used as a template for short ssDNAs: TP53-11, TP53-12, TP53-13, TP53-14 and TP53-6. Each short ssDNA has a tail that has complementary sequences with NPBIOTIN-1, which is biotinylated at its 5′ end. For programmed assembly of QDs, after the surface of each quantum dot (Qdot® 525 Streptavidin Conjugate, Invitrogen, Qdot® 705 Streptavidin Conjugate, Qdot® 585 Streptavidin Conjugate, Invitrogen, USA) was modified by NPBIOTIN-1, they were mixed with TP53-11, TP53-13 and TP53-6, respectively, in separate tubes and shaken at room temperature for 1 hour for hybridisation in the presence of Mg^{2+} (Magnesium Chloride: 12.5 mM; pH 7.8). Finally, 10 μL of the prepared samples were deposited onto the surface of coverslips before being observed under microscopes.

2.3.2 Triangular DNA origami

After using a long ssDNA as a template, we used triangular DNA origami with a side length of 120 nm because of its well-rigid structure, which enabled us to estimate the accurate distances between QDs. The sequences of the triangular DNA were

taken from the study of Zhang and his colleagues, and can be found in Appendix A [117]. M13mp18 ssDNA was purchased from Affymetrix, USA, and unmodified 220 staple strands and 6 modified staple strands were purchased from Integrated DNA Technologies, UK (see Table A.1 and A.2 for the sequences, respectively).

Three staple strands on the middle positions of the sides were modified, and extended with unique sequences for programmed assembly of three different streptavidin conjugated QDs, with maximum emissions at 525 nm, 605 nm and 655 nm (Qdot® 525 Streptavidin Conjugate, Invitrogen, Qdot® 605 Streptavidin Conjugate, Qdot® 655 Streptavidin Conjugate, Invitrogen). Each of these QDs was functionalised with a different biotin modified ssDNA, complementary to the sequences that extended from the sides of the aforementioned triangular DNA origami. Two or three different types of QDs were then attached to DNA origami. In this arrangement, the distance between the middle positions of the sides is approximately 60 nm, by design. Triangular DNA origami nanostructures were assembled according to the method from Rothemund's work [118].

M13mp18 ssDNA (1 $\mu g/\mu L$) and 220 staple strands (100 μM) (see Appendix A) were used in a 1:10 molar ratio. Strands were mixed to meet a final condition of 1× TAE-Mg^{2+} buffer (Tris: 40 mM; Acetic Acid: 20 mM; EDTA: 2 mM; Magnesium Chloride: 12.5 mM; pH 7.8) in a PCR tube. Hybaid Sprint PCR Thermal Cycler (Thermo Scientific, USA) was used for programming controlled steps cooling down the strands mixture from 94 °C to room temperature over 10 hours. The assembled DNA origami were purified and concentrated by 100K NMWL centrifugal filters (Amicon® Ultra-0.5, Millipore, Ireland). The concentration was adjusted to 20 nM using a molecular weight of 330 g/mol per base and an extinction coefficient of 50 mg/ml for A 260 = 1 in a NanoDrop Spectrophotometer (NanoVue™ Plus, GE Healthcare, UK).

Two different QDs (Qdot® 605 Streptavidin Conjugate, Qdot® 705 Streptavidin Conjugate, Invitrogen, USA) or three different QDs (Qdot® 525 Streptavidin Conjugate, Invitrogen, Qdot® 605 Streptavidin Conjugate, Qdot® 655 Streptavidin Conjugate, Invitrogen, USA) were used in the 2-QD-bound or 3-QD-bound system, respectively.

They were assembled to each specific and distinct biotinylated ssDNA sequence by biotin-streptavidin linkage. Qdot:ssDNA molar ratio was 1:100. Excess ssDNA was removed by membrane filters (0.025 μm VSWP Membrane Filter, Millipore, Ireland). QD-ssDNA conjugate probes were mixed with triangular DNA origami under 1:1 molar ratios. Mixtures were slowly cooled down from 47 °C to room temperature overnight in a water bath to anneal three different QDs on triangular DNA origami. The prepared samples were deposited onto freshly cleaved mica and left to adsorb on the surface for 2 minutes before observing them under microscopes.

2.4 Cell culture

Following DNA template tests, we imaged alpha-tubulin structures in HEK293T cells and several receptors and proteins in neurons.

2.4.1 Alpha-tubulin imaging

The HEK293T cell line, which is a human embryonic kidney cell line, was used as a model. The cells were provided by Prof Gleb Sukhorukov (School of Engineering and Materials, QMUL). HEK293T cells were grown in Dulbecco's modified Eagle medium and supplemented with 10% FCS, 1% Pen/Strep and 1% L-Glutamine in 50 mL culture flasks at 37 °C in the presence of 5% CO_2. Sub-culturing was performed twice a week with a splitting ratio of 1:10. The density of cells used in imaging experiments was $5x10^4$ cells per mL. The cells were seeded on poly-L-lysine-coated coverslips (0.13 to 0.17 mm thick) in a 12-well plate for overnight before use.

2.4.2 Neuron imaging

In order to use QDOSS on a real biological system, we aimed to observe the distribution of the receptor clusters of NMDAR and AMPAR, which are receptor proteins in the postsynaptic region of the nerve cells. Furthermore, we also applied our method to observe the distribution of the presynaptic scaffolding proteins (Bassoon and Piccolo) and postsynaptic scaffolding proteins (Homer1 and PSD95) located around

the synaptic cleft. Neurons were obtained from Prof Dmitri Rusakov, (Institute of Neurology, University College London). They were prepared from acute hippocampal transverse slices (350 μm thick) of male rats, and fixed by 4% paraformaldehyde (Thermo Scientific) on poly-L-lysine-coated coverslips (0.13 to 0.17 mm thick).

2.5 Microscopy

In this thesis, we used Atomic Force Microscope (AFM) to verify one of the results found in QDOSS (DNA origami) and Laser Scanning Confocal Microscope (LSCM) for testing the QDOSS approach. Besides, a super-resolution microscope was used for comparison of QDOSS with currently used super-resolution technique (STORM).

2.5.1 Atomic Force Microscopy

5 μL of QDs modified triangular DNA origami (with a 1X TAE-30 mM Mg^{2+} buffer) were deposited onto freshly cleaved mica and left to adsorb to the surface for 2 minutes. Ultra-Pure water (18Ω, Millipore) was used to wash the mica surface, followed by a blow dry via compressed air prior to AFM imaging. The modified DNA origami were imaged by AFM using ScanAsyst Mode (Dimension Icon with ScanAsyst, Bruker).

2.5.2 Laser Scanning Confocal Microscopy

For the QDOSS imaging process, a Leica TCS SP2 Inverted Laser Scanning Confocal Microscope, equipped with a 488 nm Ar Laser (125 mW) and two PMT detectors, was used (Figure 2.6).

Images were taken under HCX PL APO 63X/1.40 (Oil) objective. Scanning formats were selected according to priority of image in terms of quality or data acquisition time, high (e.g. 4096-pixel) or small (e.g. 256-pixel), and line:frame averages were taken (e.g. 2:3, i.e. 2-line-average and 3-frame-average were taken for the image of one channel) or not (e.g. 1:1). The emission range of each channel was adjusted according to the FWHM of each QD type, and different colours were assigned to each QD to differentiate one from the other. For comparison of spectrally separated

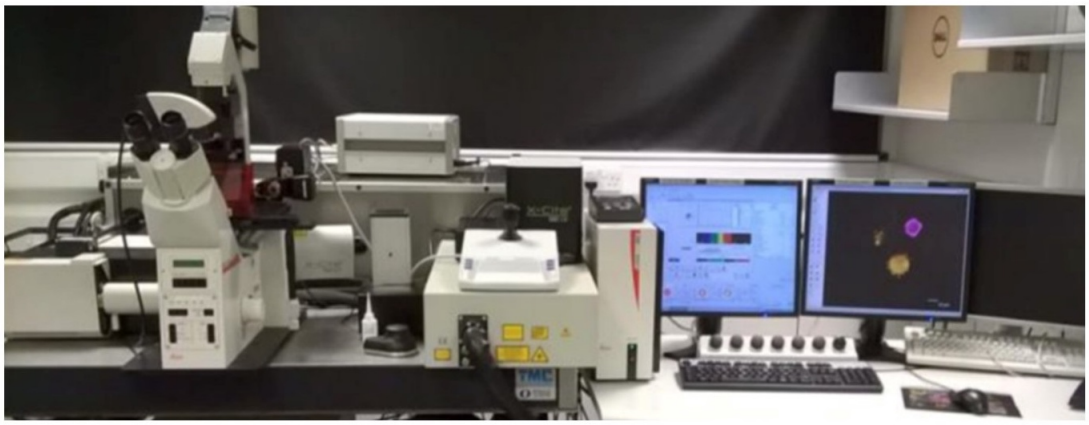

Figure 2.6: Leica TCS SP2 laser scanning confocal microscope (LSCM) equipped with a 488 nm Ar Laser (125 mW) and two PMT detectors.

Table 2.2: Data acquisition time (seconds) depend on scanning rate and line:frame averaging.

Scanning Rate		**400 Hz**			**800 Hz (or Bidirectional 400 Hz)**		
Line:Frame Averaging		**1:1**	**2:1**	**2:2**	**1:1**	**2:1**	**2:2**
Pixel Size (px)	**4096**	10.24	20.48	40.96	5.12	10.24	20.48
	2048	5.12	10.24	20.48	2.56	5.12	10.24
	1024	2.56	5.12	10.24	1.28	2.56	5.12
	512	1.28	2.56	5.12	0.64	1.28	2.56
	256	0.64	1.28	2.56	0.32	0.64	1.28

super-resolution imaging between non-spectral imaging, all QDs were observed in one channel as well. The parameters were saved for each channel, and then the channels were added to sequential scan mode in Leica Confocal Software (v2.1), which provides images to be taken in series. The pixel sizes depended on the image size and scan format, and were calculated by dividing the size of the scan field by the size of the scan format. For instance, the scan field is 10.17 μm under 63X objective with a zoom factor of 23.4, and if scan format of 256x256 is selected, the pixel size will be (10.17 μm/256=0.03972 μm) about 40 nm. As far as the data acquisition time of the image is concerned, it is calculated by dividing the size of the scan format by the scan rate, which was set to 400 Hz. If there is no line or frame average taken, the data acquisition time will be (256-pixel/2x400 Hz=0.32 seconds) 320 milliseconds.

2.5.3 Super-resolution Microscopy

For comparison of the QDOSS approach, we used Zeiss Super-resolution LSM 710 ELYRA PS.1, which is a combination of laser scanning confocal microscopy and super-resolution imaging microscopy with TIRF. The samples were excited by HR Diode 488 nm (100 mW) Laser. The images were taken under PL APO 100X/1.46 Oil DIC M27 objective and the data acquired by Andor iXon 897 EM-CCD camera in a 512x512 pixel format with a pixel size of 16 μm. 10,000 images were taken with an exposure time of 45 ms, so the all data acquisition time took more than 7.5 minutes for a single super-resolved image. The raw data of the images were analysed by the software Zen 2010D (Carl Zeiss Microscopy, Jena, Germany).

2.6 Analysis

Raw image data from experiments were analysed by the ImageJ (v1.48) plugin, Genome Damage and Stability Centre-Single Molecule Localisation Microscopy (GDSC-SMLM) (v3.1) (Available at: http://www.sussex.ac.uk/gdsc/intranet/microscopy/imagej/smlm_plugins). A 2D Gaussian fitting based on the Levenberg-Marquardt method was used in the reconstruction. All the candidate maxima of the interested region were found in the "Peak Fit" tool (Source code is available at: https://github.com/aherbert/GDSC-SMLM). The PSF of the microscope was approximated to a 2D Gaussian function using the PSF Calculator tool, and the initial parameters for the 2D Gaussian were set to the initial standard deviation value in pixels. The gain was calculated by the mean-variance test of different voltage supplied by the PMT detectors, and given as Analogue-to-Digital Units (ADUs) per photon in each image (see section 3.1.1). Calibration was set to the pixel size of the image. The images were scaled up to 10 times for producing a reconstructed image, where each localisation was weighted to an average size of each QD, which is about 10 nm. The maximum localisation precision of the single-QD positions were set (e.g. 5 or 6 nm) while the localisation images were being reconstructed. Thus, any localisation, which has a precision above this value, was discarded by the software. The quantification of the image resolution

was calculated from the FWHM of the cross-sectional line profile in the microtubule images. As for the DNA origami and neuron images, the average distances between the localisations in the reconstructed images were calculated for determining the image resolution that can be improved. The localisations in the reconstructed images of DNA origami were recoloured in Adobe Photoshop 7.0 based on the colours in the raw images. Finally, the drift of the system was calculated using 500 nm beads and found as negligible for sub-minute data acquisition time (see section 3.1.2).

Chapter 3

RESULTS AND DISCUSSION

3.1 Microscope system characterisation

In this study, we used the GDSC-SMLM ImageJ plugin, which was developed by Alex Herbert from the University of Sussex, for peak fitting. In order to use the "Peak Fit" tool of the plugin, it needs to be calibrated in terms of pixel size, gain and PSF approximation. The pixel size is given by the size of the scanned area divided by the scanning format, as explained in section 2.5.2. In this section, the gain and PSF calibration of the laser scanning confocal microscope will be described. In addition, the mechanical stability of a microscope is essential in single-molecule localisation techniques. Thus, the drift analysis of the microscope will be given in the following subsections.

3.1.1 Mean-variance test and gain analysis

The number of pixel values recorded per photon is known as “the gain”, and it is given in Analogue-to-Digital Units (ADUs)/photon. As we took 8-bit images, each pixel value ranges from 0 to 255. The gain is required to specify to the software for the conversion of the pixel values to photons and the volume of the fitted 2D Gaussian to the localisation signal. The number of photons is computed by dividing signal to the gain. The photon count is later used by the software using the formula of Mortensen et al. for localisation precision using the least squares fitting [119]:

$$Var_x = \frac{s_a^2}{N} \times \left(\frac{16}{9} + \frac{8\pi s_a^2 b^2}{Na^2} \right) \tag{3.1}$$

where Var_x is the variance of the localisation position in the X dimension, s_a is the standard deviation of the fitting function (Gaussian), a is the pixel size of the image (in nm), N is the total number of photons measured, b^2 is the expected number of photons per pixel (background noise).

Therefore, we calculated the gain for our microscope, the Leica SP2 Laser Scanning Microscope, before analysing the images in GDSC-SMLM. For this purpose, we first imaged a homogeneous layer of 30 nm fluorescent beads at different laser powers, 0, 0.1 mW, 0.2 mW, 0.4 mW, 0.6 mW, 0.8 mW and 1 mW, and at different voltage supply, 600 V, 650 V, 700 V, 750 V, 800 V and 850 V. As a bias image, the sample was also observed without any power and voltage supply. Each image was combined with the bias image in a stack, and the mean-variance test was performed by the plugin (GDSC-SMLM>Calibration). The software computed the mean and the variance of the difference of each image as seen in Table 3.1.

The data was later used to approximate the camera gain, and the graph of the variance of pixel values against the mean pixel values seen in Figure 3.1 was plotted by using a linear best fit line in Excel. The gradient of each line gives the gain of that particular voltage. These were also calculated and given in Figure 3.2. It is found that, as the voltage applied to the PMT increases, the gain increases exponentially. The blue dashed line shows a linear fit to the natural logarithm of the data. The value of the gain was calculated each time depending on the applied voltage according to the expression seen in Figure 3.2, and used in finding localisations.

3.1.2 Drift analysis

During the imaging processes, usually, there is a continuous movement of the sample, known as "drift", which might be caused by vibrations of the platform, slippage of the focus mechanism, thermal gradients or air flow in the sample. Drifting of the sample is always a problem, especially for the long term imaging; for instance,

Table 3.1: Data of mean-variance test results.

Voltage	Laser Power (mW)	Mean-1	Mean-2	Mean	Variance
600 V	0	10.48	10.46	10.47	0.38
	0.2	15.49	15.46	15.48	16.38
	0.4	28.58	28.59	28.59	58.52
	0.6	52.14	52.70	52.42	133.15
	0.8	89.99	92.30	91.15	245.61
	1	134.43	135.08	134.76	363.00
650 V	0	10.57	10.56	10.57	0.72
	0.2	20.81	20.74	20.78	59.27
	0.4	47.34	47.33	47.34	206.83
	0.6	95.64	96.70	96.17	457.67
700 V	0	10.64	10.62	10.63	1.63
	0.2	26.06	26.14	26.10	150.03
	0.4	66.76	66.85	66.81	516.16
750 V	0	10.77	10.78	10.78	4.02
	0.2	41.31	40.87	41.09	466.64
800 V	0	10.78	10.77	10.78	10.08
	0.1	10.88	10.93	10.91	12.21
	0.2	50.91	50.37	50.64	894.44
850 V	0	11.02	10.98	11.00	20.22
	0.1	11.03	11.06	11.05	23.91

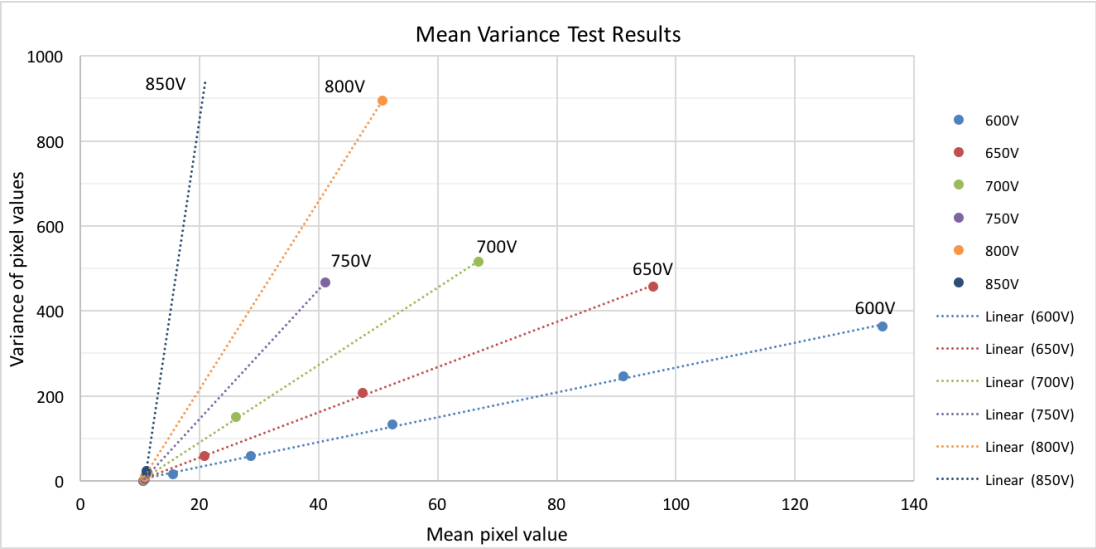

Figure 3.1: Graph of mean-variance test results for 600 V, 650 V, 700 V, 750 V, 800 V and 850 V, and best fit lines of each supply voltage.

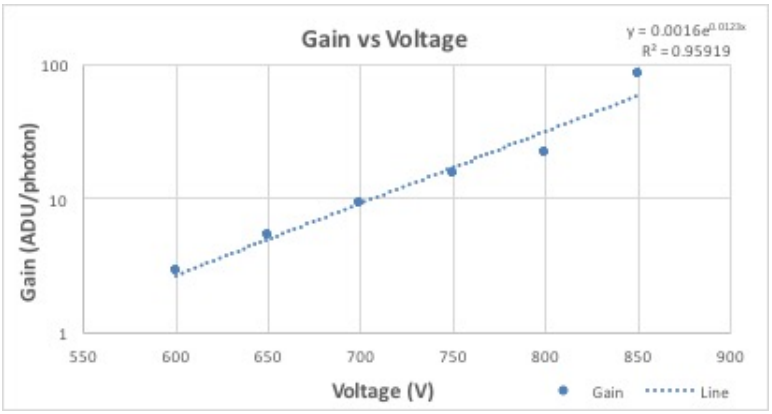

Voltage (V)	Gain (ADU/photon)
600	2.928
650	5.325
700	9.125
750	15.26
800	22.19
850	84.45

Figure 3.2: Graph and table of Gain (ADU/photon) vs Voltage (V) data at 600 V, 650 V, 700 V, 750 V, 800 V and 850 V.

several minutes or more. It can be either corrected or reduced by hardware solutions, such as a vibration isolation table to improve the stability of the instrument, and an environmental chamber that is enclosing the sample stage and the objective elements to keep the temperature stable, or by software solutions via correcting the position of the image with a reference point. In order to measure sample drift in our microscope system, the Leica TCS SP2 Inverted Laser Scanning Confocal Microscope, we took 20 images of 0.5 μm fluorescent latex beads, (Sigma, L5530, excitation wavelength: 520 nm, emission wavelength: 540 nm) for 95 seconds with 5 second intervals. The images were analysed by "Drift Analysis" of GDSC-SMLM (v3.1) in ImageJ (v1.48) and, Figure 3.3 shows the axial drifts of a 500 nm bead in terms of pixels, both for the X (blue) and Y (orange) axis. The pixel size of the images was 58 nm. In QDOSS, the data acquisition time takes from 320 microseconds to 40 seconds, which are relatively short periods compared to that in conventional single-molecule localisation based super-resolution microscopy techniques (i.e. the data acquisition time takes from several minutes to tens of minutes in STORM and PALM). Therefore, it is found that the drift is negligible (<0.0244 px $\approx$<1.5 nm) within 1 minute of imaging via QDOSS and ignored in our further localisation analysis. As for the comparison of QDOSS with STORM, we took into consideration the drift in the image analysis in section 3.3.2 using a software-based drift correction of Zeiss.

After determining the gain and the drift, we studied DNA imaging as reference

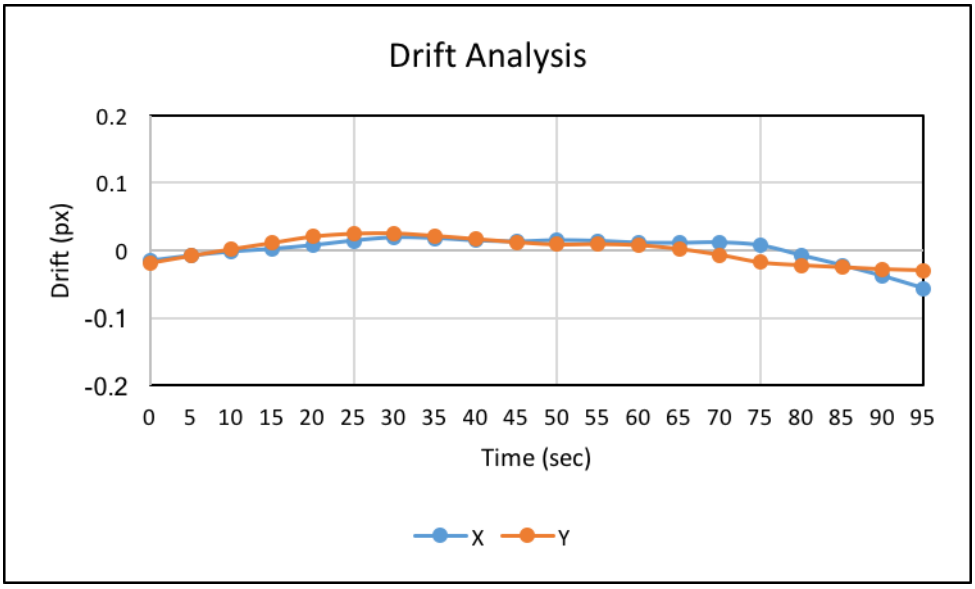

Figure 3.3: The plot of the calculated drift of the 0.5 μm fluorescent latex beads in X-axis (blue) and Y-axis (orange) for 95 seconds. The pixel size was 58 nm.

structures for testing the QDOSS, and the results are given in the next section.

3.2 DNA imaging

In this study, as described in section 2.1, we used the size-dependence of the emission due to quantum effects for the purpose of super-resolution. In order to test the idea, first, we used 180 bp long ssDNA as a reference with three different off-the-shelf QDs that are modified by complementary ssDNA to long ssDNA. Then, we targeted triangular DNA origami by two and three different QDs that are attached within sub-diffraction distance.

3.2.1 DNA ruler

Since it is easy to modify and target a long ssDNA with small oligonucleotides, we first used 180 bp long ssDNA as a template. The sequences of the nucleotides are given in Table 2.1. The longest ssDNA, TP53-CDNA, was used as a template sequence, and the other short ssDNAs, TP53-11, TP53-12, TP53-13, TP53-14 and TP53-6 were assembled on it. Before application of TP53-11, TP53-13 and TP53-6, they were mixed with NPBIOTIN-1 modified QD525, QD705 and QD585, respectively, in separate tubes

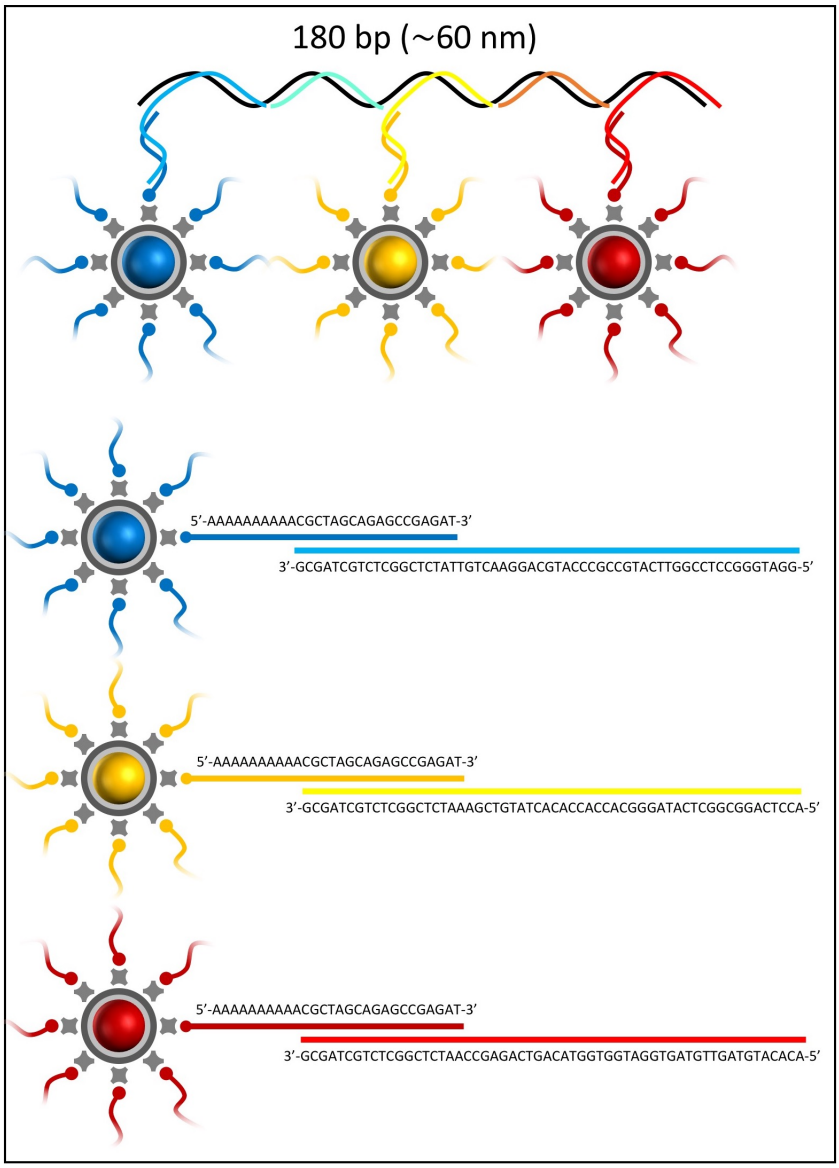

Figure 3.4: Schematic representation of the final structure of DNA ruler and QDs modified by oligonucleotides with their sequences.

to achieve the final structure of DNA ruler with QDs (Figure 3.4). By design, the distance between QDs was about 30 nm.

To be sure all ODNs were hybridised with each other, we first showed the construction steps of the DNA ruler after each ssDNA added to long ssDNA using electrophoresis, as seen in Figure 3.5. The DNA mixtures were loaded in a 2% agarose gel and run at 80 V for 15 minutes. A 50 bp ladder was used as a marker. The second well contained only QDs (QD525). That's why it is seen so brightly under UV light.

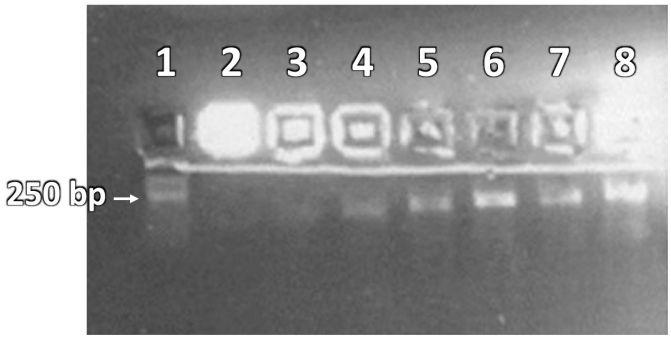

Figure 3.5: Photo of 2% Agarose gel loaded with ODNs for each step during construction of a DNA ruler.

Table 3.2: The samples loaded in the wells.

Lane	Sample
1	50 bp ladder
2	QD525
3	TP53-CDNA
4	TP53-CDNA + TP53-11
5	TP53-CDNA + TP53-11 + TP53-12
6	TP53-CDNA + TP53-11 + TP53-12 + TP53-13
7	TP53-CDNA + TP53-11 + TP53-12 + TP53-13 + TP53-14
8	TP53-CDNA + TP53-11 + TP53-12 + TP53-13 + TP53-14 + TP53-6

While the third well contained only the long DNA (TP53-CDNA), the fourth one was loaded with TP53-CDNA and TP53-11 mixture. The next one contained TP53-CDNA, TP53-11 and TP53-12. The others were loaded with the addition of the next ODN to the previous mixture. The eighth well has the DNA ruler. As seen in Figure 3.5, all bands are getting heavier each time, which means that all ODNs are hybridised with the previous mixtures. Additionally, not seeing any unhybridised ODN in the bands implies that all ODNs became part of the DNA ruler and no cross hybridisation occurred between ODNs. The QDs weren't loaded with the DNA ruler because it is not possible to see a band with QDs due to their high intensity of light emission under UV excitation.

The constructed QD-DNA ruler structure was observed under the laser scanning confocal microscope and the conditions of the microscope are given in Table 3.3.

The two spots seen in the bottom left of Figure 3.6a were then observed in different emission ranges (490-555 nm for QD525, 565-635 nm for QD585 and 640-800 nm for

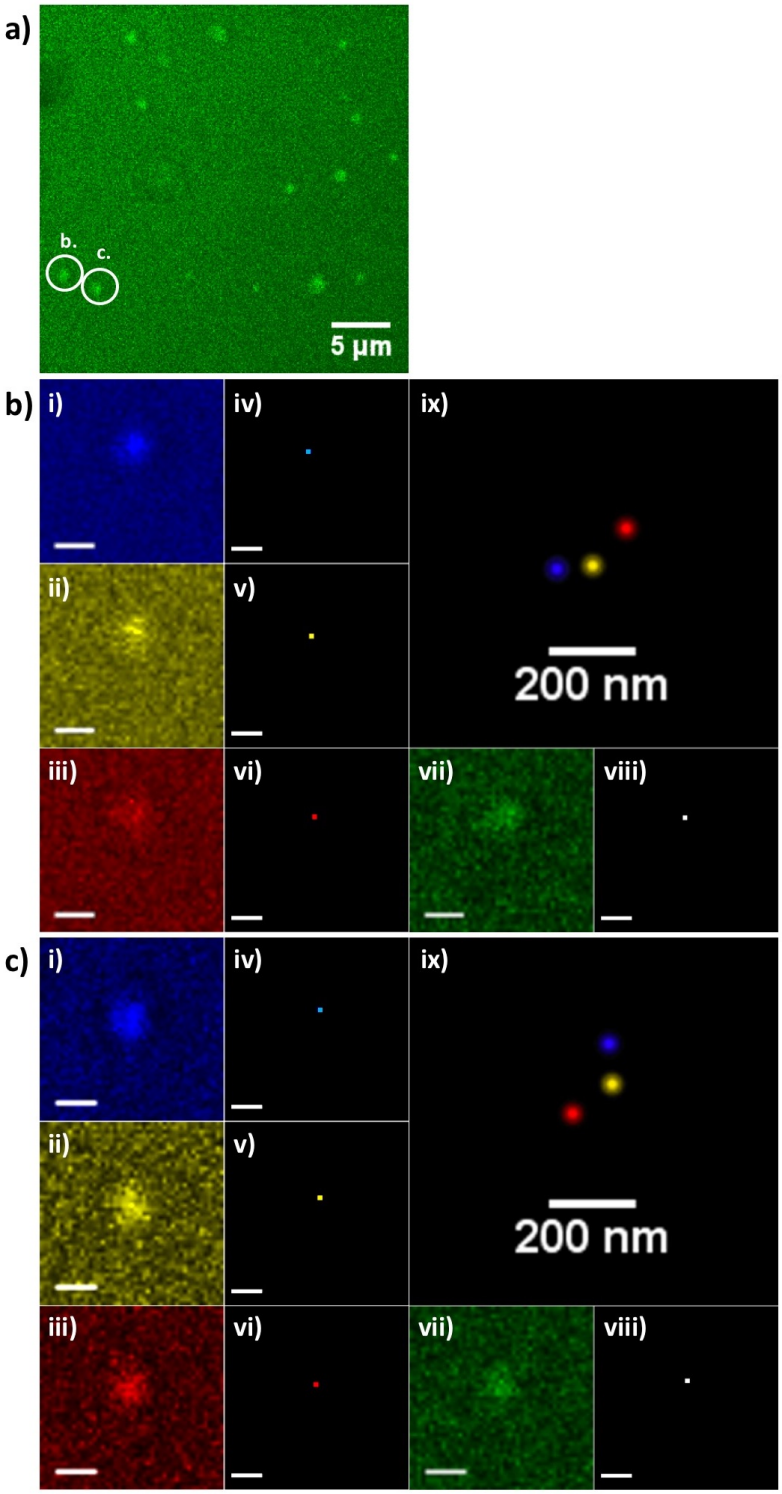

Figure 3.6: Super-resolution imaging of QDs attached to a DNA ruler. (a) General confocal image of QD-DNA ruler system. (b-c) QDOSS analysis of left (b) and right (c) spots: (i-iii) spectral separated and (iv-vi) localisations of each spot in different emission ranges, (vii-viii) the spot seen in all emission range and its localisation, and (ix) the reconstructed image via the overlay of each localisation seen in iv-vi. Scale bar is 200 nm.

Table 3.3: Microscopy settings for DNA ruler imaging.

Parameters			Settings	
# of QDs			3	
QD525	**Emission Ranges (nm)**	**Gain (V)**	490-555	635
QD585			565-635	730
QD705			640-800	716
ALL			490-800	734
Scan size (μm)			48.77	
Scan format (pixel)			512x512	
Pixel size (nm)			95	
Scan speed (Hz)			400	
Scanning direction			bidirectional	
Line:Frame Averaging			2:2	
Time per colour (sec)			2.56	
Laser intensity (Wcm^{-2})			0.102	
Bit depth			8	

QD705 as seen in Figure 3.6b-i,ii,iii and c-i,ii,iii for left and right spot respectively). After the centres of these spectrally separated spots were localised using an ImageJ fitting plugin, GDSC-SMLM (v3.1), the final constructed images were obtained, as seen in Figure 3.6b-ix and c-ix. The spots observed in all emission ranges (490-800 nm) are seen in Figure 3.6b-vii and b-vii, and their single localisations are seen in Figure 3.6b-ix and c-ix. Compared to nonspectrally separated images, three QDs can be localised and seen in the correct order (Figure 3.6b-ix and c-ix), although the distance between the first and the last QD is not consistent with the length of the DNA ruler. This may be because the localisation precision defined by the software is <30 nm. In addition, the DNA ruler is not a rigid structure. So it can easily be bent whilst drying. Therefore, we tried the same strategy by using DNA origami, which is more rigid structure compared to a DNA ruler, as described in the following section.

3.2.2 Triangular DNA origami

DNA origami is a well-defined and rigid structure compared to other DNA structures. We used triangular DNA origami with a side length of 120 nm (Figure 3.7). Three staple strands in the middle positions of the sides were modified and extended with unique sequences for programmed assembly of three different streptavidin conjugated QDs with a maximum emission at 525 nm, 605 nm and 655 nm. Each of these QDs was

functionalised with a different biotin modified single-stranded DNA, complementary to the sequences which extended from the sides of the aforementioned triangular DNA origami. Two or three different types of QDs were then attached to DNA origami. In this arrangement, the distance between the middle positions of the sides is approximately 60 nm, by design (Figure 3.7).

Atomic force microscopy (AFM) imaging was employed to verify the attachment of QDs to the DNA origami (Figure 3.8). As seen in the line analysis of triangular DNA origami with 3 QDs, while the height of double helix DNA is around 2 nm, the heights of QDs are between 5.5 nm to 7.5 nm. Therefore, we can conclude that different sizes of QDs were attached to DNA origami. It was also found that the distance between the QDs varies between 60 nm to 90 nm, due to the flexibility of the DNA strands anchoring the QDs to the Origami (Figure 3.8a and b).

These samples were then used to collect images using a conventional confocal microscope capable of spectroscopic signal separation (Leica TCS SP2). The laser scanning confocal microscopy settings of triangular DNA origami imaging are given in Table 3.4. Since we attached 2 or 3 different QDs to DNA origami, different emission ranges were set for the imaging of each type of QDs. Whereas the emission ranges were 570-630 nm for QD585, 650-800 nm for QD705 in the 2-QDs-bound system, we set the emission ranges to 490-560 nm for QD525, 570-620 nm for QD585 and 635-700 nm for QD655 in the 3-QDs-bound system. To image all QDs in the same channel, the emission ranges were set to 570-800 nm and 490-700 nm, respectively. The gain values were adjusted to "ADU/photon" while finding localisation, as explained in section 3.1.1. The pixel sizes were set to between 66 nm and 93 nm based on the scanning size and zoom factor. Depending on the scanning format and speed, the data acquisition times were taken between 3.84 to 5.12 seconds per each image.

Original frames were processed using an ImageJ fitting plugin, GDSC-SMLM, to obtain SR images (Figure 3.9a and b). The average distance between the localisations seen in the reconstructed images was found as 75 ± 15 nm (Figure 3.9a and b). Comparison of the AFM and the reconstructed SR images shows consistency in the patterns and distances of QDs attached to DNA origami, thus confirming optical

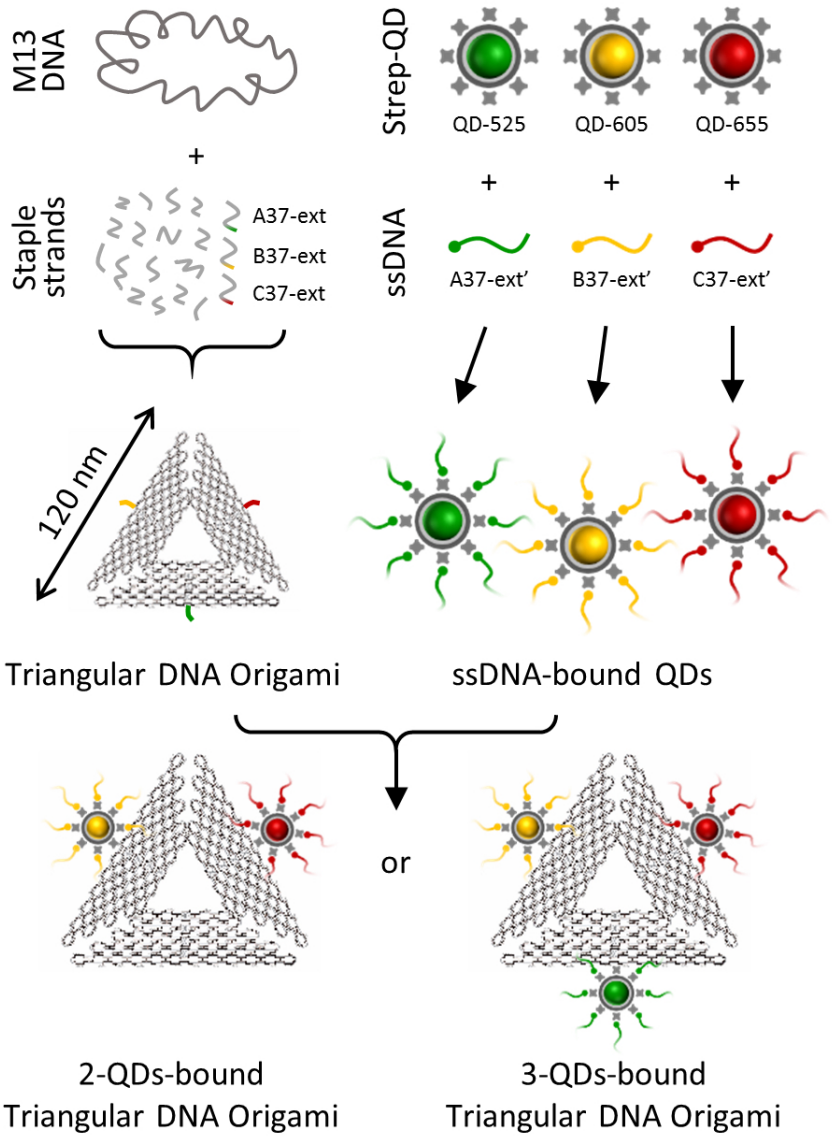

Figure 3.7: Schematic illustration of the preparation of 2-QDs and 3-QDs-bound triangle DNA origami systems. The staple strands on each side have extension sequences complementary to the ssDNA bound to QDs. While QD605 and QD655 were attached on two different sides of the DNA origami in the 2-QDs-bound system, QD525 were included to attach on the third side in the 3-QDs-bound system.

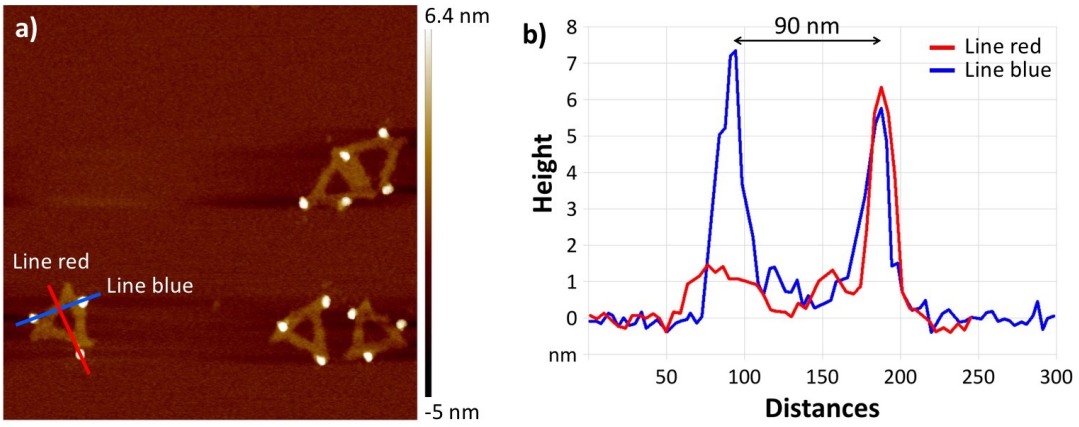

Figure 3.8: (a) AFM image of 3-QDs-bound DNA origami and (b) cross line profiles of left-bottom DNA origami seen in (a).

Table 3.4: Microscopy settings for triangular DNA origami imaging.

Parameters				**Settings**					
# of QDs				2		3		3	
QD525	**Emission Ranges (nm)**		**Gain (V)**	-	-	490-560	762	490-560	770
QD605				570-630	684	570-620	800	570-620	816
QD655				-	-	635-700	797	635-700	797
QD705				650-800	693	-	-	-	-
ALL				570-800	656	490-700	775	490-700	715
Scan size (μm)				47.61		18.37		67.49	
Scan format (pixel)				512x512		256x256		1024x1024	
Pixel size (nm)				93		72		66	
Scan speed (Hz)				400		400		400	
Scanning direction				bidirectional		bidirectional		bidirectional	
Line:Frame Averaging				2:3		4:4		2:2	
Time per colour (sec)				3.84		5.12		5.12	
Laser intensity (Wcm^{-2})				0.018		0.363		0.099	
Bit depth				8		8		8	

resolution down to at least 60 nm (with localisation precision of 6 nm), i.e. well below the diffraction limit.

3.3 Alpha-tubulin imaging

Following DNA origami tests, we imaged alpha-tubulin structures in HEK293T cells. Since microtubules are continuous biological structures in the cytoplasm and their outer diameter is about 24 nm, which is below the diffraction limit, they are widely

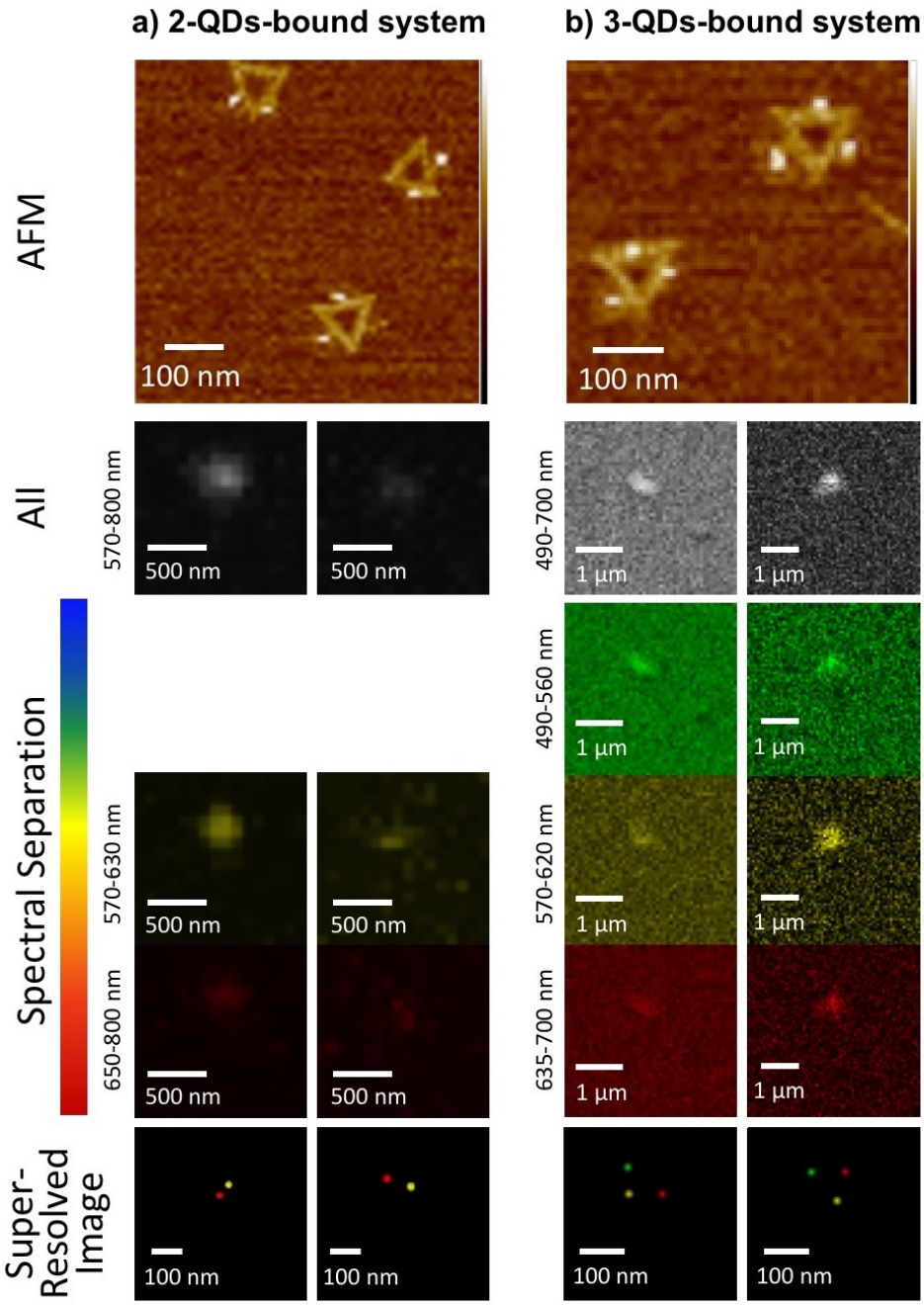

Figure 3.9: AFM, confocal microscope, and reconstructed images of (a) 2-QDs and (b) 3-QDs-bound systems. To give an illustration, two spots were spectrally separated, and localisation images were reconstructed for each system. Sums of all images (grey) represent the confocal images of the spots without spectral separation (the emission wavelength ranges from 570 nm – 800 nm in a and 490 nm – 700 nm in (b). Spectrally separated images and the localisations in the reconstructed images were recoloured as green for QD525, yellow for QD605 and red for QD655 and QD705.

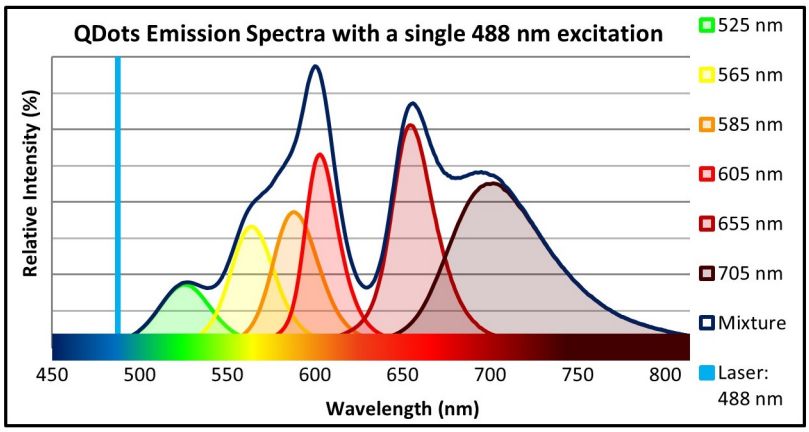

Figure 3.10: Emission spectra of six types of Qdots® and their mixture with a single 488 nm excitation.

used as a biological structure to stain for illustrating different super-resolution imaging techniques. We stained the microtubules with six different types of QDs (525 nm, 565 nm, 585 nm, 605 nm, 655 nm and 705 nm), which were mixed before application. Figure 3.10 shows the emission profiles of the individual and mixture of QDs excited with a single wavelength at 488 nm.

3.3.1 Immunostaining of alpha-tubulin structure in HEK293T cells

The labelling protocol was developed from the manufacturer's recommendations (Invitrogen, Qdot® Streptavidin Conjugates) [116]. Instead of labelling a structure with only one type of fluorophores, the mixture of six types of QDs were used in the labelling procedure. Firstly, HEK293T cells (5x10^4 cell/mL) were seeded on poly-L-lysine-coated coverslips (0.13 to 0.17 mm thick) in a 12-well plate for overnight growth. Before staining, cells were washed with a 1X PBS buffer and then fixed with 4% paraformaldehyde (Thermo Scientific) in PBS for 15 minutes and permeabilised with 0.25% v/v Triton X-100 (Sigma Aldrich) in PBS for 15 minutes. After washing with 1X PBS, cells were left in an endogenous biotin blocking buffer for 1 hour. Then, anti-alpha-tubulin monoclonal antibody (Thermo Fisher Scientific) was diluted to 1 μg/ml in the blocking buffer and added to cells for 1 hour. Staining was followed with the addition of six colour QDs streptavidin conjugates (Invitrogen) with emission peaks at 525, 565, 585, 605, 655 and 705 nm, and each colour of QDs was diluted to 15

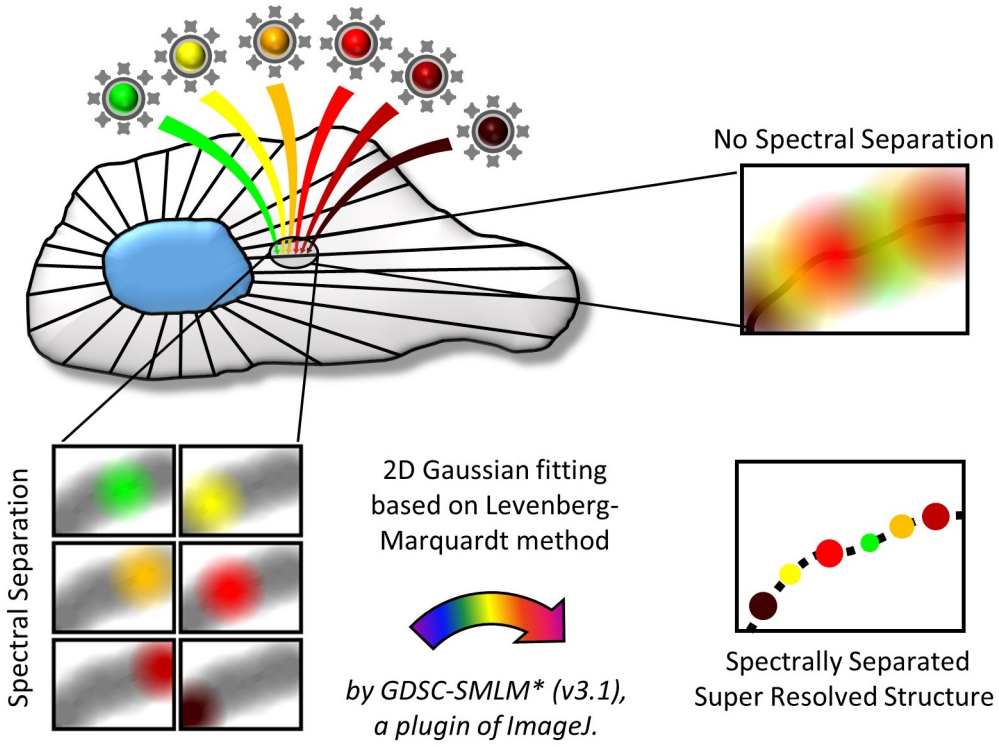

Figure 3.11: Schematic representation of QDOSS labelling and imaging of microtubules.

nM in the blocking buffer. Finally, cells were washed with ethanol and toluene and mounted with Cytoseal 60 (Thermo Fisher Scientific) before imaging them under a microscope. Figure 3.11 shows the labelling and the QDOSS imaging procedure of microtubules.

In order to compare QDOSS with current super-resolution techniques, we will first give the results of the STORM imaging, which uses the blinking properties of QDs. Then, we will show QDOSS microscopy images of the same sample in different conditions, such as in high image formats, fast imaging, with spectral slicing and 3D imaging.

3.3.2 STORM imaging

Stochastic Optical Reconstruction Microscopy (STORM) has been used for super-resolution imaging since 2006 [62]. Although it was originally described using fluorescent dyes, any photoswitchable fluorophore, such as organic dyes or QDs, can be

used for the reconstruction of a super-resolved image based on temporal separation of stochastically activated fluorophores. Unlike dyes, the QDs are separated by their blinking statistics. They were first shown in use in super-resolution imaging in 2005 by Keith A. Lidke and his colleagues [120], and there have been several papers published since then by other groups [121, 122]. In this part of the study, we observed microtubules of HEK293T cells using a 100X 1.46 NA oil objective under the super-resolution imaging microscopy of Zeiss, LSM 710 ELYRA PS.1 in TIRF mode. The QDs were excited by HR Diode 488 nm (100 mW) Laser and 10,000 images were taken with an exposure time of 45 ms (>7.5 minutes in total). The images were captured by the electron multiplying CCD and saved in 512x512 pixels image format. The images sizes were 42.65 μm and the laser intensity on the sample was 1.3 kW/cm^2.

Figure 3.12a shows the confocal image of microtubules. 10,000 raw confocal images were analysed with the software Zen 2010D (Carl Zeiss Microscopy, Jena, Germany) and the reconstructed image is shown in Figure 3.12b. As the normalised line profiles of orange (for the confocal image) and blue (for the STORM image) were measured, the FWHM of the lines was found to be 280 nm and 78 nm in the standard confocal image and the STORM image, respectively. This shows that the resolution was improved from 280 nm to 78 nm by STORM. One should remember that it was previously improved down to $\approx$51 nm via STORM with an image acquisition time of <30 minutes [83]. Although line profiles of microtubules should have two peaks because of the lumen of the microtubule ($\sim$12 nm), as were seen in the previous studies using organic dyes (Figure 1.25), we found only one peak in Figure 3.12c. This might be caused by the large sizes of QDs (8-12 nm), which prevented us being able to observe the cross-section of the microtubule in detail. In addition, even though the discontinuities and the heterogeneities seen in Figure 3.12b show insufficient labelling density, the improvement in the resolution can still be measured from the line analysis. Hence, we used the same sample for QDOSS data acquisition in various conditions: high imaging format, fast imaging, spectral slicing imaging and 3D imaging.

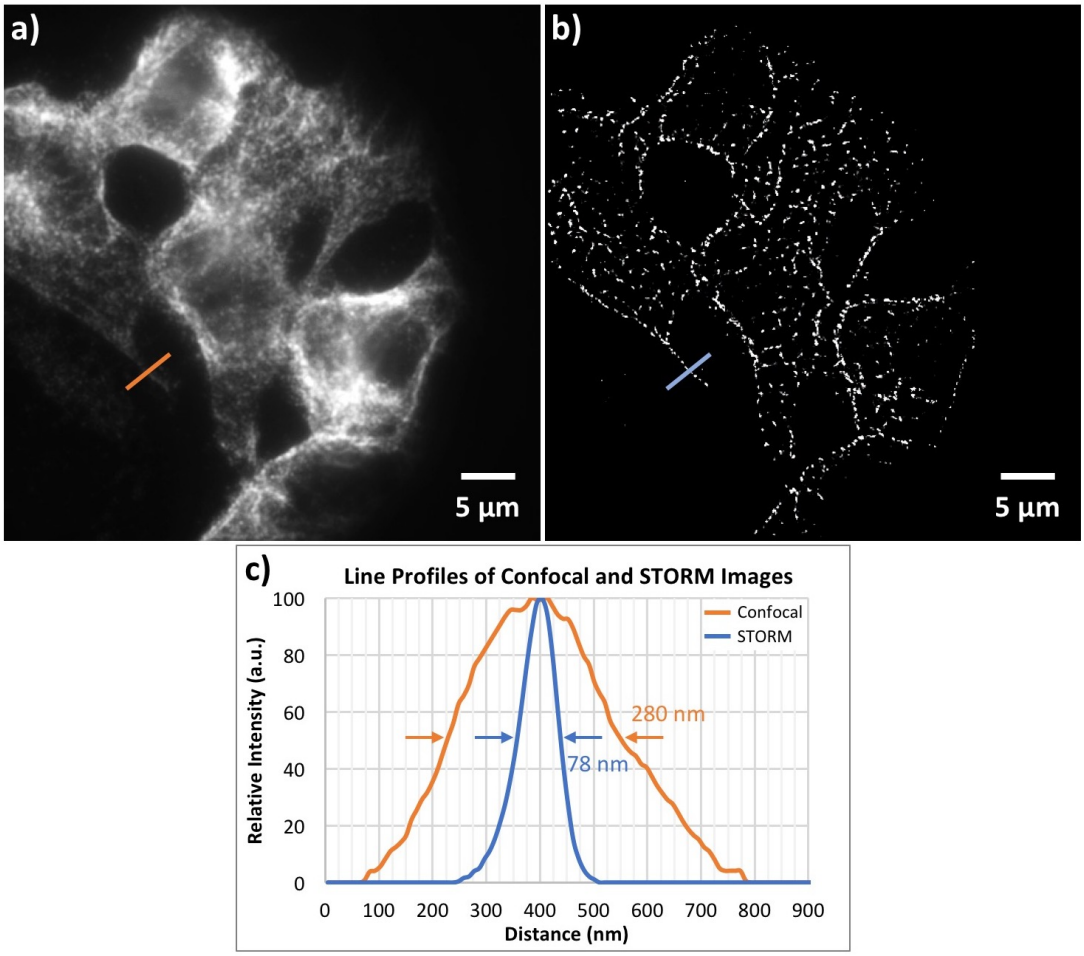

Figure 3.12: STORM imaging and line profile analysis. (a) Confocal and (b) STORM images of QDs, and (c) line profiles of microtubules seen in confocal (orange line) and STORM (blue line) images.

3.3.3 High imaging format

Following acquisition and analysis of STORM images, we carried out QDOSS imaging in the high imaging format. The images were taken in 4096x4096 pixels and small pixel size (15 nm) (Table 3.5) to get a highly resolved image, though the pixel size should be set to about half of the minimum spacing in order to resolve, according to the Nyquist sampling theorem. Each image was taken by rescanning and averaging of lines and frames twice to reduce the noise, with a data acquisition time of 40.96 seconds per frame (i.e. each colour channel) (see Table 2.2). The emission ranges were selected as 500-560 nm, 540-580 nm, 570-605 nm, 590-630 nm, 630-675 nm and 675-755 nm, respectively. For comparison, all QDs were also observed in a single image that

Table 3.5: Microscopy settings for imaging of microtubules in high imaging format.

Parameters			**Settings**	
# of QDs			6	
QD525	**Emission Ranges (nm)**	**Gain (V)**	500-560	861
QD565			540-580	874
QD585			570-605	776
QD605			590-635	793
QD655			630-675	814
QD705			675-755	888
ALL			500-809	834
Scan size (μm)			59.52	
Scan format (pixel)			4096x4096	
Pixel size (nm)			15	
Scan speed (Hz)			400	
Scanning direction			Unidirectional	
Line:Frame Averaging			2:2	
Time per colour (sec)			40.96	
Laser intensity (Wcm^{-2})			0.084	
Bit depth			8	

covered the emissions from 500 nm to 809 nm.

Following acquisition of the total emission signal (between 500 nm and 809 nm, Figure 3.13a) and for each type of QDs in different channels (Figure 3.13d), the region of interest (white square in Figure 3.13a) for each frame was reconstructed (Figure 3.13c, f) according to a 2D Gaussian fitting based on the Levenberg-Marquardt method. While Figure 3.13c shows the reconstruction image of Figure 3.13b that includes all QDs, Figure 3.13e shows each reconstructed image of each QD type shown in Figure 3.13d, and the reconstructed (using all frames in Figure 3.13e) SR image is shown in Figure 3.13f. One can see in Figure 3.13c and e that the QDs couldn't be localised better than the diffraction limit (250 nm), as expected. However, as seen in the cross-sectional line profile analysis of Figure 3.14a and b, the resolution has been improved from 298 nm to around 46 nm (Figure 3.14c) by image reconstruction of six frames with a localisation precision of <6 nm (Figure 3.13e). What is more, compared to STORM image of the same sample, it was found that better spatial resolution at faster acquisition time has been achieved in QDOSS imaging. As scanning in the high imaging format (i.e. 4096x4096 pixel) and taking the line and frame averaging twice

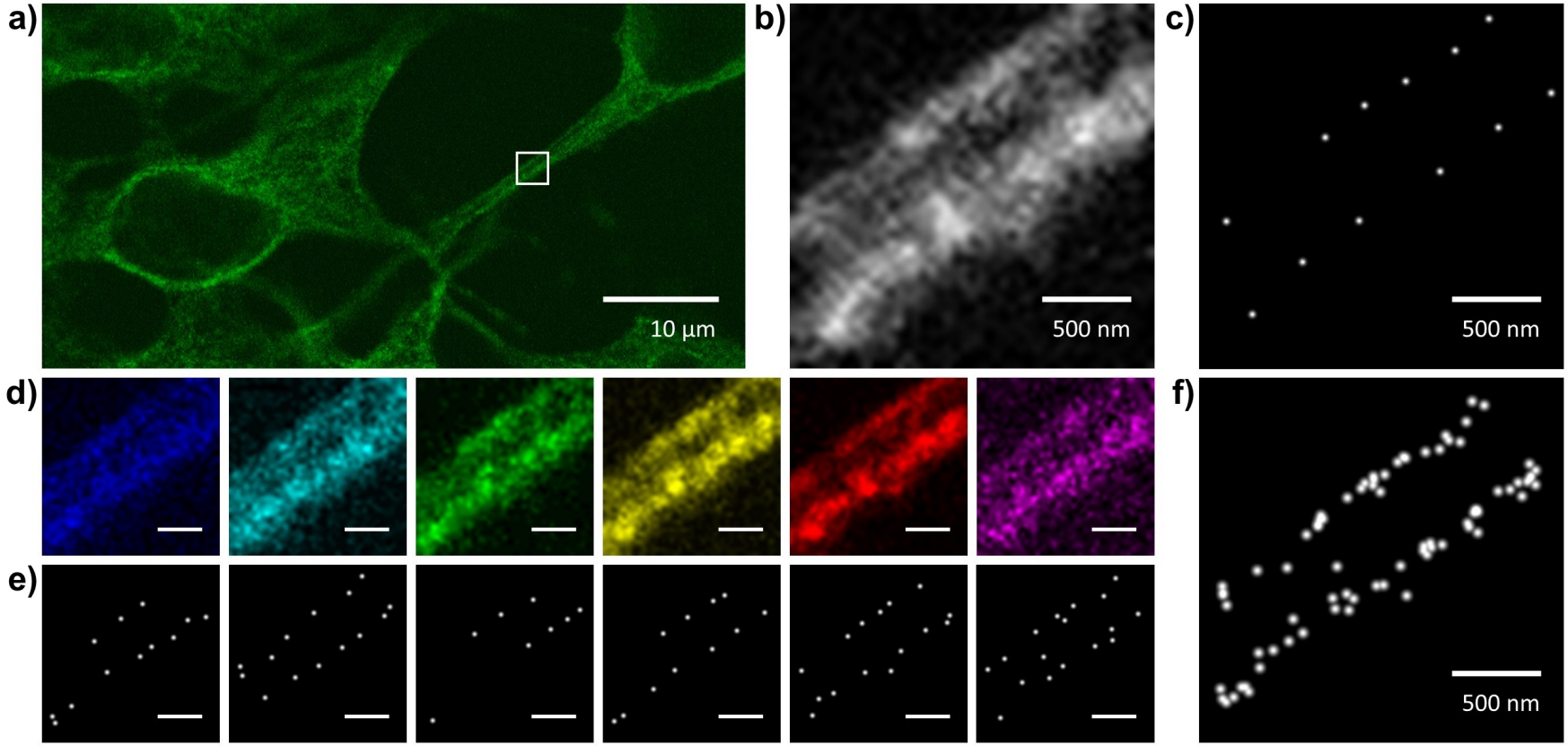

Figure 3.13: Super-resolution imaging of alpha-tubulin structure in HEK293T cells. (a) Confocal image of alpha-tubules labelled with six types of QDs. The original 4096x4096 pixel image was cropped from the top to fit it into the figure. (b) The region of interest (ROI) seen in white square in a that covers emissions between 500 nm and 809 nm (grey) (c) 2D Gaussian fitting analysis of b shows localisations of the non-spectral separated image. (d) Spectrally separated images of the ROI. The emission ranges are 500-560 nm for QD525 (blue), 540-580 nm for QD565 (cyan), 570-605 nm for QD585 (green), 590-630 nm for QD605 (yellow), 630-675 nm for QD655 (red) and 675-755 nm for QD705 (purple). (e) Localisations of each image seen in d. (f) Super-resolved reconstructed image by overlapping six images in e. Scale bar is 500 nm in d and e.

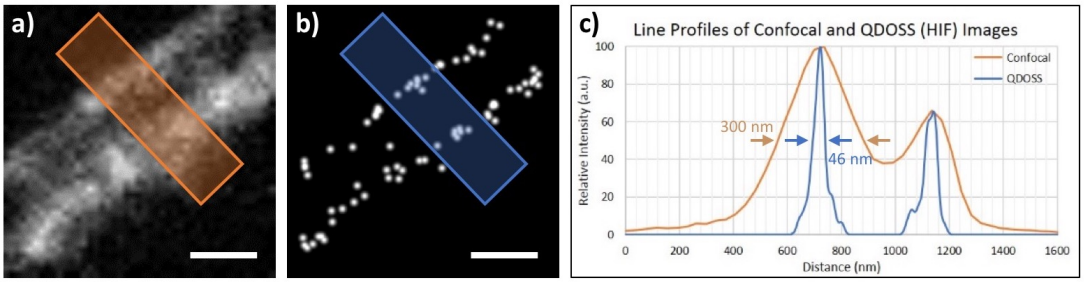

Figure 3.14: Line profile analysis of confocal and QDOSS in high imaging format. (a) Confocal image and (b) QDOSS reconstructed SR image of white square seen in Figure 3.13, and (c) line profiles of microtubules seen in confocal (orange line) and QDOSS (blue line) images. Scale bar is 500 nm.

lead to acquisition times in minutes, we decreased the imaging format to 256x256 pixel without rescanning in the next QDOSS imaging.

3.3.4 Fast QDOSS imaging

In this section, we tested the minimum time resolution that can potentially be delivered by the QDOSS approach. The microscopy conditions are given in Table 3.6. In order to decrease the data acquisition time, we took 256x256 pixel images of a selected area without taking line and frame averaging. This enabled us to decrease the acquisition time down to 320 milliseconds per colour channel using a bidirectional scanning rate of 400 Hz in a 256x256 pixel scan format (40 nm pixel size with 320ms/256/256 $\approx$5 μs per pixel) without line and frame averaging (1:1) (Table 2.2). The region of interest was sequentially observed in different channels with the same strategy as described in the previous subsection.

It is clear from the images (Figure 3.15b and d) that the contrast in the image decreases as the scan time is reduced. Following data acquisition, a selected area (white rectangle in Figure 3.15a) was analysed, and reconstructed images (Figure 3.15c, e and f) were obtained from the total emission (Figure 3.15b) and from six spectral channels (Figure 3.15d).

Line profile analysis of the reconstructed images shows that resolution can be improved down to around 41 nm (<6 nm localisation precision) when separate spectral channels are used, while it was remaining within the diffraction limit in confocal

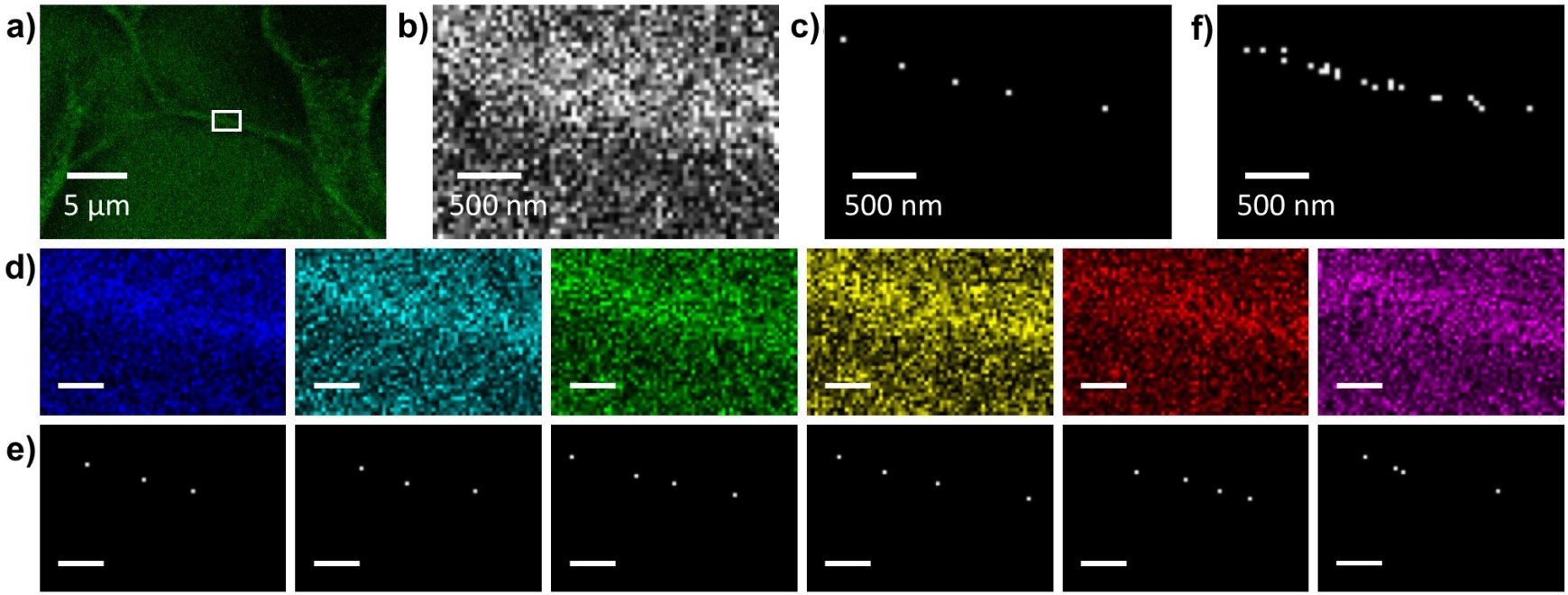

Figure 3.15: Fast super-resolution imaging of alpha-tubulin structure in HEK293T cells. (a) Confocal image of microtubules. (b) The region of interest (ROI) seen in white rectangle that covers emissions between 500 nm and 800 nm (grey) (c) Localisation image of b. (d) Spectrally separated images of the ROI. The emission ranges are 500-535 nm for QD525 (blue), 555-580 nm for QD565 (cyan), 580-595 nm for QD585 (green), 595-620 nm for QD605 (yellow), 640-665 nm for QD655 (red) and 675-800 nm for QD705 (purple). (e) 2D Gaussian fitting analysis of image seen in d. (f) Super-resolved image was reconstructed by overlapping six images in e. Scale bar is 500 nm in d and e.

Table 3.6: Microscopy settings for fast QDOSS imaging of microtubules.

Parameters			Settings	
# of QDs			6	
QD525	Emission Ranges (nm)	Gain (V)	500-535	694
QD565			555-580	746
QD585			580-595	750
QD605			595-620	773
QD655			640-665	749
QD705			675-800	727
ALL			500-800	762
Scan size (μm)			10.17	
Scan format (pixel)			256x256	
Pixel size (nm)			40	
Scan speed (Hz)			400	
Scanning direction			Bidirectional	
Line:Frame Averaging			1:1	
Time per colour (sec)			0.32	
Laser intensity (Wcm^{-2})			0.4914	
Bit depth			8	

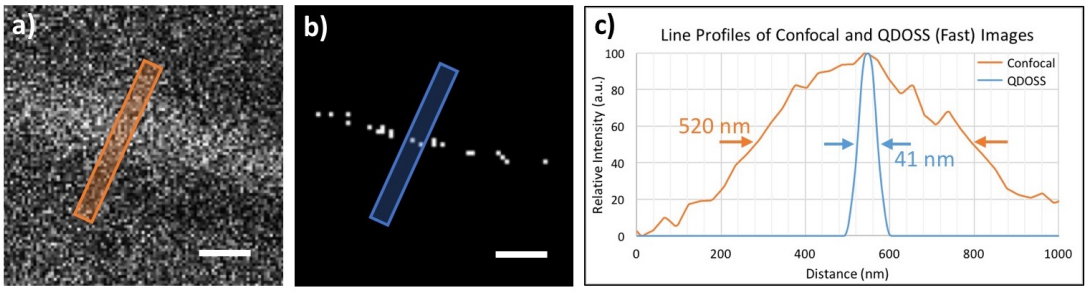

Figure 3.16: Line profile analysis of confocal and QDOSS in fast imaging format. (a) Confocal image and (b) QDOSS reconstructed SR image of white square seen in Figure 3.15a, and (c) line profiles of microtubules seen in confocal (orange line) and QDOSS (blue line) images. Scale bar is 500 nm.

image (Figure 3.16). This result confirms that the improved spatial resolution can still be achieved with QDOSS even if the time resolution of a channel is decreased to 320 milliseconds.

3.3.5 Spectral slicing

After showing fast super-resolution imaging by QDOSS, we tried to observe the same sample in 30 frames within 10 nm emission ranges from 490 nm to 790 nm. So far, we have observed the samples in the number channels that is the same as the number

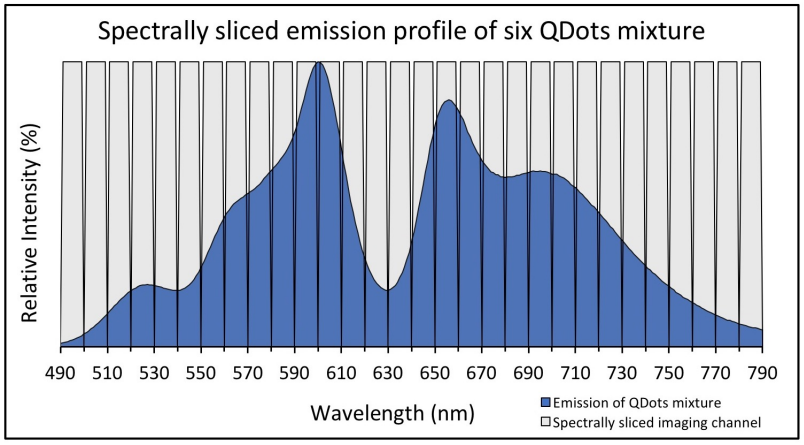

Figure 3.17: The emission spectrum of quantum dot mixture that consists of QD525, QD565, QD585, QD605, QD655 and QD705, and 30 emission ranges with 10 nm intervals that were used while observing microtubules (spectral slicing).

of types of QDs. In the previous studies done by Mingying Song, we argued that the broad emission spectrum of a mixture of QDs consists of the emission spectra of individual QDs in different sizes, and its spectrally sliced imaging can be used for finding the localisation of individual QDs [114, 115]. In other words, the emission profiles of QDs depends on the particle sizes because of the quantum confinement effects, and due to the fact that not all particles are identical in size in the mixture and so they emit at slightly different wavelength, the emission spectrum of the mixture of the QDs indicates the mixture of emission profiles of each different sized QDs. Therefore, we decided to increase the number of channels by spectral slicing to capture more QDs with distinctive emission wavelengths. 10 nm slicing interval was selected as it is close to the natural broadening of a single CdSe QD at room temperature [114, 123]. The emission profile of the mixture of the QDs in 30 emission slices is seen in Figure 3.17 and the microscopy settings can be found in Table 3.7.

The problem may come into account here that the same type of QDs can be observed in different channels so that we might localise it as separate labels. And if this had happened, we would have found the resolution improved compared to the previous microtubule results (i.e. less than 41 nm). In Figure 3.18a, we can see the general view of HEK293T cells within the emission range of 490 nm and 790 nm at the top left of the image, and 21 frames of each 10 nm interval from 500 nm to

Table 3.7: Microscopy settings for spectrally sliced imaging of microtubules.

Parameters	Settings
# of QDs	6
Emission Range (nm)	490-790
# of frames	30
Interval (nm)	10
Gain (V)	814
Scan size (μm)	47.61
Scan format (pixel)	512x512
Pixel size (nm)	93
Scan speed (Hz)	400
Scanning direction	Bidirectional
Line:Frame Averaging	4:2
Time per colour (sec)	3.84
Laser intensity (Wcm^{-2})	0.175
Bit depth	8

710 nm on the right. We didn't include the other frames after 710 nm because of the lower intensities of emissions. However, we took them into account whilst finding the localisations. The reason why the intensities are seen less in around 490-550 nm and 690-790 nm than in between 550 nm and 690 nm is that the relative intensities of QD conjugates are different under the same type of excitation. QD525 and QD705 have relatively lower light intensities than others when all of them are excited by 488 nm Ar laser. In addition, the 10 nm emission range also results in reduction of signal to noise ratio.

The region of interest seen in the white rectangle in the general view of the cells (Figure 3.18a) was analysed with GDSC-SMLM, and the spectrally non-separated image is seen in Figure 3.18c, while overlay of the localisations of the 30 spectrally sliced images is seen in Figure 3.18d. Whereas the resolution was found to be around 250 nm in the single image, which consists of all emission wavelengths, it can be improved down to 40 nm, where the precision of localisation is less than 5 nm, as seen in the line profile analysis of the reconstructed image of the microtubule structures (Figure 3.19).

This result indicates that the resolution is not related to the number of frames that are analysed by the software. Even if the same type of QDs were observed in different channels, the software finds the same localisations for them so that we couldn't achieve

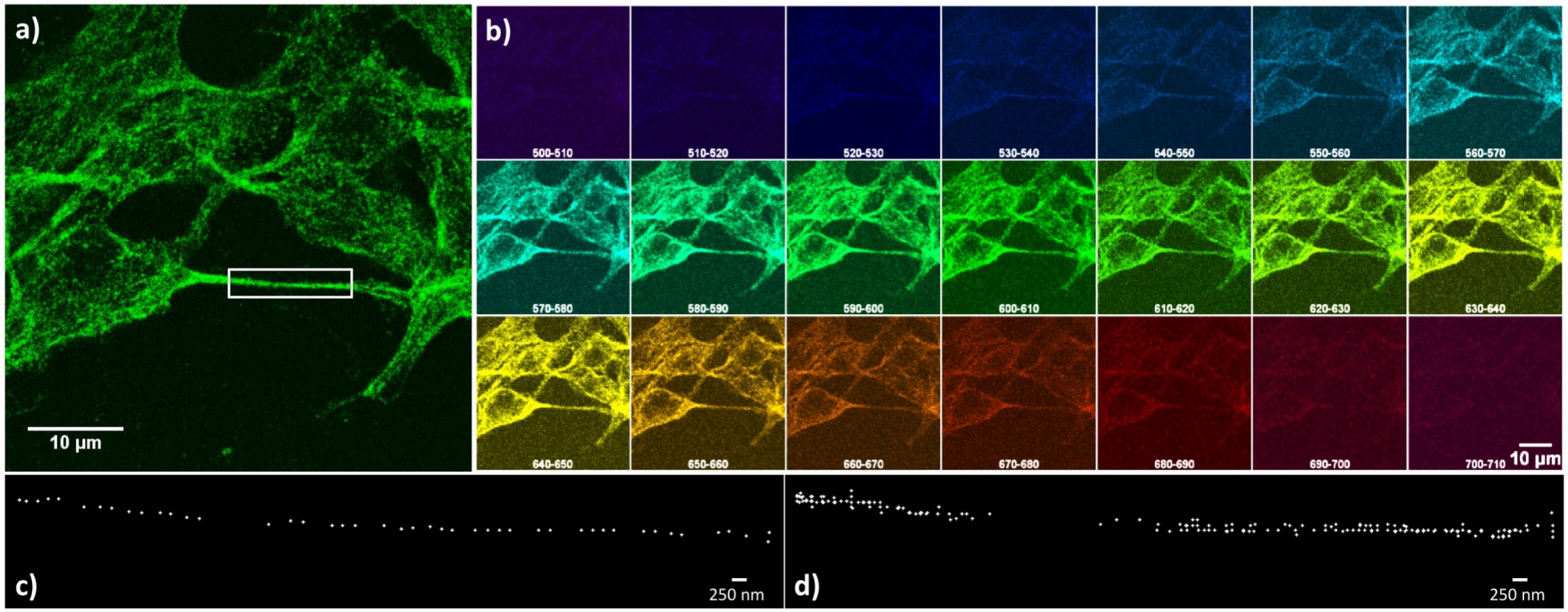

Figure 3.18: Spectral slicing imaging of alpha-tubulin structure in HEK293T cells. (a) Confocal image of microtubules observed in emissions between 490 nm and 790 nm. (b) 21 frames of spectrally sliced images observed between 500 nm and 710 nm with 10 nm intervals. (c) Localisation image of the region of interest (ROI) seen in the white rectangle in (a). (d) The reconstructed super-resolved image of the 30 frames that were observed within 10 nm emission ranges in the same area as seen in (c). Scale bar is 250 nm in c and d.

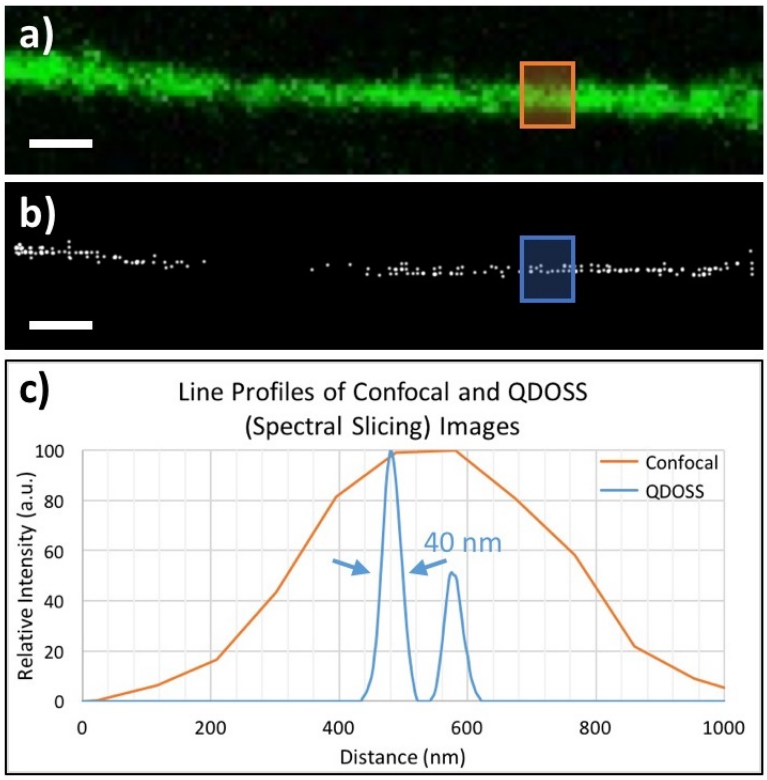

Figure 3.19: Line profile analysis of confocal and QDOSS in lambda scan imaging. (a) Confocal image and (b) QDOSS reconstructed SR image of white square seen in Figure 3.18a, and (c) line profiles of microtubules seen in confocal (orange line) and QDOSS (blue line) images. Scale bar is 1 μm.

a higher resolution in spectrally sliced imaging than in observing them in 6 channels (i.e. the same number of types of QDs used for labelling). On the contrary, it can also be concluded that the resolution couldn't be improved less than 40 nm when 6 types of QDs are used. This might be caused by random labelling of QDs mixture, which sets the stage for the possibility of QDs with a similar peak emission wavelength being closer than the diffraction limit, that would result in a compromised resolution.

Table 3.8 provides a summary comparison of the acquisition time, spatial resolution and localisation precision achieved in QDOSS and STORM for microtubules together them with the number of frames captured. It can be deduced from the Table 3.8 that significantly better resolutions and localisation precision has been achieved in all QDOSS conditions. Furthermore, the total data acquisition time could be decreased down to 1.92 seconds in QDOSS, whereas it was 7.5 minutes in STORM. Potentially,

Table 3.8: Comparison of spatial and time resolutions achieved and laser intensities on the sample used between STORM and various QDOSS imaging conditions in this study and the study of Wegel et. al. [124].

Parameters	STORM	High Imaging Format	Fast Imaging	Spectral Slicing	Wegel et. al. 2016 STED	STORM
Resolution (nm)	78	46	41	40	58.8	56.3
Precision (nm)	25	6	6	5	-	10
Time per frame	45 ms	40.96 sec	320 ms	3.84 sec	1.28 sec	20 ms
Number of frames	10,000	6	6	30	1	15,000
Laser Intensity	1.3 $kWcm^{-2}$	0.084 Wcm^{-2}	0.4914 Wcm^{-2}	0.175 Wcm^{-2}	150 $MWcm^{-2}$	2 $kWcm^{-2}$
Total time for image acquisition	7.5 min	$\sim$4 min	1.92 sec	$\sim$7.7 min	1.28 sec	5 min

further reduction in acquisition time is possible in QDOSS since we used a single PMT detector, which sequentially scanned different emission ranges. It is obvious that if the six channels can be observed at once, the time resolution of QDOSS will be the minimum acquisition time per channel (i.e. 320 milliseconds).

In order to check how well QDOSS works for 3D reconstruction and to utilise 3D capabilities of the confocal microscope, we carried out 3D tests of the same sample and the results will be given in the next subsection.

3.3.6 3D imaging

Before using QDOSS in multicolour imaging, we applied it for 3D imaging of microtubules. For this purpose, we took images of microtubules in 49 sections along z-direction, and captured the frames in the emission wavelengths between 490 nm and 800 nm for imaging of "all" types of QDs (Figure 3.20a), 490-540 nm for QD525, 540-575 nm for QD565, 575-595 nm for QD585, 595-625 nm for QD605, 625-675 nm for QD655 and finally, 675-800 nm for QD705 (Figure 3.20b). While the distance between two sections (step size) was 115 nm, the pixel size was set to 91 nm. The images were scanned in a 256x256 pixel scanning format with line:frame averages of 2:4. The whole scanned volume was 23.31x23.31x5.52 μm (x,y,z) and 343 frames (49 sections, 7 channels) were taken in total for the 3D construction (Table 3.9).

49 images that contain all of the wavelengths of the QDs in 49 z-steps are seen in Figure 3.21a. Since we scanned the sample from bottom to top, different parts of the cell were seen to be illuminated, depending on the z-position. Later, the images were combined in a stack and the 3D image seen in Figure 3.21b was constructed using the ImageJ 3D Viewer. As the white rectangle region is zoomed in on, it is clearly seen that the microtubule elongation started from bottom left to top right in the front-side image, where the image scale is 1 μm (Figure 3.21c). As far as the localisations of the QDs in the spectrally separated images are concerned, they were found in each of the 294 frames (49 sections, 6 channels) by using GDSC-SMLM, and the 3D image of the localisations were reconstructed in the 3D Viewer. The side view of the localisations is seen in Figure 3.21d. Although the elongation of the

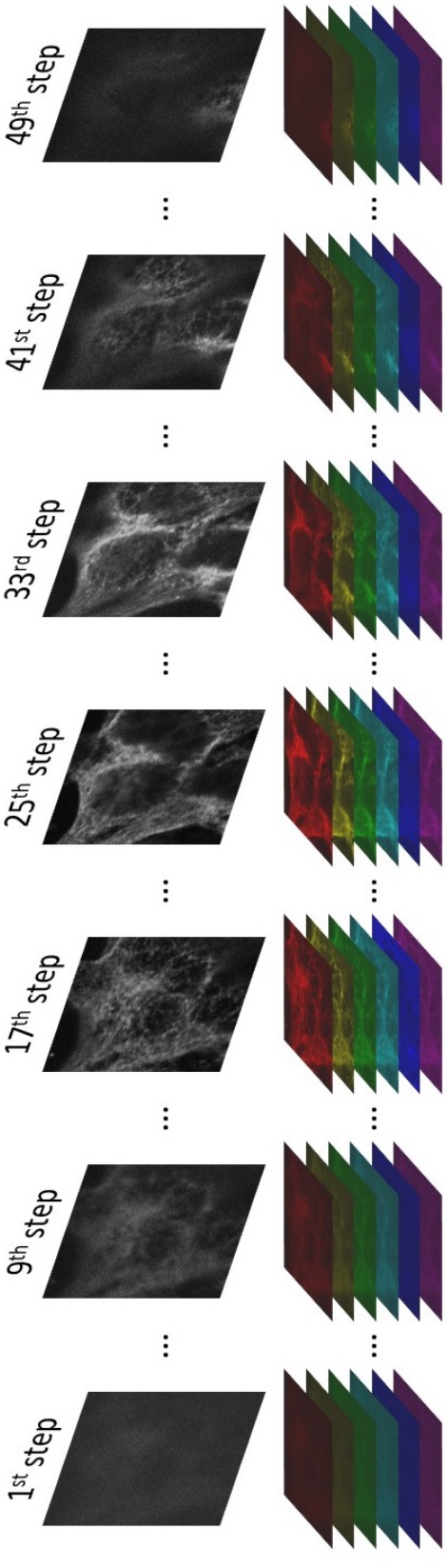

Figure 3.20: Confocal images of microtubules for 3D imaging. (a) 7 of 49 "all" images (b) and their "spectrally separated" images.

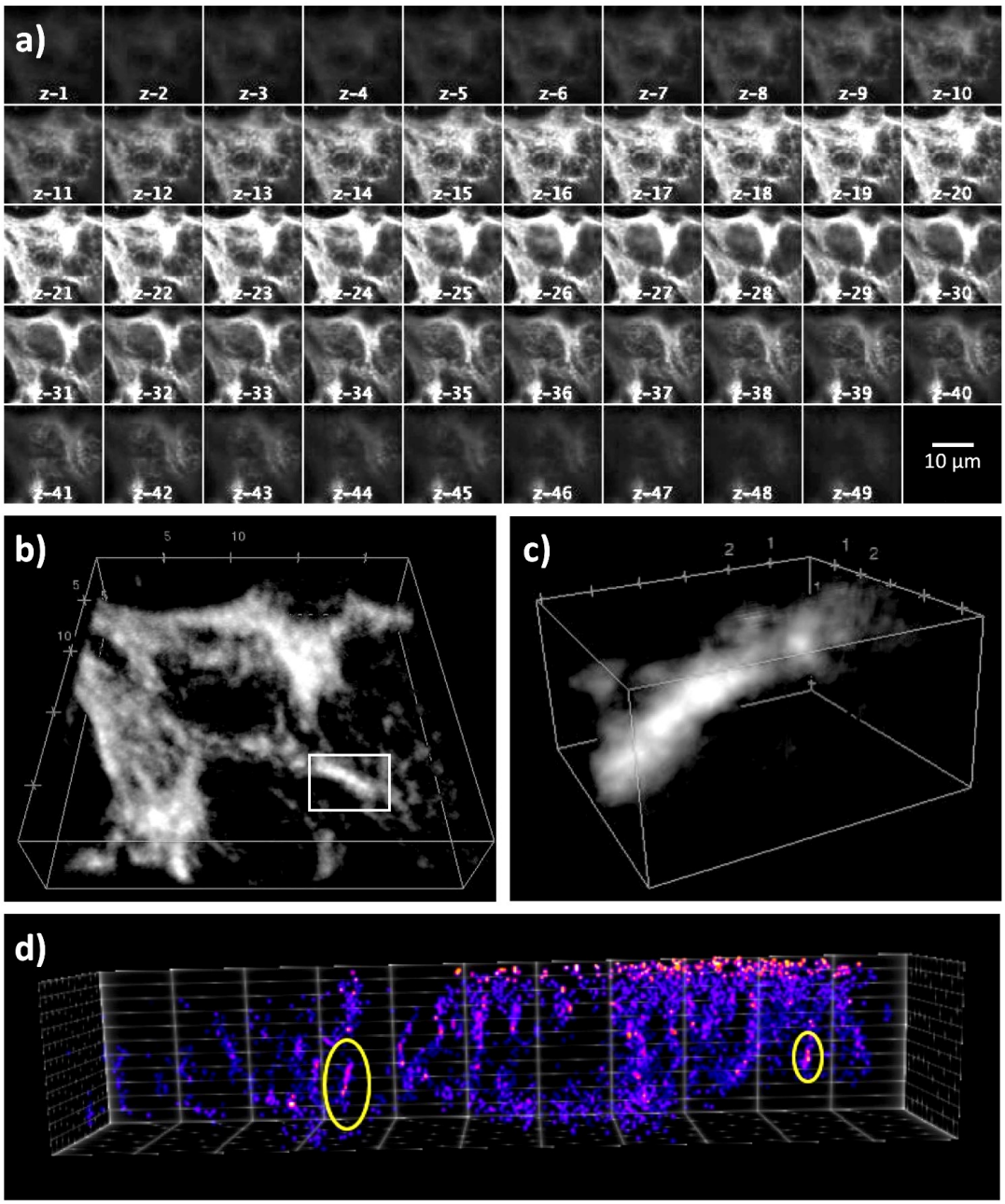

Figure 3.21: 3D analysis of microtubules. (a) Confocal images of 49 frames that contain six types of QDs ("all") in emission ranges of 490 and 800 nm). (b) Conventional 3D view of microtubules processed by ImageJ (Image scale: 5 μm). (c) Zoomed-in image of white rectangle region seen in (b) with an image scale of 1 μm. (d) Side image of localisations.

Table 3.9: Microscopy settings for 3D imaging of microtubules.

Parameters			**Settings**	
# of QDs			6	
QD525	**Emission Ranges (nm)**	**Gain (V)**	490-540	794
QD565			540-575	778
QD585			575-595	708
QD605			595-625	696
QD655			625-675	661
QD705			675-800	813
ALL			490-800	834
Scan size (μm)			23.31x23.31x5.52	
Scan format (pixel)			256x256	
Pixel size (nm)			91	
# of z-sections			49	
Step size (nm)			115	
Scan speed (Hz)			400	
Scanning direction			Unidirectional	
Line:Frame Averaging			2:4	
Time per colour per section (sec)			5.12	
Laser intensity (Wcm^{-2})			0.214	
Bit depth			8	

microtubule is seen to be consistent with the conventional confocal image, there are plenty of inaccurate localisations found along the z-direction. The artefacts produced axially are prominently seen in yellow circles in Figure 3.21d. It is noteworthy that the identification of artefacts, here, can come from a priori knowledge about the structure of microtubules, which is already known and understood.

A common reason for this is the poor estimation of the PSF of the system by the software, more prominently axially than laterally, due to the fact that Abbe's limit on spatial resolution goes by an extra factor of 1/NA axially. The elongated geometry of the PSF, and the difference between axial and lateral resolution in optical microscopy, simply stem from the non-symmetrical wavefront that emerges from the objective. Therefore, the software finds localisations from neighbouring out-of-focus planes, whereas it is required to sift signals that have come from the same source and detected in different sections. An example to solve this problem is shown in Figure 3.22. Suppose that there are two pixels, a and b, in adjacent planes in z axis, z_1 and z_2 respectively, and located in the centre of the PSF. If the software calculates and checks

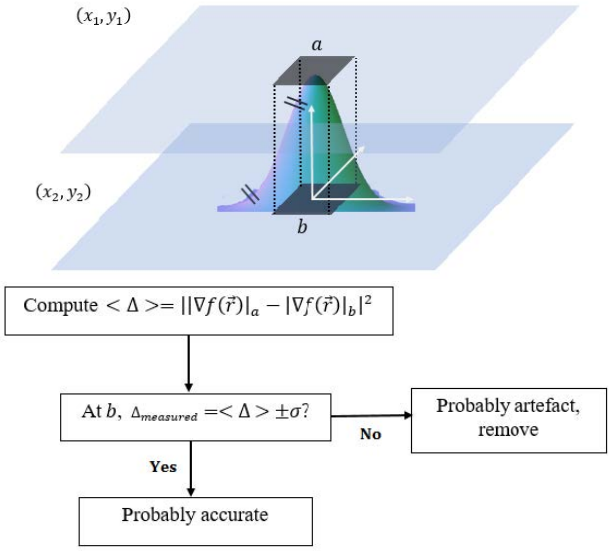

Figure 3.22: Graphical depiction of a PSF centred two pixels "a" and "b", and a hypothetical algorithm for axial artefact removal in the 3D analysis of QDOSS.

the expected magnitude of the PSF at z_1 and z_2, it is able to consider it as either an artefact or a real localisation. In other words, let's say the theoretical difference in the gradient of the PSF in pixel "a" and "b" is:

$$< \Delta >= ||\nabla f(\overrightarrow{r})|_a - |\nabla f(\overrightarrow{r})|_b|^2 \tag{3.2}$$

and the measured one is $\Delta_{measured}$, if $\Delta_{measured}$ is significantly different from $< \Delta >$ at "b", the algorithm can accept it as a new localisation. Otherwise, it should discard this result as an artefact. Since, for now, we are not able to modify the algorithm that GDSC-SMLM uses, we continued to use QDOSS in 2D multicolour imaging, which will be discussed in the next section.

3.4 Neuron imaging

After testing QDOSS on a reference structure, triangular DNA origami, and a well-known continuous structure in the cell, microtubule, we decided to use QDOSS in multicolour imaging of two structures that are localised around the synaptic cleft. Synaptic connection is one of the essential cellular communications in the brain, and

involves in the memory formation and the cognitive processes [125, 126]. Therefore, understanding of not only the physical structure but also the dynamic molecular mechanism around the synaptic environment is crucial in neuroscience [127–129]. However, whereas the synaptic active zone is within 300±150 nm, the width of the synaptic cleft is around 20 nm and the size of a synaptic vesicle varies around 35-50 nm, which falls below the diffraction limit of conventional optical microscopy [93, 96]. For this purpose, we targeted either two receptors, N-methyl-D-aspartate receptor (NMDAR) and α-amino-3-hydroxy-5-methyl-4-isoxazolepropionic acid receptor (AMPAR) in a postsynaptic region, or two structural proteins Bassoon and Homer1 or Piccolo and PSD95 in presynaptic and postsynaptic regions, respectively. Although super-resolved images of several synaptic proteins and receptors have been constructed via using STORM and PALM in previous studies [95, 96], we aimed to observe the same structures with QDOSS as it has a potential to achieve faster SR imaging at low intensities compared to STORM. Additionally, here, we used QDOSS in multicolour imaging of synaptic structures differently from the previous DNA and microtubule imaging experiments.

Usually in multicolour imaging studies, while one of the structures of interest is coloured red, the other one is coloured green. So that, if the two structures are colocalised, it is seen as yellow in the overlay of the two images where they are colocalised. Therefore, in this part of the study, besides observing the QDs individually and all of them in one channel, we observed the group of QDs for each structure in a separate channel. Then after finding localisations, we used them for comparison of QDOSS and conventional confocal imaging. Figure 3.23 shows the schematic illustrations of the positions of these proteins and receptors in neurons around the synaptic cleft.

3.4.1 Immunostaining of proteins in neurons

Similar to alpha-tubulin staining, the same procedure was used to label postsynaptic and presynaptic proteins in nerve cells. The cells were seeded and cultured on coverslips, and were fixed with 4% paraformaldehyde (Thermo Scientific) in PBS for

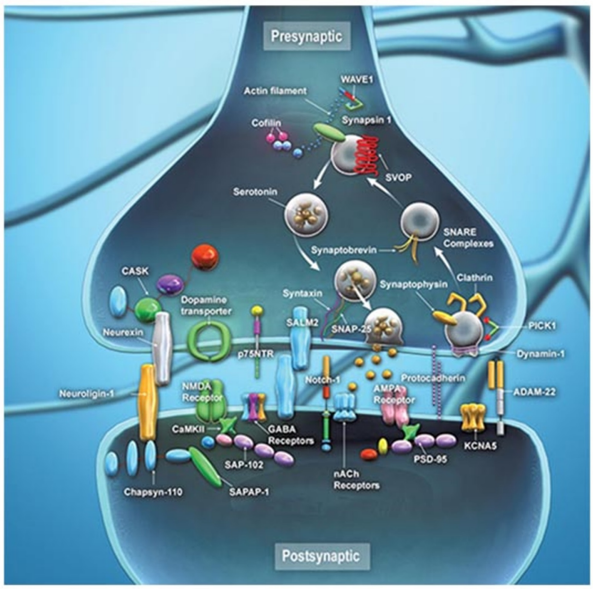

Figure 3.23: A schematic diagram of the organisation of the scaffold proteins, membrane receptors, signalling proteins and cell-adhesion molecules in the presynaptic and postsynaptic region. Figure sourced from [130].

15 minutes and permeabilised with 0.25% v/v Triton X-100 (Sigma Aldrich) in PBS for 15 minutes before staining. After washing with 1X PBS, cells were left for 30 minutes in 1-2 drops of each of the endogenous biotin blocking buffers (streptavidin and biotin blocking reagent) and for 1 hour in the blocking buffer (6% BSA/10% normal serum in PBS).

The fixed and permeabilised samples were incubated overnight with two types of primary antibodies: a monoclonal mouse anti-NMDAR2A antibody (Abcam, ab174636, 1:200) and a polyclonal rabbit anti-Glutamate Receptor 1 (Abcam, ab31232, 1:200), a monoclonal mouse Bassoon antibody (Novus Biologicals, SAP7F407, 1:200) and a polyclonal rabbit antibody against Homer 1 (Synaptic Systems, 160 003, 1:200); or a monoclonal mouse PSD-95 antibody (Novus Biologicals, 6G6-1C9, 1:200) and a polyclonal rabbit antibody, against Piccolo (Synaptic Systems, 142 003, 1:200); then in the blocking buffer at 4 °C. After primary antibody labelling, each type of QDs streptavidin conjugates (Invitrogen) with emission peaks at 525, 565, 585, 605, 655 and 705 nm was diluted to 20 nM in a secondary blocking buffer (6% BSA in PBS). Then, either a biotin-XX goat anti–mouse IgG secondary antibody (Invitrogen, B-2763,

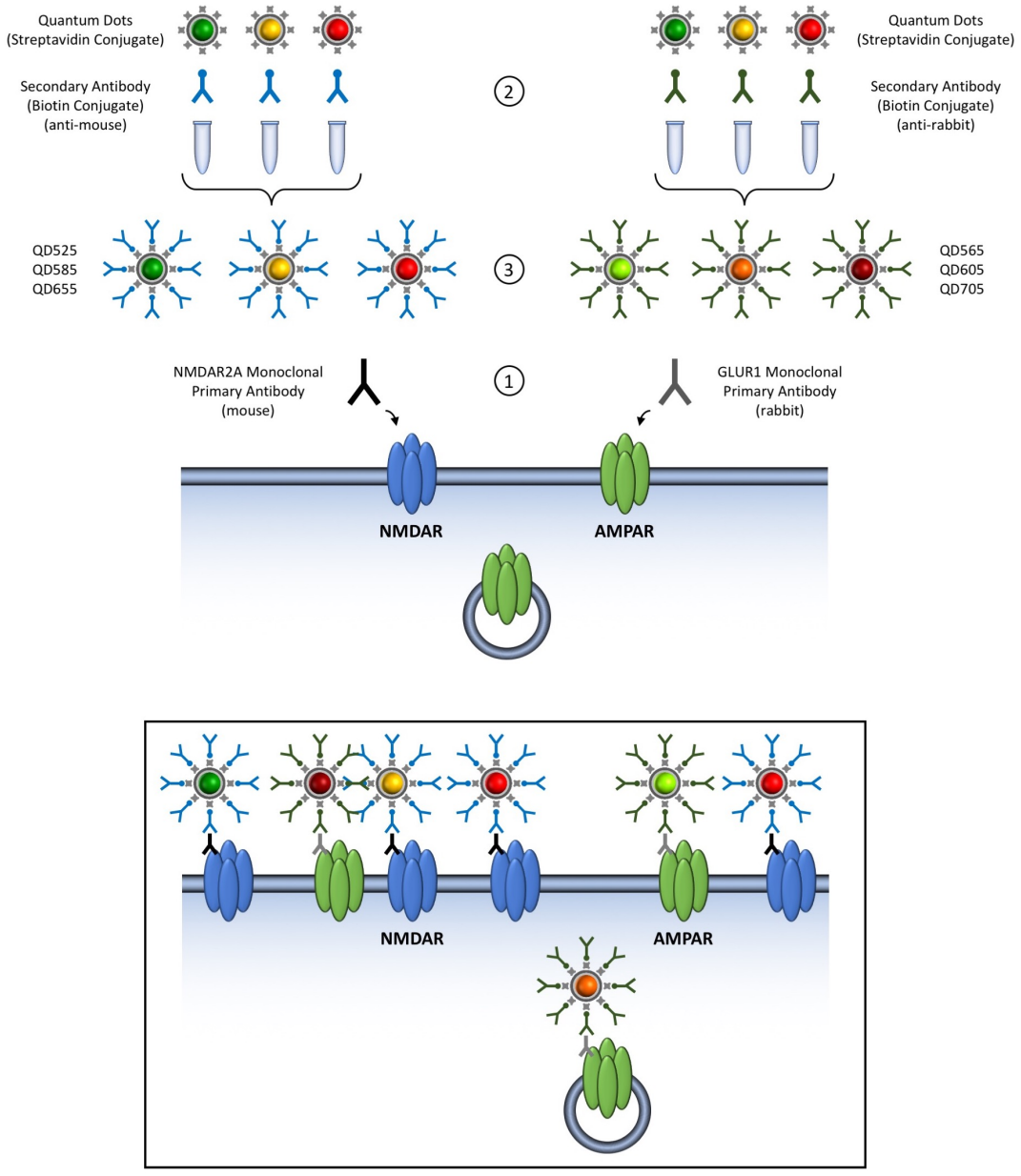

Figure 3.24: Schematic representation of QDOSS labelling of NMDAR and AMPAR in neurons for multicolour imaging.

Table 3.10: Microscopy settings for the multicolour imaging of NMDAR2A and GLUR1.

Parameters			**Settings**	
# of QDs			6	
QD525	**Emission Ranges (nm)**	**Gain (V)**	500-540 (NM)	671
QD565			540-575 (NM)	679
QD585			575-595 (NM)	608
QD605			605-640 (AM)	702
QD655			625-675 (AM)	725
QD705			675-800 (AM)	769
ALL			500-800	539
Scan size (μm)			16.45	
Scan format (pixel)			512x512	
Pixel size (nm)			32	
Scan speed (Hz)			400	
Scanning direction			Unidirectional	
Line:Frame Averaging			2:2	
Time per colour (sec)			5.12	
Laser intensity (Wcm^{-2})			0.306	
Bit depth			8	

1:500) was added to three of them (QD525, QD655 and QD705) or a biotin-XX goat anti–rabbit IgG secondary antibody (Invitrogen, B-2770, 1:500) was added the others (QD565, QD585 and QD605), and the secondary antibody and QD mixture were shaken for 1 hour at room temperature. Staining was followed by adding six colours of QDs streptavidin conjugates with secondary antibodies for 1 hour. Finally, cells were washed with ethanol and toluene and mounted with Cytoseal 60 (Thermo Fisher Scientific).

3.4.2 Multicolour imaging of NMDAR2A and GLUR1

NMDAR and AMPAR are important receptors for a neuron, and both have crucial functions in ion transportation through the membrane of a nerve cell. In this work, we labelled NMDAR2A, one of the subunits of NMDAR, with QD525, QD565 and QD585, and GLUR1, one of the subunits of AMPAR, with QD625, QD655 and QD705. The microscope conditions of the multicolour imaging of NMDAR2A and GLUR1 can be found in Table 3.10.

In Figure 3.25, it is seen that the white square region, where the two receptors are

Figure 3.25: Confocal images of NMDAR tagged by QD525, QD565 and QD585, and AMPAR tagged by QD625, QD655 and QD705, and 2D Gaussian peaks fitted using GDSC-SMLM. Image scale is 4 μm for each spectrally separated image and 250 nm for the zoomed-in image of super-resolved overlay image.

localised around the cell membrane, is analysed. As the detector of the microscope took the original images in greyscale (8-bit), we recoloured the images later. Since the software of the microscope has only 6 colours to be used, we used "blue" for the illustration of QD525, "cyan" for QD565, "green" for QD585, "yellow" for QD625, "red" for QD655 and "purple" for QD705. The image that covers all the QDs was left as "grey". For multicolour imaging of NMDAR and AMPAR, we recoloured the image of NMDAR (emission range: 500-595 nm) as "red" and AMPAR (emission range: 605-800 nm) as "green". The localisations were found from the images of three channels for each receptor with a resolution around down to 60 nm, and they are seen as "SR-NMDAR only" and "SR-AMPAR only" in Figure 3.25. The overlays of the two images are seen as "Merge" for the non-spectrally separated image and as "SR-Merge" for the super-resolved QDOSS image. If the bottom part of the membrane, where the two structures are seen as colocalised (i.e. yellow) in the "Merge" image, is zoomed in on, NMDAR and AMPAR can clearly be seen separately, even though they are close to each other down to 20 nm.

3.4.3 Multicolour imaging of Bassoon and Homer1

After the multicolour imaging of two postsynaptic receptors, we targeted two scaffolding proteins, one in the presynaptic region, Bassoon, and one in the postsynaptic region, Homer1. In the previous studies, they are shown to be clustered within a distance between 90 nm and 170 nm [95]. While Bassoon (Bs) was labelled with four types of QDs: QD565, QD585, QD605 and QD625, Homer1 was labelled with 3 types of QDs: QD525, QD655 and QD705. Each type of QDs was also observed in spectrally separated channels within emission ranges between 500 nm and 540 nm for QD525 (Hm), 540 nm and 575 nm for QD565 (Bs), 575 nm and 595 nm for QD585 (Bs), 595 nm and 615 nm for QD605 (Bs), 615 nm and 640 nm for QD625 (Bs), 640 nm and 675 nm for QD655 (Hm), and 675 nm and 750 nm for QD705 (Hm). For imaging of all of the QDs, an emission range between 500 nm and 850 nm was set. In order to compare multicolour imaging of QDOSS super-resolved localisations with conventional confocal imaging, we observed Bassoon and Homer1 only in emission

Table 3.11: Microscopy settings for the multicolour imaging of Bassoon and Homer1.

Parameters			Settings	
# of QDs			7	
QD525	**Emission Ranges (nm)**	**Gain (V)**	500-540 (Hm)	725
QD565			540-575 (Bs)	659
QD585			575-595 (Bs)	696
QD605			595-615 (Bs)	720
QD625			615-640 (Bs)	776
QD655			640-675 (Hm)	746
QD705			675-750 (Hm)	725
ALL			500-850	548
Scan size (μm)			20.87	
Scan format (pixel)			512x512	
Pixel size (nm)			41	
Scan speed (Hz)			400	
Scanning direction			Unidirectional	
Line:Frame Averaging			2:2	
Time per colour (sec)			5.12	
Laser intensity (Wcm^{-2})			0.239	
Bit depth			8	

ranges of 540-640 nm and 640-850 nm, respectively (Table 3.11).

Figure 3.26 shows fluorescence images of a general view of neurons and zoomed-in images that contain either all of the wavelengths of the QDs or their spectrally separated images, and their QDOSS localisations. For the region of interest, the white square region seen in Figure 3.26a was chosen, and zoomed in on for further imaging due to the fact that Bassoon and Homer1 are localised around synapses, and one of them is seen in the white square region of interest.

Although these two proteins are localised in either the pre- or postsynaptic region, the overlay image of "Bassoon only" and "Homer1 only" is seen as yellowish in Figure 3.26, which means that they are colocalised. Contrary to conventional methods, we also found 2D Gaussian fitting peaks of spectrally separated images and reconstructed the overlap images as seen in "SR-Bassoon only" and "SR-Homer1 only" in Figure 3.26. The resolutions are improved down to 47 nm with a precision of <9 nm in "SR-Bassoon only" and >56 nm with a precision of <9 nm in "SR-Homer1 only". Higher resolution is achieved in "SR-Bassoon only" than in "SR-Homer1 only" because Bassoon was labelled with four types of QDs and Homer1 was labelled with three different types of

Figure 3.26: Confocal images of neurons whose Bassoon (Bs) and Homer1 (Hm) proteins were labelled with QD565-QD585-QD605-QD625 and QD525-QD655-QD705, respectively. The white square region seen in (a) was spectrally separated and observed in 500-540 nm (Hm), 540-575 nm (Bs), 575-595 nm (Bs), 595-615 nm (Bs), 615-640 nm (Bs), 640-675 nm (Hm), 675-750 nm (Hm) and 500-850 nm for all QDs. Fluorescence image of "Merge" is an overlay image of "Bassoon only" and "Homer1 only", which contain only the emissions of QDs tagged to either Bassoon or Homer1. "SR Bassoon only" (green) and "SR Homer1 only" (red) are localisations found from spectrally separated images and their overlap image is shown in "SR Merge". Scale bar is 250 nm in zoomed-in images.

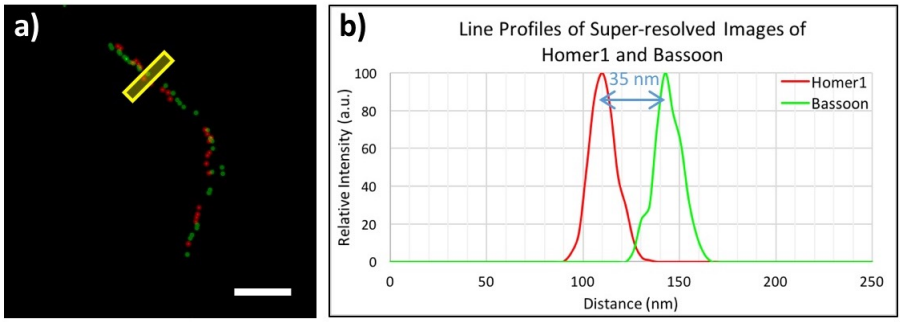

Figure 3.27: Line profile analysis of synaptic cleft proteins, Bassoon and Homer1. (a) QDOSS multicolour super-resolved image of white square seen in Figure 3.26a, and (b) line profiles of Homer1 (red) and Bassoon (green) localisations seen in the yellow area in (a). Scale bar is 250 nm.

QDs. It is obvious that the higher number of different QDs results in higher QDOSS resolution. What is more, the overlay of these two super-resolved images is seen in "SR-Merge" in Figure 3.26. Compared to the fluorescence overlay image, "Merge", Bassoon and Homer1 are seen to be localised on opposite sides of synapse.

As mentioned above, the distance between the two proteins' clusters varies from 90 nm to 170 nm [95]. However, the maximum distance between two localisation lines is measured as 70 nm in "SR-Merge", whereas the synaptic cleft with around 20 nm is clearly seen (Figure 3.27). The reason why the distance of two proteins is not found relevant to the literature might be that they were not observed from their "side" views, i.e. the synapse was oriented out of the imaging focal plane. Therefore, the criss-crossing pattern of the green and red peaks might be found. Further multicolour imaging was done to observe Piccolo and PSD95, and the results will be given in the following section.

3.4.4 Multicolour imaging of Piccolo and PSD95

In addition to Bassoon and Homer1 proteins, we also determined the positions of Piccolo, a presynaptic scaffolding protein, and PSD95 that is located on the postsynaptic side. According to the study of Dani and colleagues, the distance between Piccolo and PSD95 is from about 50 nm to 160 nm [95]. In this part of the study, each protein was labelled with 3 QDs at different emission wavelengths. On the one hand, Piccolo

Table 3.12: Microscopy settings for the multicolour imaging of Piccolo and PSD95.

Parameters			**Settings**	
# of QDs			6	
QD525	**Emission Ranges (nm)**	**Gain (V)**	500-540 (Pic)	650
QD565			540-575 (PSD)	621
QD585			575-595 (PSD)	637
QD605			595-625 (PSD)	642
QD655			625-675 (Pic)	639
QD705			675-800 (Pic)	689
ALL			500-800	617
Scan size (μm)			34.01	
Scan format (pixel)			512x512	
Pixel size (nm)			66	
Scan speed (Hz)			400	
Scanning direction			Unidirectional	
Line:Frame Averaging			2:2	
Time per colour (sec)			5.12	
Laser intensity (Wcm^{-2})			0.147	
Bit depth			8	

(Pic) was tagged by QD525, QD655 and QD705 and captured in the emission ranges of 500-540 nm, 625-675 nm and 675-800 nm, respectively. On the other hand, PSD95 (PSD) was tagged by QD565, QD585 and QD605, and spectrally separated images were captured from 540 to 575 nm for the imaging of QD565, from 575 to 595 nm for the imaging of QD585 and 595-625 nm for the imaging of QD605 (see Table 3.12 for other microscopy settings).

Figure 3.28 shows the confocal images of a general view of nerve cells and zoomed-in images of the white square region in different emission ranges. "ALL" image contains wavelengths from 500 nm up to 800 nm. We also obtained images of "Piccolo only" (red) and "PSD95 only" (green), and combined them using the overlay tool of ImageJ into a single image, "Merge".

As seen in the composite image of the Piccolo and PSD95, "Merge", in Figure 3.28, one may assume that they are colocalised due to the overlap between the red and green channels without any analysis. Thus, further analysis of finding 2D Gaussian fitting peaks was done on the spectrally separated images. The spatial resolution is achieved down to 88 nm and 62 nm in with a maximum localisation precision of 8 nm in "SR-Piccolo only" and "SR-PSD95 only", respectively (Figure 3.29). The

Figure 3.28: Confocal images and QDOSS localisations of Piccolo and PSD95 proteins. General view of neurons is seen on the left. The white square region was zoomed in on and observed in between 500-540 nm (QD525), 625-675 nm (QD655), 675-800 nm (QD705) for spectral imaging of Piccolo (Pic) and 540-575 nm (QD565), 575-595 nm (QD585) and 595-625 nm (QD605) for imaging of PSD95 (PSD). For a non-spectrally separated image, both structures were observed in between 500 nm and 800 nm (ALL). "Piccolo only" and "PSD95 only" cover the emissions of only Piccolo and PSD95 proteins, whereas "Merge" is their overlay image. 2D Gaussian peaks are seen in "SR-Piccolo only" and "SR-PSD95 only" for individual structure and in "SR-Merge" for the overlay image of Piccolo (red) and PSD95 (green). Scale bar of the zoomed-in images is 500 nm.

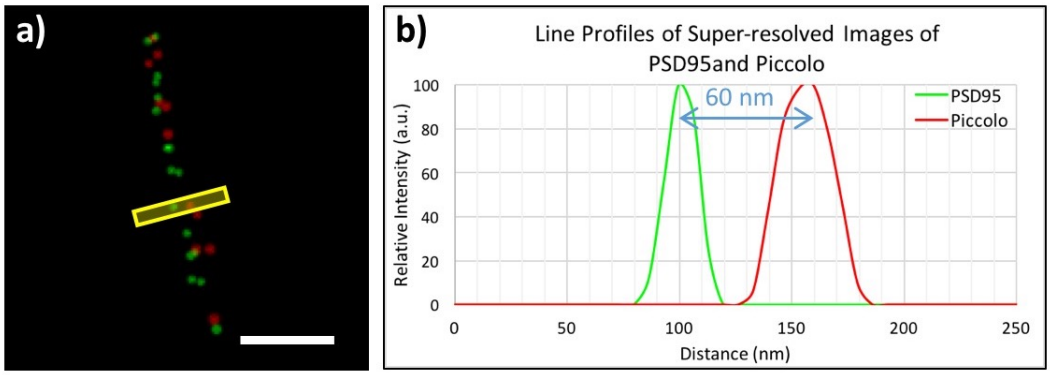

Figure 3.29: Line profile analysis of synaptic cleft proteins, PSD95 and Piccolo. (a) QDOSS multicolour super-resolved image of white square seen in Figure 3.28a, and (b) line profiles of Piccolo (red) and PSD95 (green) localisations seen in the yellow area in (a). Scale bar is 250 nm.

improvement in the resolution couldn't be obtained below 62 nm because of using a lower number of QDs for labelling, which increases the probability of localisation of QDs with similar emission wavelengths within the diffraction limit. However, in the overlay image of them, "SR-Merge", the two proteins could be separated at about 60 nm that is in the range of 50 nm and 160 nm as defined by Dani et al. [95]. Although this is somewhat suggestive of a correctly super-resolved image of Piccolo and PSD95, they are not seen in two well-separated regions.

3.4.5 Carbon quantum dots as bioimaging probes

As we carried out QDOSS experiments and developed it using off-the-shelf QDs streptavidin conjugate from Invitrogen so far, we decided to use home-made QDs to achieve super-resolved images. While germanium QDs were being used for spectroscopic super-resolution microscopy imaging in the previous studies of our group, due to their low quantum yield (<1%) and unknown surface chemistry, we attempted to use carbon QDs (CQDs), which were synthesised and characterised by one of our group members, Nikolaos Papaioannou.

For the source of carbon in the QDs, either glucose or chitosan was used as a precursor. 4% w/v aqueous solution of each precursor was prepared and placed in a Teflon lined, stainless steel autoclave. It was treated hydrothermally at 200 °C for

12 hours. The CQDs were obtained from the liquid phase at the end of the reaction. Then, they were dried and resuspended in dH_2O as a final concentration of 50 mg/mL. Optical and chemical characterisations of the synthesised CQDs were done by Nikolaos. Figure 3.30a shows high-resolution transmission electron microscopy (TEM) image of chitosan CQD. Since electron beam induces sample crystalisation, TEM images were recorded at lower accelerating voltage of 80 kV for two minutes. Based on the TEM images, the size distribution of the CQDs are 5.2$\pm$0.8 nm in the glucose-derived CQDs and 7.9$\pm$1.6 nm in the chitosan CQDs. According to electron diffraction pattern and infrared spectroscopy data, the synthesised CQDs consist of crystalline graphitic structures with carboxyl groups on their surface, including amorphous-like carbon particles. Figure 3.30c shows a proposed structure of synthesised CQDs.

As for the photoluminescence measurements, the maximum peaks of excitation and emission wavelengths of the CQDs were found as 340 nm and 440 nm with a QY of 1.5% in the precursor of glucose and 360 nm and 440 nm with a QY of 10.5% in the precursor of chitosan. Because the carboxyl groups were found on the surface of the CQDs, we functionalised the surface of the CQDs with streptavidin as described in the study of Quevedo and his colleagues [131]. 32 μL of EDC, 1-Ethyl-3-(3-dimethylaminopropyl)carbodiimide, (150 mM) and 16 μL of sulfo-NHS, N-hydroxysulfosuccinimide, (300 mM) were added to 800 μL of the colloidal suspension, followed by stirring at room temperature for 1 hour. Subsequently, 80 μL of streptavidin solution (dissolved in potassium phosphate buffer, 0.2 M, pH 6.5) was added to the mixture and shaken for overnight at room temperature.

Since streptavidin conjugated CQDs can be targeted to biotinylated anti-alpha-tubulin antibody (Ab), we applied them to HEK293T cells as described in section 3.3.1. In order to control whether any signal is coming from the cells or Ab (i.e. autofluorescence), an "only cell" and a "cell with only Ab" samples were prepared as a negative sample and a positive control sample, respectively. For comparison and to understand whether streptavidin modification has been worked or not, (i) non-specific staining of the synthesised-CQDs only and (ii) the mixture of them with alpha-tubulin Ab were applied with (iii) specific staining of streptavidin conjugated CQDs with Ab.

Table 3.13: Microscopy settings for imaging of microtubules labelled with Glucose or Chitosan CQDs.

Parameters	**Glucose CQDs**		**Chitosan CQDs**	
	CQD only	**CQD+AB**	**CQD only**	**CQD+AB**	**CQD(St)+AB**
Emission Range (nm)	490-800	490-800	490-800	490-800	490-800
Gain (V)	703	672	676	672	656
Scan size (μm)	49.17	59.52	59.58	59.52	59.52
Scan format (pixel)	512x512	512x512	512x512	512x512	512x512
Pixel size (nm)	96	116	116	116	116
Scan speed (Hz)	400	400	400	400	400
Scanning direction	Unidirectional	Unidirectional	Unidirectional	Unidirectional	Unidirectional
Line:Frame Averaging	4:2	4:2	2:2	4:2	2:2
Data Acquisition Time	10.24	10.24	5.12	10.24	5.12
Laser intensity (Wcm^{-2})	0.085	0.07	0.042	0.07	0.07
Bit depth	8	8	8	8	8

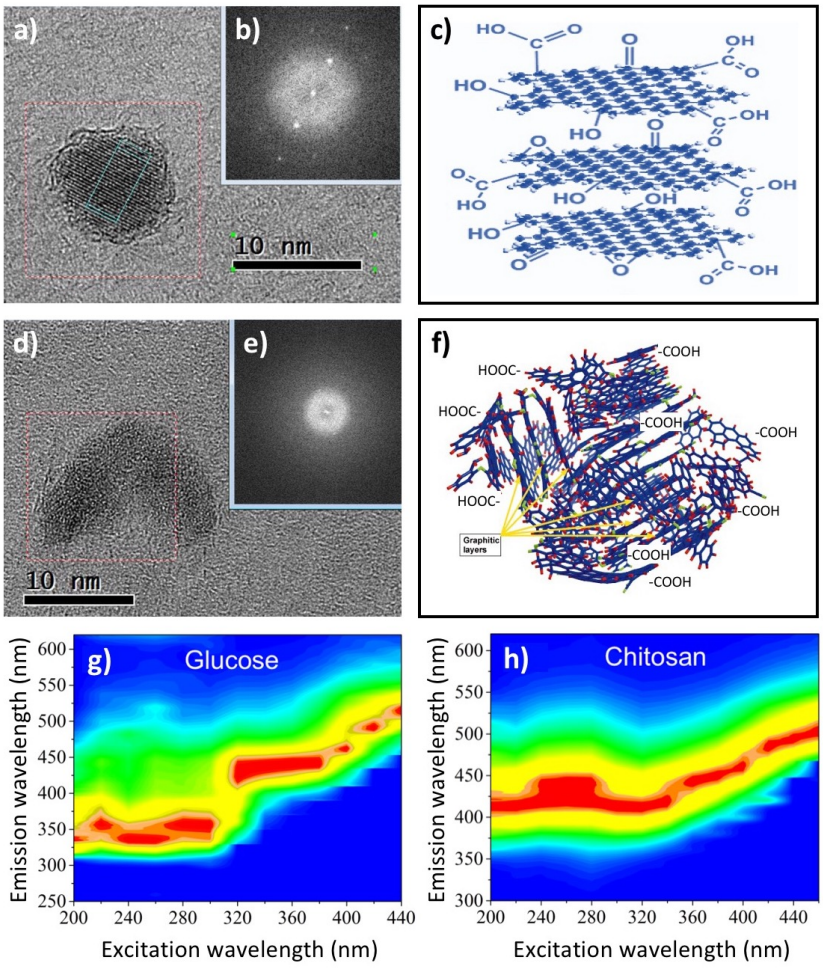

Figure 3.30: High-resolution TEM image (a,d) and electron diffraction pattern (b,e) of crystalline (a,b) and amorphous (d,e) chitosan CQD. Schematic representation of proposed structures of crystalline graphitic structure (c) and soot model (f) of CQDs. Figures in (c) and (f) are sourced from [132, 133].

Table 3.13 shows the microscopy settings of confocal imaging and Figure 3.31 shows the confocal images of the staining. As seen in Figure 3.31, the brightness of the images is higher in the images of CQDs synthesised from the precursor of chitosan than in the glucose ones, which verifies the results of QYs of the QDs. Furthermore, since there is no specific staining in non-functionalised CQDs only and CQDs with Ab, the QDs are seen to be dispersed in the cytoplasm of the cells in Figure 3.31a, b, d and e. However, accumulation of "glucose CQD with Ab" or "chitosan QD only" in the cytoplasm shows that either Abs or CQDs non-specifically bound to cytoplasmic structures with their functional groups, e.g. –COOH or –OH. In the control samples

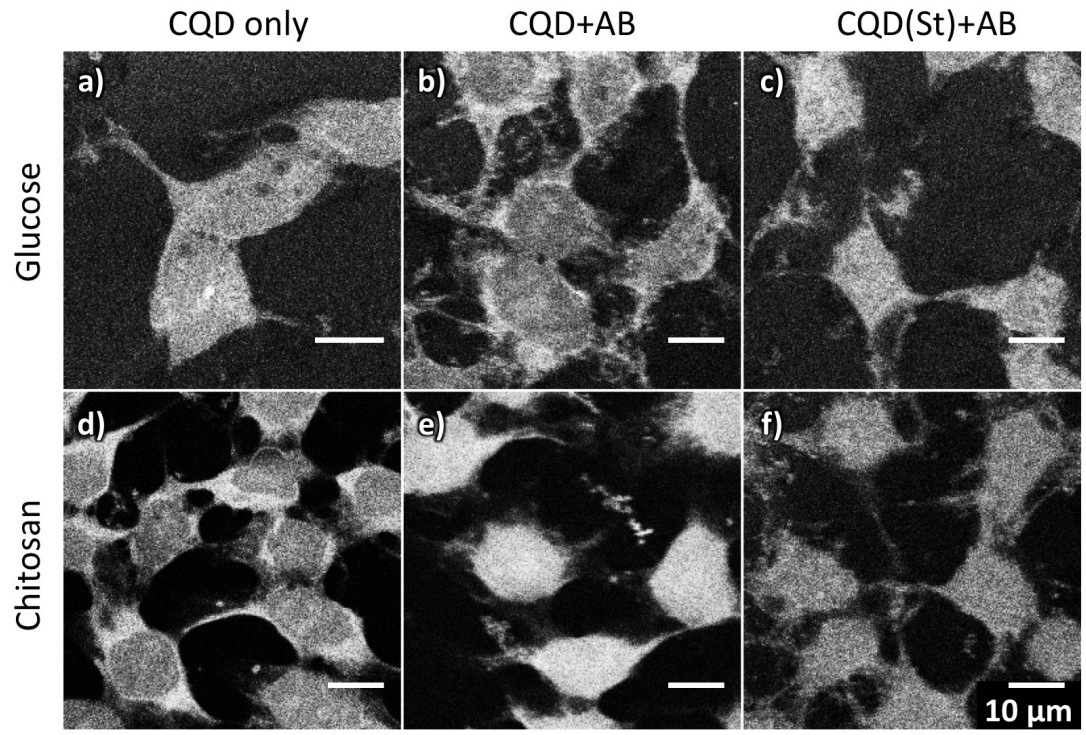

Figure 3.31: Fluorescence images of carbon QDs, which were synthesised from precursors of either (a-c) glucose or (d-f) chitosan. The cells were tagged by (a and d) only CQDs, (b and e) CQDs with biotinylated antibody, and (c and f) streptavidin conjugated CQDs with biotinylated antibody. Scale bar is 10 μm.

("only cell" and "cells with only Ab") (not shown in Figure), no signal was captured, so it is determined that the signals seen in Figure 3.31 would stem from CQDs.

Despite the fact that the biotinylated Abs were targeted to alpha-tubulin subunits of the microtubules and the streptavidin conjugated CQDs have a high affinity to the biotinylated structures, the microtubules are not clearly seen to be stained in Figure 3.31c and f. This might be caused by that the functional groups of the QDs were covered during functionalisation process or the CQDs were not sufficiently functionalised with streptavidin. Thus, a more systematic study is required of CQD systems (e.g. including "dynamic light scattering" at each step of the surface modification to verify changes in particle size). Additionally, the concentrations should be optimised before using them in cellular studies. What is more, the biocompatibility of the CQDs before and after surface modification needs to be tested for live-cell imaging.

Finally, it should also be discussed in here that the spatial resolution of the QDOSS

approach is limited by the size of the QDs (see Appendix C). Therefore, surface modifications of the QDs with linker molecules and streptavidin-like proteins lead to increase in size, which inversely affect the resolution. Besides, together with attaching to the structure of interest through an antibody causes to high localisation precision, which might also have prevented us from observing the structures in more detail in the previous experiments.

Chapter 4

CONCLUSION AND FUTURE WORK

4.1 Conclusion

In this thesis, we have demonstrated that sub-diffraction (down to 40 nm) imaging can be achieved by our QDOSS method, using a mixture of off-the-shelf QDs with several distinctive well-separated peak emission wavelengths. For the purpose of localising different types of QDs located within the diffraction limit, we used the Leica TCS SP2 Laser Scanning Confocal Microscope with a spectroscopic capability for imaging the samples, and GDSC-SMLM, a plugin of ImageJ, for the 2D Gaussian fitting process. In the first place, we carried out fundamental characterisations, such as sample drifting and gain analysis of the microscope, for further studies and analysis. According to the images of 500 nm fluorescent beads for 95 seconds, the sample drift was less than 1.5 nm within a minute, and it was concluded that it was negligible, as we observed the samples in a few seconds. Additionally, we calculated the camera gain (ADU/photon) at the various voltages supplied, based on the variance and mean of the pixel values in the sets of calibration images. It was necessary to compute the number of photons in the localisation using the signal divided by the gain.

After calibration of the system, we tested our method against standard structures: 180 bp of DNA ruler (61.2 nm in length) and triangular DNA origami with a side

length of 120 nm. Although the assembly of each DNA strand of the DNA ruler was verified by gel electrophoresis, the QDs weren't localised in the range of the length of the ruler due to its flexible structure. Hence, it was decided that DNA origami would be used. Two or three different types of QDs that were modified by different ssDNA were attached to middle positions of the sides of the triangular DNA origami using the programmed assembly of DNA. It was shown that the QDs could be localised within 60 nm to 90 nm by the GDSC-SMLM software, and this was also verified by AFM images. It was concluded that GDSC-SMLM was suitable for finding 2D localisations of QDs.

Following DNA testing, we compared QDOSS with one of the current SR techniques, STORM, which localises the fluorophores on a temporal basis instead of spectral separation as QDOSS does. For this purpose, we labelled alpha-tubulin subunits of microtubules in HEK293T cells with 6 types of QDs. First, we used the blinking properties of QDs and took 10,000 STORM images of microtubules for 7.5 minutes. It was found that the resolution could be improved from 280 nm to 78 nm. Then, we observed the same sample under a standard confocal microscope. Contrary to STORM, the spectral property of the QDs was used in QDOSS, and instead of 10,000 images, we took only 6 images because the structure was tagged with QDs at six different emission wavelengths. Both in high and low imaging formats, resolution lower than 50 nm was achieved by QDOSS, while the data acquisition time was down to 320 milliseconds per channel. Here, one of the advantages of QDOSS is shown to be that spatial resolution can be improved below the diffraction limit, even in subsecond time resolution. In addition, despite the fact that other super-resolution techniques, such as STED, can achieve a super-resolved image in milliseconds, they have to use high light intensity (more than 600 Wcm^{-2}) on the sample. However, the laser power requirements on samples were significantly reduced (varied between 0.084 and 0.491 Wcm^{-2}) with our QDOSS approach.

We used spectral slicing to observe the HEK293T cells in 30 frames with 10 nm emission wavelengths from 490 nm to 790 nm in order to check whether observing the same QD in different channels (or overlapped emission wavelengths) affects the

spatial resolution or not. Since we labelled the microtubules with 6 types of QDs and observed them in 30 frames, the same QDs should have been localised in more than one channel. If they are localised in the same position, the resolution is not improved compared to six frames. Otherwise, we should find a more super-resolved image. Based on the results discussed in section 3.3.5, the resolution remained almost the same with the previous imaging results. Therefore, we can conclude that, even if the emission ranges of different QDs are overlapped, or the same QDs are observed in more than one spectral frame, they are not localised separately, i.e. the resolution is not improved. As described in section 3.4.3 and 3.4.4, the spatial resolution of QDOSS is directly related to the number of types of QDs used. While the resolution can be achieved down to 40 nm with 6 different colours of QDs, it can be down to about 60 nm and 80 nm if you use 3 and 4 different types of QDs, respectively.

We carried out 3D QDOSS imaging and found that the software could find localisation artefacts coming from consecutive sections. We proposed an algorithm for this problem that the software should compute the gradient of the PSF and check whether the difference of the signal matches to the calculated one or not. If so, it should discard the localisation; otherwise, it should accept it.

Resistance of QDs to bleaching makes possible to label and track the cells for a long period of time. This, together with the fast acquisition times demonstrated in this work, provide a clear potential for long term live cell super-resolution imaging. This is because both STED-like and STORM/PALM-like super-resolution techniques have fundamental drawbacks in achieving super-resolution imaging with faster acquisition times at lower intensities at the same time.

Another important usage of QDOSS approach is in multicolour imaging, especially for colocalisation studies. The problem of other super-resolution methods for multicolour imaging is that several fluorophores in the same sample require being excited by multiple lasers at different wavelengths. This takes extra time to finalise the super-resolved image. On the other hand, owing to the fact that QDs are used in the QDOSS and multiple QDs can be excited by a laser at the same wavelength, super-resolution images can be obtained using a single laser. Even though the locali-

sations of the proteins were not in the range of expected values, they were localised separately at least 20 nm, which is the width of synaptic cleft, apart from each other.

As far as other advantages of QDOSS over current SR techniques are concerned, sub-diffraction images can be obtained using a standard confocal fluorescence microscope (e.g. Leica TCS SP series, Zeiss LSM series with QUASAR detector) that is capable of spectral signal separation. Contrary to other SR microscopies, which need special equipment and microscopy set-up such as multiphoton lasers with a pulse, QDOSS can, in principle, be adapted to any confocal or even fluorescence microscope including those equipped with EM-CCDs by using a suitable spectral filtering adapter (e.g. Andor multi-wavelength adapter or similar). In such a case, there is an additional advantage of using 2D detector leading to sub-millisecond acquisition time.

Currently, the major drawback of the QDOSS approach is the low number of detection channels (i.e. colours) and a requirement for neighbouring QDs to be of different peak emission wavelength. The former can be addressed by using a larger selection QDs with distinctive (and narrow, 10 nm) emission wavelengths by further improvement in size separation of QDs at the synthesis stage. This, however, is ultimately limited by the intrinsic QDs emission peak broadening and overlap. The latter, so far, has not been controlled in our experiments, as we used a random of mixture of QDs, allowing for the possibility (inversely proportional to the number of distinctive peak wavelength used) of QDs with similar peak emission wavelength being closer than the diffraction limit, that would result in a compromised resolution.

Thus, we see future directions in developing of QD-based probes of smaller size (e.g. CQD-based), narrow emission peak width (e.g. via better sample purification following synthesis and/or development of new synthesis methods) and further development and investigation of targeting protocols (e.g. via development of direct binding protocols for CQDs).

4.2 Future work

As far as the future work is concerned, there are several works to be pursued. Firstly, the labelling protocols can be developed to enable more cellular structures being labelled. Furthermore, by improving the localisation software and using biocompatible QDs, QDOSS studies can be developed to observe 3D live-cell for a long term. For the 3D reference structures, a nanoscale 3D DNA box can be used [134].

As the preliminary results of using CQDs in QDOSS imaging has been given in this thesis, it should be broadened by additional characterisation experiments. In addition to studying the surface of carbon nanoparticles and developing related labelling protocols, the sufficiency of streptavidin modification of the surface of CQDs, and their stability and cytotoxicity, especially in different cellular environments, should be investigated. One should remember that the quantum yield of the QDs can be influenced by the pH of the environment and the chemical properties of the conjugated groups on the surface. Thus, a comprehensive work is required in the spectroscopic super-resolution imaging with CQDs. This can also be extended to a comparative study of bioimaging via using different QDs, such as gold and silicon QDs.

To conclude, with regards to the improvements of spatial and temporal resolution achieved by Quantum Dot-based Optical Spectral Separation (QDOSS) microscopy in this thesis, there are further applications of QDOSS to be performed in cellular imaging. QDOSS microscopy may be compatible with live cell imaging as it takes place at low intensities of light. Besides, since QDs are used in QDOSS as fluorophores, it also sets to stage for super-resolution imaging of live cells for a long term. In addition to this, thanks to its fast acquisition time, it makes possible to capture highly dynamic nature of live cell activities. What is more, by the additional algorithms to GDSC-SMLM, super-resolved QDOSS imaging in three dimensions would be possible. Certainly, not only in QDOSS, the future developments in super-resolution optical microscopy will rely on new optical methods, more efficient algorithms and more suitable fluorescent probes, as previously happened, for understanding biological activities and problems at the nanoscale, and this knowledge and the curiosity will lead the humanity into other "rooms at the bottom".

Appendix A

Triangular DNA Origami Sequences

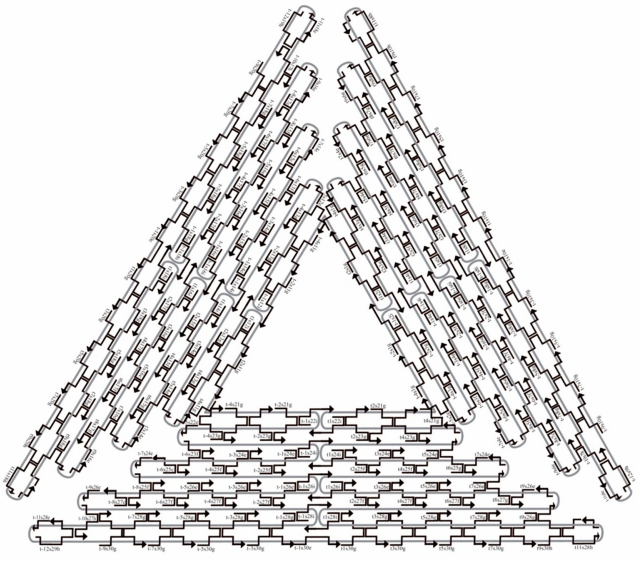

Figure A.1: Triangular DNA origami.

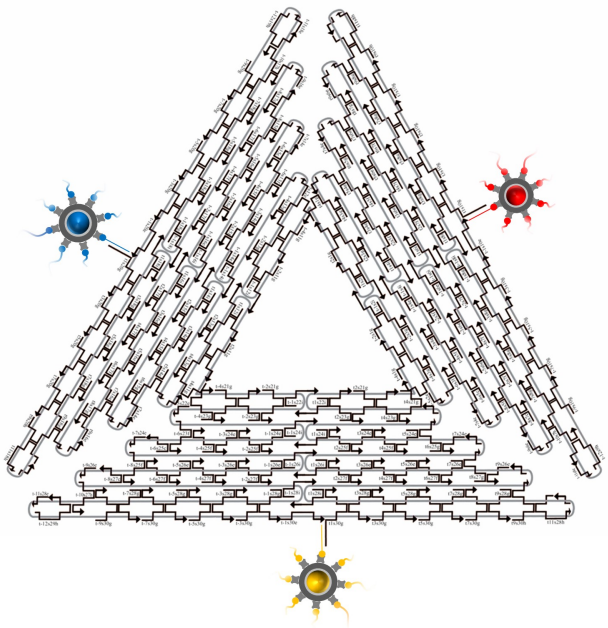

Figure A.2: Quantum Dots modifications on triangular DNA origami.

Table A.1: List of unmodified staple strands.

Oligo Name	Sequence (5′-3′)
t11s18h	AATACTGCGGAATCGTAGGGGGTAATAGTAAAATGTTTAGACT
t11s28h	TCTTTGATTAGTAATAGTCTGTCCATCACGCAAATTAACCGTT
t11s8h	CAGAAGGAAACCGAGGTTTTTAAGAAAAGTAAGCAGATAGCCG
t1s12i	TCATATGTGTAATCGTAAAACTAGTCATTTTC
t1s14i	GTGAGAAAATGTGTAGGTAAAGATACAACTTT
t1s16i	GGCATCAAATTTGGGGCGCGAGCTAGTTAAAG
t1s18i	TTCGAGCTAAGACTTCAAATATCGGGAACGAG
t1s22i	TCGGGAGATATACAGTAACAGTACAAATAATT
t1s24i	CCTGATTAAAGGAGCGGAATTATCTCGGCCTC
t1s26i	GCAAATCACCTCAATCAATATCTGCAGGTCGA
t1s28i	CGACCAGTACATTGGCAGATTCACCTGATTGC
t1s2i	CGGGGTTTCCTCAAGAGAAGGATTTTGAATTA
t1s4i	AGCGTCATGTCTCTGAATTTACCGACTACCTT

t1s6i	TTCATAATCCCCTTATTAGCGTTTTTCTTACC
t1s8i	ATGGTTTATGTCACAATCAATAGATATTAAAC
t2s11g	AGAAAAGCCCCAAAAAGAGTCTGGAGCAAACAATCACCAT
t2s13g	ACAGTCAAAGAGAATCGATGAACGACCCCGGTTGATAATC
t2s15f	ATAGTAGTATGCAATGCCTGAGTAGGCCGGAG
t2s17f	AACCAGACGTTTAGCTATATTTTCTTCTACTA
t2s1g	GATAAGTGCCGTCGAGCTGAAACATGAAAGTATACAGGAG
t2s21g	CCTGATTGCTTTGAATTGCGTAGATTTTCAGGCATCAATA
t2s23g	TGGCAATTTTTAACGTCAGATGAAAACAATAACGGATTCG
t2s25f	AAGGAATTACAAAGAAACCACCAGTCAGATGA
t2s27f	GGACATTCACCTCAAATATCAAACACAGTTGA
t2s3g	TTTGATGATTAAGAGGCTGAGACTTGCTCAGTACCAGGCG
t2s5f	CCGGAACCCAGAATGGAAAGCGCAACATGGCT
t2s7f	AAAGACAACATTTTCGGTCATAGCCAAAATCA
t3s10g	GTCAGAGGGTAATTGATGGCAACATATAAAAGCGATTGAG
t3s14e	CAATATGACCCTCATATATTTTAAAGCATTAA
t3s16e	CATCCAATAAATGGTCAATAACCTCGGAAGCA
t3s18g	AACTCCAAGATTGCATCAAAAAGATAATGCAGATACATAA
t3s20g	CGCCAAAAGGAATTACAGTCAGAAGCAAAGCGCAGGTCAG
t3s24e	TAATCCTGATTATCATTTTGCGGAGAGGAAGG
t3s26e	TTATCTAAAGCATCACCTTGCTGATGGCCAAC
t3s28g	AGAGATAGTTTGACGCTCAATCGTACGTGCTTTCCTCGTT
t3s30g	AGAATCAGAGCGGGAGATGGAAATACCTACATAACCCTTC
t3s4e	TGTACTGGAAATCCTCATTAAAGCAGAGCCAC
t3s6e	CACCGGAAAGCGCGTTTTCATCGGAAGGGCGA
t3s8g	CATTCAACAAACGCAAAGACACCAGAACACCCTGAACAAA

t4s11g	GCAAATATTTAAATTGAGATCTACAAAGGCTACTGATAAA
t4s13g	CGTTCTAGTCAGGTCATTGCCTGACAGGAAGATTGTATAA
t4s15f	CAGGCAAGATAAAAATTTTTAGAATATTCAAC
t4s17f	GATTAGAGATTAGATACATTTCGCAAATCATA
t4s1g	TAGCCCGGAATAGGTGAATGCCCCCTGCCTATGGTCAGTG
t4s21g	GCGCAGAGGCGAATTAATTATTTGCACGTAAATTCTGAAT
t4s23g	GATTATACACAGAAATAAAGAAATACCAAGTTACAAAATC
t4s25f	TAGGAGCATAAAAGTTTGAGTAACATTGTTTG
t4s27f	TGACCTGACAAATGAAAAATCTAAAATATCTT
t4s3g	TTTAACGGTTCGGAACCTATTATTAGGGTTGATATAAGTA
t4s5f	CTCAGAGCATATTCACAAACAAATTAATAAGT
t4s7f	GGAGGGAATTTAGCGTCAGACTGTCCGCCTCC
t5s10g	GATAACCCACAAGAATGTTAGCAAACGTAGAAAATTATTC
t5s14e	TTAATGCCTTATTTCAACGCAAGGGCAAAGAA
t5s16e	TTAGCAAATAGATTTAGTTTGACCAGTACCTT
t5s18g	TAATTGCTTTACCCTGACTATTATGAGGCATAGTAAGAGC
t5s20g	AACACTATCATAACCCATCAAAAATCAGGTCTCCTTTTGA
t5s24e	AATGGAAGCGAACGTTATTAATTTCTAACAAC
t5s26e	TAATAGATCGCTGAGAGCCAGCAGAAGCGTAA
t5s28g	GAATACGTAACAGGAAAAACGCTCCTAAACAGGAGGCCGA
t5s30g	TTAAAGGGATTTTAGATACCGCCAGCCATTGCGGCACAGA
t5s4e	CCTTGAGTCAGACGATTGGCCTTGCGCCACCC
t5s6e	TCAGAACCCAGAATCAAGTTTGCCGGTAAATA
t5s8g	TTGACGGAAATACATACATAAAGGGCGCTAATATCAGAGA
t6s15g	ATAAAGCCTTTGCGGGAGAAGCCTGGAGAGGGTAG
t6s17f	TAAGAGGTCAATTCTGCGAACGAGATTAAGCA

t6s25g	TCAATAGATATTAAATCCTTTGCCGGTTAGAACCT
t6s27f	CAATATTTGCCTGCAACAGTGCCATAGAGCCG
t6s5g	CAGAGCCAGGAGGTTGAGGCAGGTAACAGTGCCCG
t6s7f	ATTAAAGGCCGTAATCAGTAGCGAGCCACCCT
t7s10g	ATAAGAGCAAGAAACATGGCATGATTAAGACTCCGACTTG
t7s14e	ATGACCCTGTAATACTTCAGAGCA
t7s16e	TAAAGCTATATAACAGTTGATTCCCATTTTTG
t7s18g	CGGATGGCACGAGAATGACCATAATCGTTTACCAGACGAC
t7s20g	GATAAAAACCAAAATATTAAACAGTTCAGAAATTAGAGCT
t7s24e	ACAATTCGACAACTCGTAATACAT
t7s26e	TTGAGGATGGTCAGTATTAACACCTTGAATGG
t7s28g	CTATTAGTATATCCAGAACAATATCAGGAACGGTACGCCA
t7s30g	GAATCCTGAGAAGTGTATCGGCCTTGCTGGTACTTTAATG
t7s4e	GCCGCCAGCATTGACACCACCCTC
t7s6e	AGAGCCGCACCATCGATAGCAGCATGAATTAT
t7s8g	CACCGTCACCTTATTACGCAGTATTGAGTTAAGCCCAATA
t8s17g	TAATTGCTTGGAAGTTTCATTCCAAATCGGTTGTA
t8s27g	CGCGAACTAAAACAGAGGTGAGGCTTAGAAGTATT
t8s7g	AGCCATTTAAACGTCACCAATGAACACCAGAACCA
t9s10h	TATCTTACCGAAGCCCAAACGCAATAATAACGAAAATCACCAG
t9s16e	ACTAAAGTACGGTGTCGAATATAA
t9s18g	TGCTGTAGATCCCCCTCAAATGCTGCGAGAGGCTTTTGCA
t9s20h	AAAGAAGTTTTGCCAGCATAAATATTCATTGACTCAACATGTT
t9s26e	ACCACCAGCAGAAGATGATAGCCC
t9s28g	TAAAACATTAGAAGAACTCAAACTTTTTATAATCAGTGAG
t9s30h	GCCACCGAGTAAAAGAACATCACTTGCCTGAGCGCCATTAAAA

t9s6e	CCATTAGCAAGGCCGGGGGAATTA
t9s8g	GAGCCAGCGAATACCCAAAAGAACATGAAATAGCAATAGC
t10s17h	ACCAACCTAAAAAATCAACGTAACAAATAAATTGGGCTTGAGA
t10s27h	AACTCACATTATTGAGTGTTGTTCCAGAAACCGTCTATCAGGG
t10s7h	ACGACAATAAATCCCGACTTGCGGGAGATCCTGAATCTTACCA
t12s19h	CCTGACGAGAAACACCAGAACGAGTAGGCTGCTCATTCAGTGA
t12s29h	ACGTGGACTCCAACGTCAAAGGGCGAATTTGGAACAAGAGTCC
t12s9h	TGCTATTTTGCACCCAGCTACAATTTTGTTTTGAAGCCTTAAA
t1s10e	AGAGAATAACATAAAAACAGGGAAGCGCATTA
t1s12i	AGGGATAGCTCAGAGCCACCACCCCATGTCAA
t1s14e	ATTTTCTGTCAGCGGAGTGAGAATACCGATAT
t1s14i	CAACAGTTTATGGGATTTTGCTAATCAAAAGG
t1s16e	ATTCGGTCTGCGGGATCGTCACCCGAAATCCG
t1s16i	GCCGCTTTGCTGAGGCTTGCAGGGGAAAAGGT
t1s18g	CGACCTGCGGTCAATCATAAGGGAACGGAACAACATTATT
t1s18i	GCGCAGACTCCATGTTACTTAGCCCGTTTTAA
t1s20e	ACAGGTAGAAAGATTCATCAGTTGAGATTTAG
t1s22i	CGCGTCTGATAGGAACGCCATCAACTTTTACA
t1s24e	CAGTTTGACGCACTCCAGCCAGCTAAACGACG
t1s24i	AGGAAGATGGGGACGACGACAGTAATCATATT
t1s26e	GCCAGTGCGATCCCCGGGTACCGAGTTTTTCT
t1s26i	CTCTAGAGCAAGCTTGCATGCCTGGTCAGTTG
t1s28g	TTTCACCAGCCTGGCCCTGAGAGAAAGCCGGCGAACGTGG
t1s28i	CCTTCACCGTGAGACGGGCAACAGCAGTCACA
t1s2i	CCTTTTTTCATTTAACAATTTCATAGGATTAG
t1s30e	CGAGAAAGGAAGGGAAGCGTACTATGGTTGCT

t1s4e	TTATCAAACCGGCTTAGGTTGGGTAAGCCTGT
t1s4i	TTTAACCTATCATAGGTCTGAGAGTTCCAGTA
t1s6e	TTAGTATCGCCAACGCTCAACAGTCGGCTGTC
t1s6i	AGTATAAAATATGCGTTATACAAAGCCATCTT
t1s8g	TTTCCTTAGCACTCATCGAGAACAATAGCAGCCTTTACAG
t1s8i	CAAGTACCTCATTCCAAGAACGGGAAATTCAT
t2s11g	CCTCAGAACCGCCACCCAAGCCCAATAGGAACGTAAATGA
t2s13g	AGACGTTACCATGTACCGTAACACCCCTCAGAACCGCCAC
t2s15f	CACGCATAAGAAAGGAACAACTAAGTCTTTCC
t2s17f	ATTGTGTCTCAGCAGCGAAAGACACCATCGCC
t2s1g	AAAACAAAATTAATTAAATGGAAACAGTACATTAGTGAAT
t2s21g	GCTCATTTTTTAACCAGCCTTCCTGTAGCCAGGCATCTGC
t2s23g	GTAACCGTCTTTCATCAACATTAAAATTTTTGTTAAATCA
t2s25f	ACGTTGTATTCCGGCACCGCTTCTGGCGCATC
t2s27f	CCAGGGTGGCTCGAATTCGTAATCCAGTCACG
t2s3g	AGAGTCAAAAATCAATATATGTGATGAAACAAACATCAAG
t2s5f	ACTAGAAATATATAACTATATGTACGCTGAGA
t2s7f	TCAATAATAGGGCTTAATTGAGAATCATAATT
t3s10g	AACGTCAAAAATGAAAAGCAAGCCGTTTTTATGAAACCAA
t3s14e	GTTTTGTCAGGAATTGCGAATAATCCGACAAT
t3s16e	GACAACAAGCATCGGAACGAGGGTGAGATTTG
t3s18g	TATCATCGTTGAAAGAGGACAGATGGAAGAAAAATCTACG
t3s20g	TTAATAAAACGAACTAACCGAACTGACCAACTCCTGATAA
t3s24e	TGTAGATGGGTGCCGGAAACCAGGAACGCCAG
t3s26e	GGTTTTCCATGGTCATAGCTGTTTGAGAGGCG
t3s28g	GTTTGCGTCACGCTGGTTTGCCCCAAGGGAGCCCCCGATT

t3s30g	TAGAGCTTGACGGGGAGTTGCAGCAAGCGGTCATTGGGCG
t3s4e	GATTAAGAAATGCTGATGCAAATCAGAATAAA
t3s6e	CACCGGAATCGCCATATTTAACAAAATTTACG
t3s8g	AGCATGTATTTCATCGTAGGAATCAAACGATTTTTTGTTT
t4s11g	AGGTTTAGTACCGCCATGAGTTTCGTCACCAGGATCTAAA
t4s13g	AGCGTAACTACAAACTACAACGCCTATCACCGTACTCAGG
t4s15f	TAGTTGCGAATTTTTTCACGTTGATCATAGTT
t4s17f	GTACAACGAGCAACGGCTACAGAGGATACCGA
t4s1g	GAGCAAAAGAAGATGAGTGAATAACCTTGCTTATAGCTTA
t4s21g	GTTAAAATTCGCATTAATGTGAGCGAGTAACACACGTTGG
t4s23g	GGATAGGTACCCGTCGGATTCTCCTAAACGTTAATATTTT
t4s25f	AGTTGGGTCAAAGCGCCATTCGCCCCGTAATG
t4s27f	CGCGCGGGCCTGTGTGAAATTGTTGGCGATTA
t4s3g	ACATAGCGCTGTAAATCGTCGCTATTCATTTCAATTACCT
t4s5f	GTTAAATACAATCGCAAGACAAAGCCTTGAAA
t4s7f	CCCATCCTCGCCAACATGTAATTTAATAAGGC
t5s10g	TCCCAATCCAAATAAGATTACCGCGCCCAATAAATAATAT
t5s16e	AACAGCTTGCTTTGAGGACTAAAGCGATTATA
t5s18g	CCAAGCGCAGGCGCATAGGCTGGCAGAACTGGCTCATTAT
t5s20g	ACCAGTCAGGACGTTGGAACGGTGTACAGACCGAAACAAA
t5s26e	TGCTGCAAATCCGCTCACAATTCCCAGCTGCA
t5s28g	TTAATGAAGTTTGATGGTGGTTCCGAGGTGCCGTAAAGCA
t5s30g	CTAAATCGGAACCCTAAGCAGGCGAAAATCCTTCGGCCAA
t5s6e	GTGTGATAAGGCAGAGGCATTTTCAGTCCTGA
t5s8g	ACAAGAAAGCAAGCAAATCAGATAACAGCCATATTATTTA
t6s13f	ACAGACAGCCCAAATCTCCAAAAAAAAATTTCTTA

t6s15c	CGAGGTGAGGCTCCAAAAGGAGCC
t6s17f	ACCCCCAGACTTTTTCATGAGGAACTTGCTTT
t6s23f	CGGCGGATTGAATTCAGGCTGCGCAACGGGGGATG
t6s25c	TGGCGAAATGTTGGGAAGGGCGAT
t6s27f	TGTCGTGCACACAACATACGAGCCACGCCAGC
t6s3f	TCCCTTAGAATAACGCGAGAAAACTTTTACCGACC
t6s5c	GTTTGAAATTCAAATATATTTTAG
t6s7f	AATAGATAGAGCCAGTAATAAGAGATTTAATG
t7s10g	GCCAGTTACAAAATAATAGAAGGCTTATCCGGTTATCAAC
t7s18g	AAAACACTTAATCTTGACAAGAACTTAATCATTGTGAATT
t7s20g	ACCTTATGCGATTTTATGACCTTCATCAAGAGCATCTTTG
t7s28g	TTCCAGTCCTTATAAATCAAAAGAGAACCATCACCCAAAT
t7s30g	CAAGTTTTTTGGGGTCGAAATCGGCAAAATCCGGGAAACC
t7s8g	GCGCCTGTTATTCTAAGAACGCGATTCCAGAGCCTAATTT
t8s15f	CGGTTTATCAGGTTTCCATTAAACGGGAATACACT
t8s17c	GGCAAAAGTAAAATACGTAATGCC
t8s25f	TCTTCGCTATTGGAAGCATAAAGTGTATGCCCGCT
t8s27c	GCGCTCACAAGCCTGGGGTGCCTA
t8s5f	TTCTGACCTAAAATATAAAGTACCGACTGCAGAAC
t8s7c	TCAGCTAAAAAAGGTAAAGTAATT
t9s10g	ACGCTAACGAGCGTCTGGCGTTTTAGCGAACCCAACATGT
t9s20g	TGGTTTAATTTCAACTCGGATATTCATTACCCACGAAAGA
t9s30g	CGATGGCCCACTACGTATAGCCCGAGATAGGGATTGCGTT
tsrem1	GCGCTTAATGCGCCGCTACAGGGC
t5s2et6s23c3T	TTAATTAATTTTTTACCATATCAAA
t7s4et8s25c2T	TTAATTTCATCTTAGACTTTACAA

t9s6et10s27c1T	C T G T C C A G A C G T A T A C C G A A C G A
t11s8et12s29c0T	T C A A G A T T A G T G T A G C A A T A C T
t5s12et6s3c3T	T G T A G C A T T C C T T T T A T A A A C A G T T
t7s14et8s5c2T	T T T A A T T G T A T T T C C A C C A G A G C C
t9s16et10s7c1T	A C T A C G A A G G C T T A G C A C C A T T A
t11s18et12s9c0T	A T A A G G C T T G C A A C A A A G T T A C
t5s22et6s13c-T	G T G G G A A C A A A T T T C T A T T T T T G A G
t7s24et8s15c2T	C G G T G C G G G C C T T C C A A A A A C A T T
t9s26et10s17c1T	A T G A G T G A G C T T T T A A A T A T G C A
t11s28et12s19c0T	A C T A T T A A A G A G G A T A G C G T C C

Table A.2: List of modified staple strands.

Oligo Name	Sequence (5′-3′)
Sticky End t1s10g	A G A G A A T A A C A T A A A A A C A G G G A A G C G C A T T A T G T G G T G G T G
Sticky End t1s20g	A C A G G T A G A A A G A T T C A T C A G T T G A G A T T T A G G C A T G G G C G G
Sticky End t1s30g	C G A G A A A G G A A G G G A A G C G T A C T A T G G T T G C T A G C T T T G A G G
Complementary Biotin 1	Biotin - A A A A A C A C C A C C A C A
Complementary Biotin 2	Biotin - A A A A A C C G C C C A T G C
Complementary Biotin 3	Biotin - A A A A A C C T C A A A G C T

Appendix B

Localisation parameters

The information of the localisation parameters can be found in the user manual of Genome Damage and Stability Centre (GDSC) Single Molecule Light Microscopy (SMLM) plugins [135]. The calibrations of "Initial StdDev0", "Initial StdDev1" and "Initial Angle" of the point spread function were automatically calculated using the "PSF Calculator" of GDSC-SMLM, and the localisations were found by using "Peak Fit". As a spot filter, "mean" was used, and the images were filtered once before finding the local maxima to simplify the process. The parameters of "smoothing", "search width", "border" and "fitting width" are the factors that are applied to the "Initial StdDev0" and "Initial StdDev1", Gaussian function widths. The final integer values are used by the software. Since the smoothing of the image alters the original signal, no "Smoothing" was applied, and it was set to 0. The sizes of the regions for finding the local maxima and fitting each peak were controlled by "Search width" and "Fitting width", and they were set to 0.5-1 and 2-3, respectively. Whereas increasing the "search width" from 1 reduces the number of true maxima by eliminating the fitting candidates, the "fitting width" was set up to 3, in order to cover up to 99.7% of the Gaussian function and to fit it in the entire spot region. The "Border", which defines the number of pixels bordering a localisation to be ignored, was set to its minimum value, 0.5. As a statistical method in "fit solver", the least-squares estimation is used for the estimations to minimise the sum of the squared errors whilst fitting the PSF on a candidate maximum. In the estimation process, the software computes

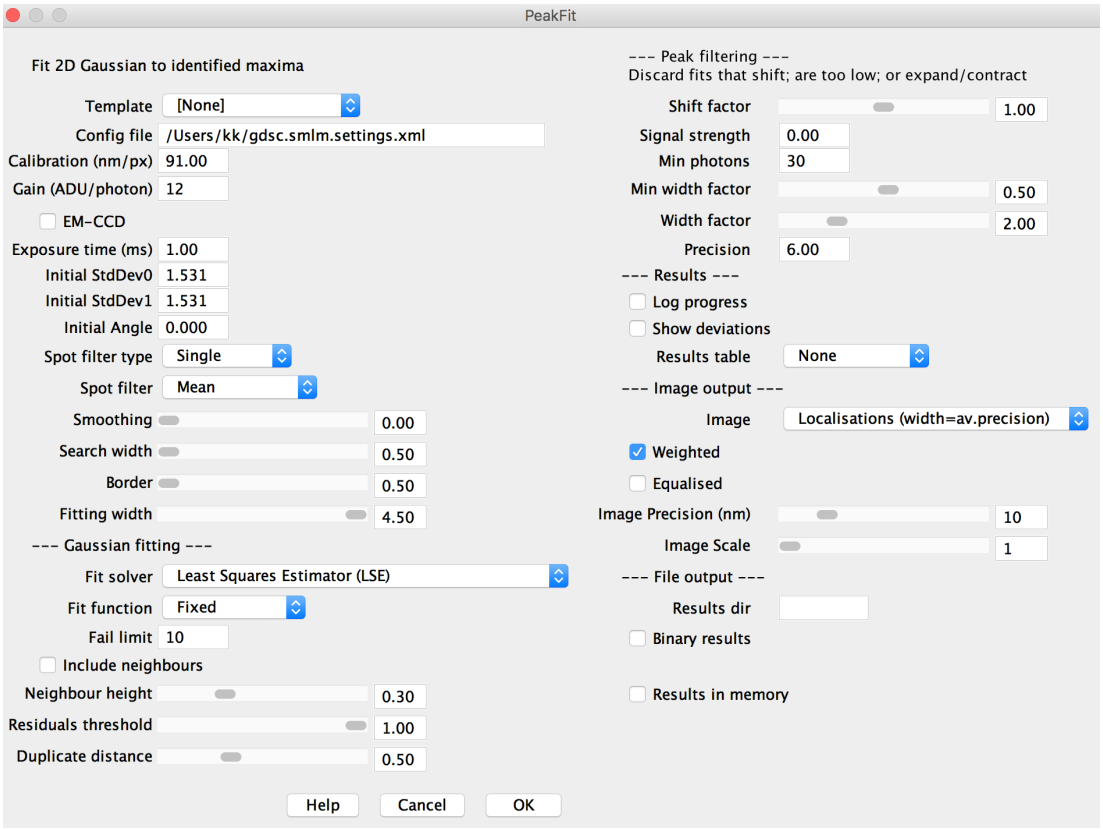

Figure B.1: An illustration of a parameter interface for "Peak Fit" in GDSC-SMLM plugin. Depending on the microscopy conditions, the options and the inputs vary in the parameters.

the gradient of the function through the Levenberg–Marquardt algorithm, and default parameters of the algorithm were used. The type of the 2D Gaussian function was set to "fixed", which fits the function to a fixed position in X and Y dimensions. As for the "fail limit", it specifies the number of failures that stop processing the image, and it was set to 10 to simplify the calculation. The localisation precision threshold of the fittings can be determined in the "precision" (in nm), i.e. the software discards any peak with a localisation precision above this value. As far as the "image output" is concerned, the "weighted" localisations in the constructed image were plotted using "localisations (width=av.precision)", which specifies the width of the spots as the same size of "image precision" (in nm). Finally, the image scale was set to 10 for producing the final reconstructed image. Figure B.1 presents an example of a "Peak Fit" window of GDSC-SMLM plugin.

Appendix C

Spatial resolution in QDOSS and the probability function

In the random labelling of QDs in QDOSS, there is a probability of the localisations of the same type of QDs, which have not distinctive emission profiles, in a sub-diffraction-sized region. In the QDOSS approach, the spatial resolution of the reconstructed image is inversely proportional to the number of QDs with different emission spectra. It can be easily inferred that the number of distinctive QDs should be higher than the number of QDs in the diffraction-limit area (i.e. ≈200 nm) for the perfect spatial localisations. In Figure C.1, one-dimensional (planar) and two-dimensional (planar) orientations of close-packed QDs are seen. It can be clearly illustrated by the fact that, in the linear arrangement of spherical particles, assume that they are 20 nm in diameter and randomly close-packed, there would be 12 spheres per 240 nm length, and there should be at least 12 different colours in order not to see the same colours along 240 nm. If we approach the problem from another side, consider that you have spheres with 6 different colours and don't want to arrange the same colours in the 240 nm periods linearly, the average distance of the intervals between their positions would be at least 40 nm. Therefore, it can be calculated as:

$$R = \frac{d}{m} \tag{C.1}$$

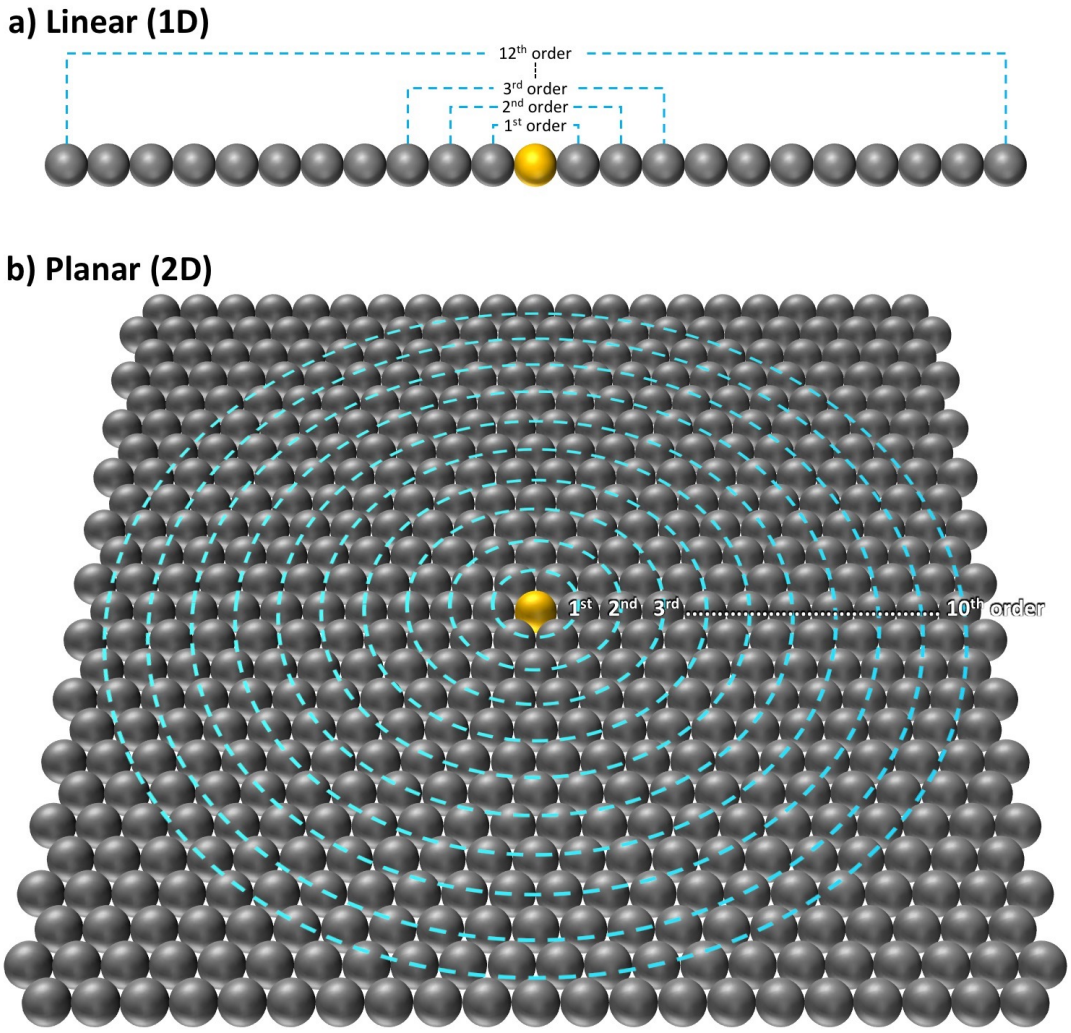

Figure C.1: Schematic view of positions of closest-packed QDs in (a) one dimension or (b) two dimensions.

where d is the size of the diffraction limit and m is the number of distinctive QDs. Since the spatial resolution in QDOSS is limited by the size of the QDs, the maximum m can be the maximum number of the positions of the QDs (k) that can be packed on the structure. Hence the minimum resolution that can be achieved in QDOSS can be calculated as:

$$R_{min} = \frac{d}{k} \tag{C.2}$$

Here, the total number of QDs in the given area depends on the dimensions that the

QDs are arranged in and the density of packing of the QDs. Thus, the maximum number of QDs can be calculated as:

$$k = \eta \left(\frac{d}{R_{QD}} \right)^{D} \tag{C.3}$$

where η is the density function, R_{QD} is the size of QD and D is the number of dimensions that QDs are packed in. The density function of the densest packing of equal spheres can be taken as 1 in linear packing (1D), $\frac{\pi}{2\sqrt{3}} \approx 0.9069$ in planar packing (2D) as found by Joseph Louis Lagrange in 1773 and $\frac{\pi}{3\sqrt{2}} \simeq 0.74048$ in face-centred cubic arrangements in three dimensions (3D) that was proved by Carl Friedrich Gauss in 1831 [136].

As for the probability of positioning of QDs, let's assume that there is an equal chance of being of all types of QDs at the same position (i.e. equal amount and excessive numbers of QDs for each type), the probability of one type of the QDs being at the position would be $1/m$, and the probability of not being there would be $\frac{m-1}{m}$. Consider that there are k positions, where QDs can be localised, in the given region, the probability of finding the same type of QDs anywhere in the region of interest can be calculated as the following equation:

$$P = 1 - \left(\frac{m-1}{m} \right)^{k-1} \tag{C.4}$$

where $k-1$ is the total number of neighbours of QDs in the given area.

Bibliography

[1] J. Pawley, J. B. Pawley, *Handbook of Biological Confocal Microscopy*, (Ed.: J. B. Pawley), Springer US, Boston, MA, **2006**, p. 985.

[2] T. C. Kriss, V. M. Kriss, *Neurosurgery* **1998**, *42*, 899–907.

[3] B. R. Masters in *Encyclopedia of Life Sciences*, John Wiley & Sons, Ltd, Chichester, UK, **2008**.

[4] G. W. White, *Introduction to Microscopy*, Butterworth, **1966**.

[5] MicroscopyU, Finite and Infinity Optical Systems, **2016**.

[6] H. Hertz, *Annalen der Physik und Chemie* **1887**, *267*, 983–1000.

[7] A. Einstein, *Annalen der Physik* **1905**, *322*, 132–148.

[8] B W, S G, Buried channel charge coupled devices, **1974**.

[9] M. F. Tompsett, Charge transfer imaging devices, **1978**.

[10] E. Karanasios, E. Stapleton, S. A. Walker, M. Manifava, N. T. Ktistakis, *Journal of Visualized Experiments* **2013**.

[11] Y. Hiraoka, J. W. Sedat, D. A. Agard, *Science* **1987**, *238*, 36–41.

[12] M. M. FREUNDLICH, *Science (New York N.Y.)* **1963**, *142*, 185–8.

[13] S. L. Flegler, J. W. Heckman, K. L. Klomparens, *Scanning and Transmission Electron Microscopy: An Introduction*, Oxford University Press, **1993**.

[14] E. M. Nelson, *Journal of the Royal Microscopical Society* **1910**, *30*, 282–289.

[15] A. Koehler in *New Method of Illimination for Phomicrographical Purposes*, Journal of the Royal Microscopical Society., **1894**, 261–262.

[16] R. D. Allen, G. B. David, G Nomarski, *Zeitschrift fur wissenschaftliche Mikroskopie und mikroskopische Technik* **1969**, *69*, 193–221.

[17] B. U. o. California, Optical paths for condensers yielding Critical and Kohler Illumination. **2015**.

[18] B. Alberts, A. Johnson, J. Lewis, M. Raff, K. Roberts, P. Walter, *Molecular Biology of the Cell, Fourth Edition*, 4th ed., Garland Science, **2002**.

[19] B. Pode-Shakked, H. Barash, L. Ziv, K. Gripp, E. Flex, O. Barel, K. Carvalho, M. Scavina, G. Chillemi, M. Niceta, E. Eyal, N. Kol, B. Ben-Zeev, O. Bar-Yosef, D. Marek-Yagel, E. Bertini, A. Duker, Y. Anikster, M. Tartaglia, A. Raas-Rothschild, *Clinical Genetics* **2017**, *91*, 725–738.

[20] R. R. M. Dijkstra, PhD thesis, University of Twente, **2012**, p. 36.

[21] R. S. (London), *Philosophical Transactions of the Royal Society of London: Giving Some Accounts of the Present Undertakings, Studies, and Labours, of the Ingenious, in Many Considerable Parts of the World*, **1852**.

[22] D. A. McQuarrie, J. D. Simon, *Physical Chemistry: A Molecular Approach*, University Science Books, **1997**.

[23] T. J. Chozinski, L. A. Gagnon, J. C. Vaughan, *FEBS Letters* **2014**, *588*, 3603–3612.

[24] B. N. G. Giepmans, S. R. Adams, M. H. Ellisman, R. Y. Tsien, *Science (New York N.Y.)* **2006**, *312*, 217–24.

[25] X. Michalet, *Science* **2005**, *307*, 538–544.

[26] *Principles of Fluorescence Spectroscopy*, 3rd ed., (Ed.: J. R. Lakowicz), Springer US, Boston, MA, **2006**.

[27] M. Fernández-Suárez, A. Y. Ting, *Nature reviews. Molecular cell biology* **2008**, *9*, 929–43.

[28] O SHIMOMURA, F. H. JOHNSON, Y SAIGA, *Journal of cellular and comparative physiology* **1962**, *59*, 223–39.

[29] S. J. Rosochacki, M. Matejczyk, *Acta microbiologica Polonica* **2002**, *51*, 205–16.

[30] K. A. Lukyanov, D. M. Chudakov, S. Lukyanov, V. V. Verkhusha, *Nature Reviews Molecular Cell Biology* **2005**, *6*, 885–890.

[31] X. Wu, H. Liu, J. Liu, K. N. Haley, J. A. Treadway, J. P. Larson, N. Ge, F. Peale, M. P. Bruchez, *Nature Biotechnology* **2003**, *21*, 41–46.

[32] W. C. Chan, S Nie, *Science (New York N.Y.)* **1998**, *281*, 2016–8.

[33] C. G. Galbraith, J. A. Galbraith, *Journal of Cell Science* **2011**, *124*, 1607–1611.

[34] M Bruchez, M Moronne, P Gin, S Weiss, A. P. Alivisatos, *Science (New York N.Y.)* **1998**, *281*, 2013–6.

[35] D. Ioannou, D. K. Griffin, *Nano Reviews* **2010**, *1*, 5117.

[36] W. C. W. Chan, D. J. Maxwell, X. Gao, R. E. Bailey, M. Han, S. Nie, *Current opinion in biotechnology* **2002**, *13*, 40–6.

[37] P. N. Prasad, *Nanophotonics*, John Wiley & Sons, Inc., Hoboken, NJ, USA, **2004**.

[38] E. E. Salpeter, *American Journal of Physics* **1997**, *65*, (Ed.: A. Lakhtakia), 933–934.

[39] L. E. Brus, *The Journal of Chemical Physics* **1984**, *80*, 4403–4409.

[40] J. M. Nedelijkovic, R. C. Patel, P. Kaufman, C. Joyce-Pruden, N. O'Leary, *Journal of Chemical Education* **1993**, *70*, 342.

[41] Olympus, Introduction to Confocal Microscopy, **2016**.

[42] M. Minsky, *Scanning* **1988**, *10*, 128–138.

[43] T Wilson, *Confocal Microscopy*, Acad. Press, **1990**.

[44] R. Lima, S. Wada, K.-i. Tsubota, T. Yamaguchi, *Measurement Science and Technology* **2006**, *17*, 797.

[45] Cellbiology, Group 6 Project - Confocal Microscopy, **2010**.

[46] T. Tanaami, S. Otsuki, N. Tomosada, Y. Kosugi, M. Shimizu, H. Ishida, *Appl. Opt.* **2002**, *41*, 4704–4708.

[47] S. L. Liu, Z. G. Wang, Z. L. Zhang, D. W. Pang, *Chemical Society Reviews* **2016**, *45*, 1211–1224.

[48] M. Abramowitz, M. W. Davidson, Diffraction of Light.

[49] E. Abbe, *Archiv für Mikroskopische Anatomie* **1873**, *9*, 413–418.

[50] Rayleigh, *Philosophical Magazine Series 5* **1879**, *8*, 261–274.

[51] A. Ashkin, J. M. Dziedzic, J. E. Bjorkholm, S. Chu, *Optics Letters* **1986**, *11*, 288.

[52] W. E. Moerner, L. Kador, *Physical Review Letters* **1989**, *62*, 2535–2538.

[53] E. Betzig, A. Lewis, A. Harootunian, M. Isaacson, E. Kratschmer, *Biophysical Journal* **1986**, *49*, 269–279.

[54] S. W. Hell, J. Wichmann, *Opt. Lett.* **1994**, *19*, 780–782.

[55] T. a. Klar, S Jakobs, M Dyba, A Egner, S. W. Hell, *Proceedings of the National Academy of Sciences of the United States of America* **2000**, *97*, 8206–8210.

[56] T. a. Klar, S. W. Hell, *Optics letters* **1999**, *24*, 954–6.

[57] A. Yildiz, J. N. Forkey, S. A. McKinney, T. Ha, Y. E. Goldman, P. R. Selvin, *Science* **2003**, *300*, 2061 LP –2065.

[58] M. G. L. Gustafsson, *Journal of Microscopy* **2000**, *198*, 82–87.

[59] S. Bretschneider, C. Eggeling, S. W. Hell, *Physical Review Letters* **2007**, *98*.

[60] E. Betzig, G. H. Patterson, R. Sougrat, O. W. Lindwasser, S. Olenych, J. S. Bonifacino, M. W. Davidson, J. Lippincott-Schwartz, H. F. Hess, *Science (New York N.Y.)* **2006**, *313*, 1642–1645.

[61] S. T. Hess, T. P. Girirajan, M. D. Mason, *Biophysical Journal* **2006**, *91*, 4258–4272.

[62] M. J. Rust, M. Bates, X. W. Zhuang, *Nat Methods* **2006**, *3*, 793–795.

[63] M. Neil, R. Juškaitis, T. Wilson, *Optics Communications* **1998**, *153*, 1–4.

[64] L. Schermelleh, P. M. Carlton, S. Haase, L. Shao, L. Winoto, P. Kner, B. Burke, M. C. Cardoso, D. A. Agard, M. G. L. Gustafsson, H. Leonhardt, J. W. Sedat, *Science (New York N.Y.)* **2008**, *320*, 1332–6.

[65] M. G. L. Gustafsson, *Proceedings of the National Academy of Sciences* **2005**, *102*, 13081–13086.

[66] Andor, Super-Resolution Imaging - Structured Illumination Microscopy.

[67] A. Einstein, *Deutsche Physikalische Gesellschaft* **1916**, *18*.

[68] B. Huang, M. Bates, X. Zhuang, *Annual Review of Biochemistry* **2009**, *78*, 993–1016.

[69] S. W. Hell, S. J. Sahl, M. Bates, X. Zhuang, R. Heintzmann, M. J. Booth, J. Bewersdorf, G. Shtengel, H. Hess, P. Tinnefeld, A. Honigmann, S. Jakobs, I. Testa, L. Cognet, B. Lounis, H. Ewers, S. J. Davis, C. Eggeling, D. Klenerman, K. I. Willig, G. Vicidomini, M. Castello, A. Diaspro, T. Cordes, *Journal of Physics D: Applied Physics* **2015**, *48*, 443001.

[70] D. Wildanger, B. R. Patton, H. Schill, L. Marseglia, J. P. Hadden, S. Knauer, A. Schönle, J. G. Rarity, J. L. O'Brien, S. W. Hell, J. M. Smith, *Advanced Materials* **2012**, *24*, OP309–OP313.

[71] N. Gustafsson, S. Culley, G. Ashdown, D. M. Owen, P. M. Pereira, R. Henriques, *Nature Communications* **2016**, *7*, 12471.

[72] M. Yamanaka, N. I. Smith, K. Fujita, Introduction to super-resolution microscopy, **2014**.

[73] R. A. Hoebe, C. H. Van Oven, T. W. J. Gadella, P. B. Dhonukshe, C. J. F. Van Noorden, E. M. M. Manders, *Nature Biotechnology* **2007**, *25*, 249–253.

[74] R. F. Laine, G. S. K. Schierle, S. van de Linde, C. F. Kaminski, *Methods and Applications in Fluorescence* **2016**, *4*, 22004.

[75] J. R. Allen, S. T. Ross, M. W. Davidson, *Journal of Optics* **2013**, *15*, 094001.

[76] H. Shroff, C. G. Galbraith, J. A. Galbraith, E. Betzig, *Nature Methods* **2008**, *5*, 417–23.

[77] A. Wyner, S. Shamai, *Proceedings of the IEEE* **1998**, *86*, 442–446.

[78] R. E. Thompson, D. R. Larson, W. W. Webb, *Biophysical Journal* **2002**, *82*, 2775–2783.

[79] G. B. Johnson, *The Living World*, McGraw-Hill Education, **2014**.

[80] H. Li, D. J. DeRosier, W. V. Nicholson, E. Nogales, K. H. Downing, *Structure* **2002**, *10*, 1317–1328.

[81] P. Kner, B. B. Chhun, E. R. Griffis, L. Winoto, M. G. L. Gustafsson, *Nature Methods* **2009**, *6*, 339–342.

[82] B. Hein, K. I. Willig, S. W. Hell, *Proceedings of the National Academy of Sciences* **2008**, *105*, 14271–14276.

[83] M. Bates, B. Huang, G. T. Dempsey, X. Zhuang, *Science* **2007**, *317*, 1749–1753.

[84] G. T. Dempsey, J. C. Vaughan, K. H. Chen, M. Bates, X. Zhuang, *Nature Methods* **2011**, *8*, 1027–1036.

[85] T. Kiuchi, M. Higuchi, A. Takamura, M. Maruoka, N. Watanabe, *Nature Methods* **2015**, *12*, 743–746.

[86] J. Fölling, M. Bossi, H. Bock, R. Medda, C. A. Wurm, B. Hein, S. Jakobs, C. Eggeling, S. W. Hell, *Nature Methods* **2008**, *5*, 943–945.

[87] Z. Zeng, X. Chen, H. Wang, N. Huang, C. Shan, H. Zhang, J. Teng, P. Xi, *Scientific reports* **2015**, *5*, 8359–1.

[88] Bálint, I. Verdeny Vilanova, Sandoval Álvarez, M. Lakadamyali, *Proceedings of the National Academy of Sciences* **2013**, *110*, 3375–3380.

[89] M. Heilemann, S. van de Linde, M. Schüttpelz, R. Kasper, B. Seefeldt, A. Mukherjee, P. Tinnefeld, M. Sauer, *Angewandte Chemie International Edition* **2008**, *47*, 6172–6176.

[90] M. R. Villarreal, Diagram of a typical myelinated vertebrate motor neuron, **2007**.

[91] R. López-Leal, J. Alvarez, F. A. Court, *Cytoskeleton* **2016**, *73*, 629–639.

[92] D. Debanne, E. Campanac, A. Bialowas, E. Carlier, G. Alcaraz, *Physiological reviews* **2011**, *91*, 555–602.

[93] C. Ribrault, K. Sekimoto, A. Triller, *Nature Reviews Neuroscience* **2011**, *12*, 375–387.

[94] M. van Spronsen, C. C. Hoogenraad, *Current Neurology and Neuroscience Reports* **2010**, *10*, 207–214.

[95] A. Dani, B. Huang, J. Bergan, C. Dulac, X. Zhuang, *Neuron* **2010**, *68*, 843–856.

[96] D. Nair, E. Hosy, J. D. Petersen, A. Constals, G. Giannone, D. Choquet, J.-B. Sibarita, *Journal of Neuroscience* **2013**, *33*, 13204–13224.

[97] M. Mondin, V. Labrousse, E. Hosy, M. Heine, B. Tessier, F. Levet, C. Poujol, C. Blanchet, D. Choquet, O. Thoumine, *Journal of Neuroscience* **2011**, *31*, 13500–13515.

[98] P. Michaluk, L. Mikasova, L. Groc, R. Frischknecht, D. Choquet, L. Kaczmarek, *Journal of Neuroscience* **2009**, *29*, 6007–6012.

[99] E. D. Gundelfinger, C. Reissner, C. C. Garner, *Frontiers in Synaptic Neuroscience* **2016**, *7*.

[100] D. Ivanova, A. Dirks, A. Fejtova, *The Journal of Physiology* **2016**, *594*, 5441–5448.

[101] L. Foa, R. Gasperini, *Journal of Neurochemistry* **2009**, *108*, 1–10.

[102] F. Li, J. Z. Tsien, *New England Journal of Medicine* **2009**, *361*, 302–303.

[103] C. Cremer, R. Kaufmann, M. Gunkel, S. Pres, Y. Weiland, P. Müller, T. Ruckelshausen, P. Lemmer, F. Geiger, S. Degenhard, C. Wege, N. A. W. Lemmermann, R. Holtappels, H. Strickfaden, M. Hausmann, *Biotechnology Journal* **2011**, *6*, 1037–1051.

[104] M. Heilemann, P. Dedecker, J. Hofkens, M. Sauer, *Laser & Photonics Review* **2009**, *3*, 180–202.

[105] M. P. Gordon, T. Ha, P. R. Selvin, *Proceedings of the National Academy of Sciences* **2004**, *101*, 6462–6465.

[106] P. Hoyer, T. Staudt, J. Engelhardt, S. W. Hell, *Nano Letters* **2011**, *11*, 245–250.

[107] M. Heilemann, D. P. Herten, R. Heintzmann, C. Cremer, C. Muller, P. Tinnefeld, K. D. Weston, J. Wolfrum, M. Sauer, *Analytical Chemistry* **2002**, *74*, 3511–3517.

[108] Bornfleth, Satzler, Eils, Cremer, *Journal of Microscopy* **1998**, *189*, 118–136.

[109] R. Kaufmann, P. Lemmer, M. Gunkel, Y. Weiland, P. Müller, M. Hausmann, D. Baddeley, R. Amberger, C. Cremer, *Proc. SPIE* **2009**, *7185*, (Eds.: J. Enderlein, Z. K. Gryczynski, R. Erdmann), 1–19.

[110] A. Pertsinidis, Y. Zhang, S. Chu, *Nature* **2010**, *466*, 647–651.

[111] I. L. Medintz, H. T. Uyeda, E. R. Goldman, H. Mattoussi, *Nature Materials* **2005**, *4*, 435–446.

[112] X. Shi, Z. Xie, Y. Song, Y. Tan, E. S. Yeung, H. Gai, *Analytical Chemistry* **2012**, *84*, 1504–1509.

[113] X. Michalet, T. D. Lacoste, S. Weiss, *Methods* **2001**, *25*, 87–102.

[114] M. Song, A. Karatutlu, I. Ali, O. Ersoy, Y. Zhou, Y. Yang, Y. Zhang, W. R. Little, A. P. Wheeler, A. V. Sapelkin, *Optics Express* **2017**, *25*, 4240–4253.

[115] M. Song, PhD thesis, Queen Mary University of London, **2015**.

[116] Invitrogen, "Qdot® Streptavidin Conjugates", **2007**.

[117] Q. Zhang, Q. Jiang, N. Li, L. Dai, Q. Liu, L. Song, J. Wang, Y. Li, J. Tian, B. Ding, Y. Du, *ACS Nano* **2014**, *8*, 6633–6643.

[118] P. W. K. Rothemund, *Nature* **2006**, *440*, 297–302.

[119] K. I. Mortensen, L. S. Churchman, J. A. Spudich, H. Flyvbjerg, *Nature Methods* **2010**, *7*, 377–381.

[120] K. Lidke, B. Rieger, T. Jovin, R. Heintzmann, *Optics express* **2005**, *13*, 7052–62.

[121] F.-C. Chien, C. W. Kuo, P. Chen, *The Analyst* **2011**, *136*, 1608.

[122] Y. Wang, G. Fruhwirth, E. Cai, T. Ng, P. R. Selvin, *Nano Letters* **2013**, *13*, 5233–5241.

[123] K. A. Magarian, V. V. Fedyanin, K. R. Karimullin, I. A. Vasilieva, G. V. Klimusheva, *Journal of Physics: Conference Series* **2013**, *478*, 012007.

[124] E. Wegel, A. Göhler, B. C. Lagerholm, A. Wainman, S. Uphoff, R. Kaufmann, I. M. Dobbie, *Scientific Reports* **2016**, *6*, 27290.

[125] T. V. Bliss, G. L. Collingridge, *Nature* **1993**, *361*, 31–9.

[126] R. C. Malenka, R. A. Nicoll, *Science (New York N.Y.)* **1999**, *285*, 1870–4.

[127] A Malgaroli, R. W. Tsien, *Nature* **1992**, *357*, 134–9.

[128] D. M. Kullmann, G Erdemli, F Asztély, *Neuron* **1996**, *17*, 461–74.

[129] N. J. Emptage, C. A. Reid, A. Fine, T. V. P. Bliss, *Neuron* **2003**, *38*, 797–804.

[130] BioLegend, How's Your Synapse?, **2015**.

[131] P. D. Quevedo, T. Behnke, U. Resch-Genger, *Analytical and Bioanalytical Chemistry* **2016**, *408*, 4133–4149.

[132] M. Fu, Q. Jiao, Y. Zhao, H. Li, *J. Mater. Chem. A* **2014**, *2*, 735–744.

[133] J. D. Kubicki, *Geochemical Transactions* **2000**, *1*, 41.

[134] E. S. Andersen, M. Dong, M. M. Nielsen, K. Jahn, R. Subramani, W. Mamdouh, M. M. Golas, B. Sander, H. Stark, C. L. P. Oliveira, J. S. Pedersen, V. Birkedal, F. Besenbacher, K. V. Gothelf, J. Kjems, *Nature* **2009**, *459*, 73–76.

[135] A. Herbert, *Single Molecule Light Microscopy ImageJ Plugins*, Sussex, **2017**.

[136] H.-C. Chang, L.-C. Wang, *A Simple Proof of Thue's Theorem on Circle Packing* **2010**.